Lattice Models for Ultrafast electron dynamics in MoS_2 Monolayers

Giorgio Lovato

Master Thesis

M.Sc. Physics

Institute of Theoretical Physics and Astrophysics
Christian-Albrechts-Universität zu Kiel

Supervisor: Prof. Dr. Michael Bonitz
Second supervisor: Prof. Dr. Fabio Caruso

Kiel, November 2024

Contents

Kurzfassung

In dieser Arbeit wird die Elektronendynamik in Graphen- und MoS_2-Monolagen während der Interaktion mit hochgeladenen Ionen untersucht. Zu Beginn werden die theoretischen Grundlagen der quantenmechanischen Vielteilchentheorie dargestellt und es wird gezeigt, wie mithilfe eines sogenannten Embedding-Verfahrens die numerischen Kosten einer solchen Simulation reduziert werden können. Dazu werden die Korrelationen in den Subsystemen mit unterschiedlichen Näherungsverfahren behandelt. Dieses Verfahren wird anschließend, in Kombination mit Gittermodellen, auf Ionen-Stopping-Situationen angewendet und dazu genutzt um zu untersuchen, wie die elektronische Struktur des Materials durch den Einschlag des hochgeladenen Ions modifiziert wird. Der Ladungstransfer sowie die Beschreibung des Ions werden mithilfe eines vereinfachten Modells dargestellt, sodass die wichtigsten Prozesse abgebildet werden.

In den Simulationen werden qualitative Unterschiede zwischen den beiden Materialien festgestellt, die auf die geringere Beweglichkeit der Ladungsträger in MoS_2 zurückgeführt werden können. Ein wichtiger Unterschied ist dabei die reduzierte Emission von Sekundärelektronen in den MoS_2-Monolagen nach dem Einschlag des Ions.

Eine Untersuchung der zeitaufgelösten Spektren während der Simulation zeigt, dass die Elektronenkorrelationen zu einer grundlegenden Änderung der Zustandsdichte in MoS_2 durch die Interaktion mit dem Ion führen.

Weiterhin wird, am Beispiel des 3-Band-Modells für MoS_2, gezeigt, dass das Verfahren auch eine detaillierte Beschreibung der Bandstruktur des Monolayers ermöglicht.

Abstract

In this thesis we investigate the electron dynamics in graphene and molybdenum disulfide (MoS_2) monolayers during the interaction with highly charged ions. To do so we first lay out the theoretical groundwork of many-body quantum mechanics. Then, we show how an embedding scheme can be used to reduce the computational cost of numerical simulations in specific cases, where the different parts of a system can be treated in different approximations.

We then apply the framework together with lattice Hamiltonians to ion stopping experiments in graphene and MoS_2 monolayers in order to investigate how the material reacts to a highly charged ion impact. We use a simplified model of the ion and the charge transfer to model the electron capture process during the interaction.

We report qualitative differences between the two materials, which can mostly be attributed to the reduced carrier mobility in MoS_2 compared to graphene. Additionally, we find a reduced emission of secondary electrons during the impact in MoS_2 and by investigating the time resolved spectral properties, conclude that when correlations are included, the density of states of the MoS_2 monolayer is changed by the ion impact.

Furthermore, we show that the framework also allows for a more detailed description of the band structure of the monolayer by employing the 3-band tight-binding model for MoS_2.

1 Introduction

The dynamics of correlated fermions in non-equilibrium represent both a highly interesting field of research with applications in many cutting-edge technologies and one of the more difficult numerical challenges. Since electron dynamics, in for example condensed matter, stay hidden from direct experimental measurements and take place on timescales ranging from sub-fs to ns, the development of accurate and efficient numerical methods is of great importance to understanding how materials are altered by excitations. However, the direct solution of such many-body systems via exact diagonalization is not feasible due to the exponential growth of computational cost with the size of the system. Therefore, approximative methods have to be developed.

The first and widely used approximations to many-body quantum mechanics can be classified as Hartree-Fock (HF) or mean-field methods. They include multi-particle effects in the Hamiltonian of the system via an effective potential stemming from the averaged interactions between the particles [1–3]. These methods are computationally very favorable and can in some cases already capture many of the interaction-based effects in many-body systems. However, correlational effects are neglected in which the state of the system can not be cleanly decomposed into products or Slater-determinants of single-particle states.

The most prominent treatment of these effects in the literature is the method of time-dependent density functional theory (TDDFT) [4]. In this method an exchange-correlation functional of the particle density is introduced in order to include deviations from the Hartree solution. However, the accuracy of this method depends strongly on the choice of the functional and in general, correlations are underestimated.

A different approach, known as non-equilibrium Green's function theory (NEGF), can be derived from the second-quantization representation of many-body systems. It provides access to both the dynamical and spectral properties of the system while also allowing for the derivation of approximations from perturbative methods in the form of self-energies [5–7]. These advantages are somewhat diminished by the cubic scaling of the computation time with the number of time steps, limiting the method to short simulations.

Recent developments in the generalized Kadanoff–Baym ansatz (GKBA) [8] enabled the derivation of the time-diagonal G1–G2 scheme [9–11]. Using the HF-GKBA the propagation of the single-particle density matrix can be realized solely on the time diagonal, resulting in a linear scaling with the number of time steps. The G1–G2 scheme also allows for the usage of the perturbative approximations derived in NEGF theory as a firm theoretical basis of the method. The G1–G2 scheme can be linked to reduced density matrix (RDM) theory derived from the BBGKY hierarchy [12, 13] and can therefore give insight into the known approximations, for which a solid theoretical basis was lacking before [11]. With the inclusion of lattice models based on the tight-binding approach as well as the Hubbard treatment of Coulomb interactions, the G1–G2 scheme can be applied to many interesting situations such as laser excitation of graphene [10, 14].

The main computational challenge is then the costly propagation of the correlation tensor of order up to four, which has to be stored in the memory of the computer. To overcome this limitation, in specific situations an embedding approach can be used, in which the full system is split into two coupled systems. These two subsystems can then be treated with different approximations, effectively reducing the size of the correlation tensor [15].

One potential application for such an embedding treatment is the electronic stopping of slow, highly charged ions in graphene and MoS_2 monolayers [16]. Since the discovery of graphene, a one-atom-thick layer of carbon, 2D materials stand in the center of scientific interest due to confinement effects on the electrons. Graphene offers many properties, that can be useful in the development of small-scale electronics, such as a high carrier-mobility and high electrical and thermal conductivity [17]. However, many applications require semiconducting properties such as field effect transistors or photovoltaic cells. Graphene can be carefully prepared to exhibit semiconducting properties, with methods that can decrease the application potential by introducing complexity into and diminishing the mobility of the setup [18].

A different approach to 2D semiconductors has emerged from the exfoliation of effective 2D layers of transition-metal dichalcogenides (TMDC), which in their bulk form consist of vertical stacks of weakly coupled compound layers. These compound layers are composed of two chalcogenide layers and a transition metal layer in between, which form strong, covalent-ionic bonds. These layers can exhibit a number of different properties such as the semiconducting MoS_2 monolayers with a sizable bandgap of around $1.9\,\text{eV}$ [19]. This property can potentially be exploited in many future applications as summarized in [18]. By studying the electron dynamics in these materials during the interaction with highly charged ions, a number of insights can be obtained and can be used in applications such as fabrication and control using ion beams [20] and interactions of surfaces and plasmas [21].

This work is structured as follows. In Ch. 2, we are going to derive and discuss the theoretical framework of the G1–G2 embedding scheme. In Ch. 3 we then apply the derived equations to ion stopping in graphene and MoS_2 monolayers using effective single-band lattice models for both materials and a simplified model of the charge transfer between the ion and the monolayer. In order to link the results of these simulations to experimental observations, we are going to investigate the charge density dynamics in the monolayer, the emission of secondary electrons in the coupled system and spectral properties during the interaction. In Ch. 4 we are going to show how a more complex model, tuned for the band structure of MoS_2, can be incorporated in the simulation. Finally, we are going to summarize the results and discuss potential pitfalls of the employed methods in Ch. 5.

2 Theory

In this chapter, we will briefly revisit important theoretical concepts in many-body quantum mechanics. We will start with the general framework of many-body quantum mechanics in the mixed state description in Sec. 2.1. From this framework we will derive the equations of motion for reduced density matrices from the quantum BBGKY-hierarchy in Sec. 2.2. Furthermore, we will derive commonly known approximations for the treatment of correlation effects and link the method to the G1–G2 scheme, which is a reformulation of the HF-GKBA in non-equilibrium Green's function theory.

Afterwards, we will introduce the embedding scheme in Sec. 2.3 in order to speed up simulations of coupled systems in which the two subsystems are treated with different approximations. We will show how to derive the embedding equations of motion from both the two-time approach, as well as the time-local G1–G2 scheme.

2.1 Many-body quantum mechanics - general framework

The dynamics of quantum systems can be accurately described via the time-dependent Schrödinger Equation (SE). The state of the system is represented by a vector in Hilbert space $|\Psi\rangle$. And the SE gives the dynamics in terms of a first order differential equation

$$i\hbar\frac{\partial}{\partial t}|\Psi\rangle = \hat{H}|\Psi\rangle, \quad \langle\Psi|\Psi\rangle = 1.$$

i is the imaginary unit and $\hbar$ is Planck's constant. On the right hand side of the equation we find the operator $\hat{H}$, which is called the Hamiltonian with the property that the expectation value is equal to the total Energy of the system E

$$\langle\hat{H}\rangle = \langle\Psi|\hat{H}|\Psi\rangle = E.$$

To solve the equation also an initial condition is needed which will be the state of the system at a specific time

$$|\Psi(t=t_0)\rangle = |\Psi\rangle^0.$$

The state $|\Psi\rangle$ contains information about all particles in the system and their correlation, so we often write $|\Psi_{1,...,N}\rangle$ to indicate a N particle system.

However, solving the SE for a N particle system proves to be a problem of roughly the complexity $\sim e^N$ making it infeasible for larger system. Moreover, reducing the information about the system into a vector is only allowed when considering closed systems. In the general case we want to describe a specific system as the subsystem of a larger system, in which the larger system interacts with the subsystem. However, the larger system should not be seen as a quantum mechanical system but instead as a classical system, resulting in real weights W_k. For such an open system, we have to specify the state in the form of a mixed state, also called a density matrix [22]

$$\hat{\rho} = \sum_k W_k |\Psi_{1,..N}\rangle\langle\Psi_{1,..N}|, \quad \mathrm{Tr}\hat{\rho} = 1.$$

The weights of the sum are specified by the thermodynamic properties of the larger system. Note that all subsequent discussions of the density matrix formalism are completely independent of the larger system, i.e. the specific ensemble used.

For an environment that does not significantly depend upon the dynamics of the subsystem, for example if the environment is significantly larger than the subsystem, we can assume that $\frac{\mathrm{d}}{\mathrm{d}t}W_k = 0$ for all k. In this case we can find an equivalent equation to the SE, which gives the dynamics of the subsystem in terms of $\hat{\rho}$, namely the Von Neumann Equation (VNE)

$$i\hbar\frac{\partial}{\partial t}\hat{\rho} - [\hat{H}, \hat{\rho}] = 0.$$

In the density matrix framework expectation values are now calculated via the trace

$$\langle \hat{H} \rangle = \mathrm{Tr}_{1..N}\hat{H}\hat{\rho} = E.$$

Since the VNE is equivalent to the SE and still requires information about the complete system, the complexity of solving the equation has not improved.

2.2 Reduced Density Matrix methods

To solve the problem of exponential scaling, one must rely on approximation techniques. A prominent framework within this domain is the use of time-diagonal methods. Specifically, we will focus on the method of Reduced Density Matrices (RDM).
To start, we first consider the Hamiltonian of the full system and subdivide it into one-particle and two-particle operators[1]

$$\hat{H} = \sum_{i=1..N} \hat{T}_i + \frac{1}{2}\sum_{i,j=1..N} \hat{V}_{ij}. \tag{2.1}$$

Here, the indices indicate the particle number the operator is associated with. We can see that the full energy of the system is given by a sum over all the kinetic energies $\hat{T}_i$ of the particles and the Coulomb like interactions between the particles $\hat{V}_{ij}$. This substructure of the Hamiltonian is a reasonable assumption in most relevant cases. If, for example, we wish to calculate the total energy of the system we can write

$$E = \langle \hat{H} \rangle = \mathrm{Tr}\hat{H}\hat{\rho} = \mathrm{Tr}\bigg(\sum_{i=1..N} \hat{T}_i\hat{\rho}\bigg) + \frac{1}{2}\mathrm{Tr}\bigg(\sum_{i,j=1..N} \hat{V}_{ij}\hat{\rho}\bigg).$$

Next, we are going to introduce some labels to improve the readability. The full density matrix of the system will be denoted by $\hat{\rho}_{1..N}$ and the trace over the whole system by $\mathrm{Tr}_{1..N}$. With this notation the expression for the energy becomes

$$E = \mathrm{Tr}_{1..N}\bigg(\sum_{i=1..N} \hat{T}_i\hat{\rho}_{1..N}\bigg) + \frac{1}{2}\mathrm{Tr}_{1..N}\bigg(\sum_{i,j=1..N} \hat{V}_{ij}\hat{\rho}_{1..N}\bigg).$$

Since the operators $\hat{T}_i$ and $\hat{V}_{ij}$ only refer to the subspaces corresponding to the particle number i and j we can split the trace into two parts

$$E = \sum_{i=1..N} \mathrm{Tr}_i\hat{T}_i\mathrm{Tr}_{(1..N)/(i)}\hat{\rho}_{1..N} + \frac{1}{2}\sum_{i,j=1..N} \mathrm{Tr}_{ij}\hat{V}_{ij}\mathrm{Tr}_{(1..N)/(i,j)}\hat{\rho}_{1..N}.$$

Here the notation $(1..N)\setminus(i)$ and $(1..N)\setminus(i,j)$ indicates that the trace is over the whole system excluding the particle number i and j respectively.
The trace of the full density matrix over a subset of the full system is itself a density matrix known as a Reduced Density Matrix (RDM)

$$\begin{aligned}\hat{F}_i &:= \tilde{N}_1\mathrm{Tr}_{(1..N)/(i)}\hat{\rho}_{1..N},\\ \hat{F}_{ij} &:= \tilde{N}_2\mathrm{Tr}_{(1..N)/(i,j)}\hat{\rho}_{1..N},\end{aligned}$$

with the normalization constants $\tilde{N}_1$, $\tilde{N}_2$.
Substituting the redefinition into the expression for the energy we get

$$E = \frac{1}{\tilde{N}_1}\sum_{i=1..N} \mathrm{Tr}_i\hat{T}_i\hat{F}_i + \frac{1}{2\tilde{N}_2}\sum_{i,j=1..N} \mathrm{Tr}_{ij}\hat{V}_{ij}\hat{F}_{ij}.$$

---

[1] Note that no self-interactions exist: $\hat{V}_{ii} = 0$.

Lastly, since all the subsystems are treated equivalently[2] the sums can be removed[3]

$$E = \frac{N}{\tilde{N}_1}\mathrm{Tr}_1\hat{F}_1 + \frac{N(N-1)}{2\tilde{N}_2}\mathrm{Tr}_{12}\hat{F}_{12}.$$

The prefactors in front of the two energy contributions lead to the identification of the two normalization constants of the one-particle RDM (1-pRDM) and the two-particle RDM (2-pRDM)

$$\begin{aligned}\hat{F}_1 &\coloneqq N\mathrm{Tr}_{2..N}\hat{\rho}_{1..N}, \quad \mathrm{Tr}_1\hat{F}_1 = N,\\ \hat{F}_{12} &\coloneqq N(N-1)\mathrm{Tr}_{3..N}\hat{\rho}_{1..N}, \quad \mathrm{Tr}_{12}\hat{F}_{12} = N(N-1).\end{aligned}$$

Furthermore we can define a general s-pRDM by

$$\hat{F}_{1..s} \coloneqq \frac{N!}{(N-s)!}\mathrm{Tr}_{1..s}\hat{\rho}_{1..N}.$$

In addition to the relation to the full density matrix, we can also find relations between RDMs typically referred to as trace consistency relations

$$\hat{F}_{1..s} = \left[\prod_{i=1}(N-s-1+i)\right]^{-1}\mathrm{Tr}_{s+1..s+k}\hat{F}_{1..s+k},$$

which evaluates in the case of $s = 1, 2$ and $k = 1$ to

$$\begin{aligned}\hat{F}_1 &= \frac{1}{N-1}\mathrm{Tr}_2\hat{F}_{12},\\ \hat{F}_{12} &= \frac{1}{N-2}\mathrm{Tr}_3\hat{F}_{123}.\end{aligned}$$

Returning to the VNE, we can insert the decomposed Hamiltonian and find

$$\begin{aligned} i\hbar\frac{\partial}{\partial t}\hat{\rho}_{1..N} - \left[\sum_{i=1..N}\hat{T}_i, \hat{\rho}_{1..N}\right] - \frac{1}{2}\left[\sum_{i,j=1..N}\hat{V}_{ij}, \hat{\rho}_{1..N}\right] &= 0,\\ \Leftrightarrow i\hbar\frac{\partial}{\partial t}\mathrm{Tr}_{2..N}\hat{\rho}_{1..N} - \mathrm{Tr}_{2..N}\left[\sum_{i=1..N}\hat{T}_i, \hat{\rho}_{1..N}\right] - \frac{1}{2}\mathrm{Tr}_{2..N}\left[\sum_{i,j=1..N}\hat{V}_{ij}, \hat{\rho}_{1..N}\right] &= 0.\end{aligned}$$

We can evaluate the sums over i, j by using the fact that an operator which is completely covered by a trace can be cyclically permuted without changing the trace. Therefore, all commutators in which the indices of $\hat{T}_i$ and $\hat{V}_{ij}$ are covered by the trace will vanish[4]

$$\begin{aligned}\mathrm{Tr}_{2..N}\left[\sum_{i=1..N}\hat{T}_i, \hat{\rho}_{1..N}\right] &= \mathrm{Tr}_{2..N}\left[\hat{T}_1, \hat{\rho}_{1..N}\right],\\ \frac{1}{2}\mathrm{Tr}_{2..N}\left[\sum_{i,j=1..N}\hat{V}_{i,j}, \hat{\rho}_{1..N}\right] &= \mathrm{Tr}_{2..N}\left[\sum_{i=1..N}\hat{V}_{1i}, \hat{\rho}_{1..N}\right].\end{aligned}$$

Now we use this to simplify the equation even further by introducing the RDMs

$$\begin{aligned} i\hbar\frac{\partial}{\partial t}\mathrm{Tr}_{2..N}\hat{\rho}_{1..N} - \mathrm{Tr}_{2..N}\left(\hat{T}_1\hat{\rho}_{1..N} - \hat{\rho}_{1..N}\hat{T}_1\right) - \mathrm{Tr}_{2..N}\left(\sum_{i=1..N}\hat{V}_{1i}\hat{\rho}_{1..N} - \hat{\rho}_{1..N}\sum_{i=1..N}\hat{V}_{1i}\right) &= 0,\\ \Leftrightarrow i\hbar\frac{\partial}{\partial t}\tilde{F}_1 - \left(\hat{T}_1\tilde{F}_1 - \tilde{F}_1\hat{T}_1\right) - \mathrm{Tr}_2\left(\sum_{i=1..N}\hat{V}_{1i}\tilde{F}_{12} - \tilde{F}_{12}\sum_{i=1..N}\hat{V}_{1i}\right) &= 0,\\ \Leftrightarrow i\hbar\frac{\partial}{\partial t}\tilde{F}_1 - \left[\hat{T}_1, \tilde{F}_1\right] - \sum_{i=2..N}\mathrm{Tr}_i\left[\hat{V}_{1i}, \tilde{F}_{1i}\right] &= 0.\end{aligned}$$

Again we treat the subsystems and their couplings equivalently and obtain

$$i\hbar\frac{\partial}{\partial t}\tilde{F}_1 - \left[\hat{T}_1, \tilde{F}_1\right] - N(N-1)\mathrm{Tr}_2\left[\hat{V}_{12}, \tilde{F}_{12}\right] = 0.$$

---

[2] And all particles are indistinguishable

[3] Note that in the interaction sum we have used the fact that there are no self interactions i.e. $\hat{V}_{ii} = 0$.

[4] We also make use of the fact that $\hat{V}_{ij} = \hat{V}_{ji}$, as is the case for any sensible interaction.

Finally, with the correct normalization of the RDMs we get

$$i\hbar\frac{\partial}{\partial t}\hat{F}_1 - \big[\hat{T}_1, \hat{F}_1\big] = \mathrm{Tr}_2\big[\hat{V}_{12}, \hat{F}_{12}\big]. \tag{2.2}$$

Upon closer inspection we find that this is in fact not a closed expression for the evolution of $\hat{F}_1$, but instead couples to the 2-pRDM on the right hand side. To solve for the dynamics of a given system we would also have to compute $\hat{F}_{12}$, which evolves according to[5]

$$i\hbar\frac{\partial}{\partial t}\hat{F}_{12} - \big[\hat{T}_1 + \hat{T}_2, \hat{F}_{12}\big] = \mathrm{Tr}_3\big[\hat{V}_{13} + \hat{V}_{23}, \hat{F}_{123}\big],$$

which is also not closed but couples to the 3-pRDM. This pattern continues all the way up to $\hat{\rho}_{1..N}$. This hierarchy of coupled EOMs for the RDMs is more commonly known as the BBGKY-Hierarchy named after Bogolyubov, Born, Green, Kirkwood and Yvon [12, 13]. The hierarchy is a reformulation of the VNE and therefore the problematic scaling remains.

2.2.1 Decoupling the BBGKY-Hierarchy

To apply this framework to any real application we need to close the hierarchy by making approximations. One common way to do so is the cluster expansion. The guiding principle behind this approach is to start from an ideal system in which no interactions are present. In such a system, the 2-pRDM would simply be the product of two 1-pRDMs[6]

$$\hat{F}_{12}^{(\mathrm{id})} = \hat{F}_1\hat{F}_2.$$

However, since electron-electron interactions are important in most systems, we need to somehow capture the correlation effects which are induced by the interaction. The simplest approach is to define the correlation operator as the deviation from the ideal 2-pRDM

$$\begin{aligned} \hat{g}_{12} &\coloneqq \hat{F}_{12} - \hat{F}_{12}^{(\mathrm{id})}, \\ \Leftrightarrow \hat{F}_{12} &= \hat{F}_1\hat{F}_2 + \hat{g}_{12}. \end{aligned}$$

Substituting this reconstruction for the 2-pRDM in the first hierarchy equation we get

$$i\hbar\frac{\partial}{\partial t}\hat{F}_1 - \big[\hat{T}_1, \hat{F}_1\big] = \mathrm{Tr}_2\big[\hat{V}_{12}, \hat{F}_1\hat{F}_2\big] + \mathrm{Tr}_2\big[\hat{V}_{12}, \hat{g}_{12}\big].$$

A closer look at the first term on the right-hand side reveals that this represents an effective one-particle potential, induced by the interaction with the rest of the system

$$\begin{aligned} \mathrm{Tr}_2\big(\hat{V}_{12}\hat{F}_1\hat{F}_2 - \hat{F}_1\hat{F}_2\hat{V}_{12}\big) &= \mathrm{Tr}_2\big(\hat{V}_{12}\hat{F}_2\big)\hat{F}_1 - \hat{F}_1\mathrm{Tr}_2\big(\hat{V}_{12}\hat{F}_2\big) \\ &= \hat{U}_1^{(\mathrm{eff})}\hat{F}_1 - \hat{F}_1\hat{U}_1^{(\mathrm{eff})} \\ &= \big[\hat{U}^{(\mathrm{eff})}, \hat{F}_1\big]. \end{aligned}$$

This effective potential $\hat{U}^{(\mathrm{eff})}$ is also known as the mean-field- or Hartree potential $\hat{U}^{(\mathrm{H})}$. So we can write the EOM as

$$i\hbar\frac{\partial}{\partial t}\hat{F}_1 - \big[\hat{T}_1 + \hat{U}_1^{(\mathrm{H})}, \hat{F}_1\big] = \mathrm{Tr}_2\big[\hat{V}_{12}, \hat{g}_{12}\big].$$

On the right-hand side, we find the so-called collision integral which involves the two-particle correlation operator $\hat{g}_{12}$. Of course, this reconstruction will then also give rise to an EOM for the correlation operator, coupling to the 3-pRDM. The simplest imaginable approximation would be to require that $\hat{g}_{12} = 0$. This results in the Hartree approximation. However, in this approximation correlation effects are neglected, which are known to be important in many applications.

To include these two-particle correlation effects, we have to first find a reconstruction for the 3-pRDM, in terms of 1-pRDMs and the correlation operator. One such reconstruction is the cluster expansion

$$\hat{F}_{123} = \hat{F}_1\hat{F}_2\hat{F}_3 + \hat{F}_1\hat{g}_{23} + \hat{F}_2\hat{g}_{13} + \hat{F}_3\hat{g}_{12} + \hat{g}_{123}.$$

---

[5] The derivation follows the same strategy as for the 1-pRDM above.

[6] This simplified picture does not capture exchange effects, meaning that the particles essentially are spinless.

With this reconstruction we can now derive the EOM for the correlation operator[7]

$$\begin{aligned} i\hbar\frac{\partial}{\partial t}\hat{g}_{12} - \left[\hat{T}_1 + \hat{T}_2 + \hat{U}_1^{(\mathrm{H})} + \hat{U}_2^{(\mathrm{H})}, \hat{g}_{12}\right] &= \left[\hat{V}_{12}, \hat{F}_1\hat{F}_2\right] + \left[\hat{V}_{12}, \hat{g}_{12}\right] + \mathrm{Tr}_3\Big(\left[\hat{V}_{13}, \hat{g}_{23}\hat{F}_1\right] + \left[\hat{V}_{23}, \hat{g}_{13}\hat{F}_2\right]\Big) \\ &\quad + \mathrm{Tr}_3\left[\hat{V}_{13} + \hat{V}_{23}, \hat{g}_{123}\right] \\ &=: \hat{\Psi}_{12} + \hat{L}_{12} + \hat{\Pi}_{12} + \hat{C}_{12}. \end{aligned}$$

While on the left-hand side of the EOM we find the usual kinetic and Hartree energy contributions, the right-hand side is made up of all possible multi-particle interactions that contribute to the correlation build up in the system

a) $\hat{\Psi}_{12}$: Inhomogeneity – Interactions between two uncorrelated particles acts as a source for correlations

b) $\hat{L}_{12}$: Ladder Interaction – Repeated interactions between two particles enables the description of strong interactions

c) $\hat{\Pi}_{12}$: Polarization Interaction – Interactions between two particles are screened by the influence of surrounding particles

d) $\hat{C}_{12}$: Three-particle correlation

In order to close the hierarchy, we are going to neglect the three particle correlation effects included in $\hat{g}_{123}$, resulting in a closed expression for the combined evolution of $\hat{F}_1$ and $\hat{g}_{12}$. With this last step, we arrive at the so-called Dynamically Screened Ladder Approximation (DSL). From this basis independent expression, we can derive a number of lower order approximations by neglecting specific terms in the DSL equations, which are known from different self-energy approximations in Green's function theory [23]:

a) Second-order Born Approximation (SOA): $\hat{L}_{12}, \hat{\Pi}_{12} \to 0$

b) Particle-Particle T-matrix Approximation: $\hat{\Pi}_{12} \to 0$

c) GW Approximation: $\hat{L}_{12} \to 0$

These approximations capture only specific effects and might be applicable in specific situations, where the dominant interaction effects are known.

2.2.2 Antisymmetric reconstruction

Using the above framework for fermionic systems would require basis states which obey the fermionic symmetry with respect to particle exchange. For example a two-particle system with the one-particle basis $|i\rangle$ would result in the antisymmetric two-particle basis states

$$|i,j\rangle^- = \frac{1}{\sqrt{2}}\big(|i,j\rangle - |j,i\rangle\big).$$

Even if this might be possible to use in principle, for most practical applications, it is more convenient to instead use reconstructions which already obey the correct symmetry relations [24]. This allows for the usage of a simple basis of product states in all calculations, instead of the more costly Slater-determinants

$$\begin{aligned} \hat{F}_{12}^- &= \hat{\Lambda}_{12}^-\hat{F}_1\hat{F}_2 + \hat{g}_{12}^-, \\ \hat{F}_{123}^- &= \hat{\Lambda}_{123}^-\hat{F}_1\hat{F}_2\hat{F}_3 + \hat{\Lambda}_{(23),1}\hat{F}_1\hat{g}_{12}^- + \hat{\Lambda}_{(13),2}\hat{F}_2\hat{g}_{13}^- + \hat{\Lambda}_{(12),3}\hat{F}_3\hat{g}_{12}^-, \end{aligned}$$

with the antisymmetrization operator

$$\begin{aligned} \hat{\Lambda}_{12}^- &= \big(1 - \hat{P}_{12}\big), \\ \hat{\Lambda}_{(12),3}^- &= \big(1 - \hat{P}_{13} - \hat{P}_{23}\big), \\ \hat{\Lambda}_{123}^- &= \hat{\Lambda}_{12}^-\hat{\Lambda}_{(12),3}^-. \end{aligned}$$

---

[7] For a detailed derivation please see Sec. A.1 in the appendix.

Here, we used the permutation operator $\hat{P}_{12}$ which is defined by its action on two-particle states

$$\hat{P}_{12} \left| i, j \right\rangle = \left| j, i \right\rangle .$$

With these reconstructions of course also the resulting EOMs change[8]

$$\begin{aligned} i\hbar \frac{\partial}{\partial t}\hat{F}_1 - \left[\hat{T}_1 + \hat{U}_1^{(\mathrm{HF})}, \hat{F}_1\right] &= \mathrm{Tr}_2\left[\hat{V}_{12}, \hat{g}_{12}^{-}\right], \\ i\hbar \frac{\partial}{\partial t}\hat{g}_{12}^{-} - \left[\hat{T}_1 + \hat{T}_2 + \hat{U}_1^{(\mathrm{HF})} + \hat{U}_2^{(\mathrm{HF})}, \hat{g}_{12}^{-}\right] &= \hat{\Psi}_{12}^{-} + \hat{L}_{12}^{-} + \hat{\Pi}_{12}^{-}. \end{aligned} \tag{2.3}$$

All contributions now also include particle exchange effects. The Hartree potential becomes the Hartree-Fock potential

$$\hat{U}_1^{(\mathrm{H})} \to \hat{U}_1^{(\mathrm{HF})} = \mathrm{Tr}_2\big(\hat{V}_{12}^{-}\hat{F}_2\big),$$

with the antisymmetric interaction $\hat{V}_{12}^{-} = \hat{V}_{12}\hat{P}_{12}$. The second order interactions becomes

$$\hat{\Psi}_{12} \to \hat{\Psi}_{12}^{-} = \tilde{V}_{12}^{-}\hat{F}_1\hat{F}_2 - \hat{F}_1\hat{F}_2\tilde{V}_{12}^{-,\dagger},$$

with the Pauli blocked interaction

$$\tilde{V}_{12}^{-} = \big(1 - \hat{F}_1 - \hat{F}_2\big)\hat{V}_{12}^{-},$$

which includes phase space filling effects due to the Pauli exclusion principle. The Ladder interaction becomes

$$\hat{L}_{12} \to \hat{L}_{12}^{-} = \tilde{V}_{12}\hat{g}_{12}^{-} - \hat{g}_{12}^{-}\tilde{V}_{12},$$

where Pauli Blocking is included as well. The polarization interaction becomes

$$\hat{\Pi}_{12} \to \hat{\Pi}_{12}^{-} = \mathrm{Tr}_3\bigg(\left[\hat{V}_{13}^{-}, \hat{g}_{23}^{-}\hat{F}_1\right] + \left[\hat{V}_{23}^{-}, \hat{g}_{13}^{-}\hat{F}_2\right]\bigg)\hat{\Lambda}_{12}^{-}.$$

Eqs. (2.3) represent the DSL approximation with exchange effects. We can again also formulate different lower order approximations [11]

a) SOA Approximation with exchange: $\hat{L}_{12}^{-} = \hat{\Pi}_{12}^{-} = 0$

b) Particle-Particle T-matrix Approximation: $\hat{\Pi}_{12}^{-} = 0$

c) GW Approximation with Particle-Hole T-matrix terms and respective cross couplings: $\hat{L}_{12}^{-} = 0$

2.2.3 Alternative representation: second quantization

A different representation for the many-body state is the so-called occupation number representation. We start by considering the N particle wave function as a product of N single particle states[9]

$$\left|\Psi_{1,..N}\right\rangle = \bigotimes_{k=1}^{N} \left|\psi_k\right\rangle .$$

In the occupation number representation, we instead keep track only of the occupation of each one-particle state n_i. The full, antisymmetric state of the system is then given by[10]

$$\left|\Psi_{1,..N}\right\rangle^{-} = \left|n_0, n_1, ..., n_B\right\rangle = \left|\{n\}\right\rangle .$$

In the following, we will focus on fermionic systems. For such a state, the occupation numbers can only be $n_i = 1$ or $n_i = 0$, as posited by the spin statistics theorem. Since these states represent states with

---

[8] Please refer to Sec. A.2 of the appendix for a detailed derivation

[9] For bosonic (fermionic) states, we have to include the proper (anti-) symmetrization and normalization of the state, so that the spin statistics theorem is satisfied.

[10] Here B is the number of basis states.

different numbers of particles, they are no longer states in Hilbert space but instead in so-called Fock space, which is a direct sum of Hilbert spaces with different particle numbers

$$\mathcal{F} = \mathcal{H}_0 \oplus \mathcal{H}_1 \oplus \cdots \oplus \mathcal{H}_N.$$

This representation allows for the description of the creation and annihilation of particles in the system. These actions are performed by the fermionic creation $\hat{c}_i^\dagger$ and annihilation $\hat{c}_i$ operators acting on the state

$$\begin{aligned} \hat{c}_i^\dagger \left|n_0, ..., n_i, ..., n_N\right\rangle &= (-1)^{\alpha_i} \sqrt{1-n_i} \left|n_0, ..., n_i+1, ..., n_N\right\rangle, \\ \hat{c}_i \left|n_0, ..., n_i, ..., n_N\right\rangle &= (-1)^{\alpha_i} \sqrt{n_i} \left|n_0, ..., n_i-1, ..., n_N\right\rangle, \\ \alpha_i &= \sum_{l<i} n_l. \end{aligned}$$

The correct symmetry of the fermionic states is also preserved by the creation and annihilation operators via their anti-commutation relations

$$\begin{aligned} \left[\hat{c}_i^\dagger, \hat{c}_j\right]_+ &= \hat{c}_i^\dagger \hat{c}_j + \hat{c}_j \hat{c}_i^\dagger = \delta_{i,j}, \\ \left[\hat{c}_i^\dagger, \hat{c}_j^\dagger\right]_+ &= \left[\hat{c}_i, \hat{c}_j\right]_+ = 0. \end{aligned}$$

This allows for the usage of much simpler basis states without the need for antisymmetrization.
The advantage of this approach is that all operators can be expressed in terms of the creation and annihilation operators

$$\hat{D}_K = \frac{1}{K!} \sum_{j_1...j_k m_1...m_k=1}^{B} d_{j_1...j_k m_1...m_k} \hat{c}_{j_1}^\dagger ... \hat{c}_{j_k}^\dagger \hat{c}_{m_k} ... \hat{c}_{m_1}. \tag{2.4}$$

Therefore, all observables and all contributions to the Hamiltonian of the system will be given by products of creation and annihilation operators. In principle, this implies that the complete information about the system and its dynamics can be obtained by solving the Heisenberg equations of motion

$$\begin{aligned} \frac{\partial}{\partial t} \hat{c}_i(t) &= \left[\hat{H}, \hat{c}_i(t)\right], \\ \frac{\partial}{\partial t} \hat{c}_i^\dagger(t) &= -\left[\hat{c}_i^\dagger(t), \hat{H}\right]. \end{aligned}$$

However, since this is a set of operator-equations, it is not directly solvable. Instead, all operators have to be represented in a specific basis, which introduces similar challenges as the BBGKY formalism.

2.2.4 Non-equilibrium Green's functions

The G1–G2 scheme is another approach to many-body quantum mechanics which is based on non-equilibrium Green's functions (NEGF). In the following section we will give a brief introduction into NEGFs and outline the derivation of the G1–G2 scheme. More information and details on the formalism can be found in [9–11].
We start with the Hamiltonian in second quantization, which can be stated in terms of the creation and annihilation operators in an arbitrary basis $|i\rangle$ as demonstrated in Eq. (2.4)

$$\hat{H}(t) = \sum_{ij} h_{ij}^{(0)} \hat{c}_i^\dagger \hat{c}_j + \frac{1}{2} \sum_{ijkl} w_{ijkl}(t) \hat{c}_i^\dagger \hat{c}_j^\dagger \hat{c}_l \hat{c}_k.$$

In this expression of the Hamiltonian h^0 is the kinetic energy $\hat{T}$ and w is the interaction pair potential $\hat{V}$ (compare to Eq. (2.1)). The dynamic quantities of interest in this formalism are the creation and annihilation operator correlation functions, like the one-particle Green's function

$$G_{ij}(z, z') = \frac{1}{i\hbar} \left\langle \mathcal{T}_\mathcal{C} \left\{ \hat{c}_i^\dagger(z) \hat{c}_j(z') \right\} \right\rangle.$$

The arguments z, z' represent points on the complex Keldysh contour $\mathcal{C}$ [5] and $\mathcal{T}_\mathcal{C}$ is the time-ordering operator. The ensemble averaging indicated by $\langle\cdot\rangle$ is performed using the correlated unperturbed N-particle density operator of the system. This last fact also explains why in the pair potential $w(t)$ an

explicit time dependency appears, because in order to obtain the correlated density operator, one has to find the correlated ground state of the system. This can be done in a number of ways, but the most convenient one is the method of adiabatic switching [25] in which the interaction is slowly switched on to transition from the ideal ground state to the correlated one.
The EOMs on the contour for G are given by the Keldysh-Kadanoff-Baym equations (KBEs) [23]

$$\begin{aligned}\sum_k \left[i\hbar \frac{\mathrm{d}}{\mathrm{d}z}\delta_{ik} - h^{(0)}_{ik} \right] G_{kj}(z,z') - \delta_{ij}\delta_{\mathcal{C}}(z,z') &= -i\hbar \sum_{klp} \int_{\mathcal{C}} \mathrm{d}\bar{z}\, w_{iklp}(z,\bar{z}) G^{(2)}_{lpjk}(z,\bar{z},z',\bar{z}^+) \qquad (2.5)\\ &= \sum_k \int_{\mathcal{C}} \mathrm{d}\bar{z}\, \Sigma_{ik}(z,\bar{z}) G_{kj}(\bar{z},z'), \qquad (2.6)\\ \sum_k G_{ik}(z,z') \left[-i\hbar \frac{\overleftarrow{\mathrm{d}}}{\mathrm{d}z} - h^{(0)}_{kj} \right] - \delta ij \delta_{\mathcal{C}}(z,z') &= -i\hbar \sum_{klp} \int_{\mathcal{C}} \mathrm{d}\bar{z}\, G^{(2)}_{iklp}(z,\bar{z}^-,z',\bar{z}) w_{lpjk}(\bar{z},z')\\ &= \sum_k \int_{\mathcal{C}} \mathrm{d}\bar{z}\, G_{ik}(z,\bar{z}) \Sigma_{kj}(\bar{z},z').\end{aligned}$$

Again, for further details, the reader is refered to the references, while for the purpose of this work, three observations about the KBEs are of interest. First, we realize that the left-hand sides of the equations correspond to the free propagation of the one-particle Green's function while the right-hand sides couple the dynamics to the rest of the system and include interaction effects via the pair potential. Second, we can write the right-hand sides in two distinct ways. On way (Eq. (2.5)) involves the two-particle Green's function

$$G^{(2)}_{ijkl}(z_1,z_2,z_3,z_4) = \frac{1}{(i\hbar)^2} \big\langle \mathcal{T}_{\mathcal{C}} \big\{ \hat{c}^\dagger_i(z_1) \hat{c}^\dagger_j(z_2), \hat{c}_l(z_4) \hat{c}_k(z_3) \big\} \big\rangle,$$

which is very reminiscent of the way the 1-pRDM coupled to the 2-pRDM in Eq. (2.2). In fact, it is not surprising, that, hidden in the NEGF formalism, there is also a hierarchy of correlation functions called the Martin-Schwinger-hierarchy [26]. The other way (Eq. (2.6)) removes the two-particle quantity and instead introduces the self-energy Σ. Self-energy is a prominent concept in quantum field theory that incorporates the interactions with the rest of the system by renormalizing the energy of the particle itself. In principle, this reformulation of the correlation integral is exact, but since the self-energy is not completely known, we have to approximate it. Finally, the third observation is the appearance of the contour integral $\int_{\mathcal{C}}$ on the right hand side. In the previous section 2.2.1 we saw that the correlation integral only depends on the 2-pRDM at the same time (Eq. (2.2)). However, in the NEGF formalism, since we are propagating two-time quantities such as the one-particle Green's function, the correlations depend on the history of the system incorporated by the so-called memory integral.
In order to apply this approach for the simulation of real systems, we first have to move from the Keldysh contour onto the real-time plane. This can be achieved by selecting different contour time orders, applying the time-ordering operator and focusing on the real times t

$$\begin{aligned} G^<_{ij}(t,t') &\coloneqq -\frac{1}{i\hbar} \big\langle \hat{c}^\dagger_j(t') \hat{c}_i(t) \big\rangle, \quad t < t',\\ G^>_{ij}(t,t') &\coloneqq \frac{1}{i\hbar} \big\langle \hat{c}_i(t) \hat{c}^\dagger_j(t') \big\rangle, \quad t > t'.\end{aligned}$$

Here, the benefit of this approach becomes clear. Not only do we have access to time-diagonal quantities like the 1-pRDM

$$F_{ij}(t) = -i\hbar G^<_{ji}(t,t),$$

but we can also calculate spectral properties which require the Fourier transform, with respect to the difference time $\tau = t' - t$, of $G^>_{ij}(t,t') - G^<_{ij}(t,t')$ [6, 7]. However, there is also a cost to this advantage, namely the computationally expensive contour integral. The computation of this integral can result in cubic scaling with the propagation time, disallowing long simulation times.
At this point, two important self-energies should be pointed out. The simplest one is the Hartree-Fock self-energy which only has a time-diagonal contribution

$$\Sigma^{\mathrm{HF}}_{ij}(t) = -i\hbar \sum_{kl} w^-_{ikjl}(t) G^<_{lk}(t,t).$$

Due to the simple structure of the HF self-energy, it can be treated as an effective one-particle Hamiltonian and grouped together with the kinetic energy[11]

$$h_{ij}^{\mathrm{HF}}(t) = h_{ij}^{0} - i\hbar \sum_{kl} w_{ikjl}^{-}(t) G_{lk}^{<}(t,t).$$

The simplest self-energy beyond Hartree-Fock that includes correlation effects is the second-order Born approximation (SOA). The self-energy for SOA does include off diagonal elements as well as the HF contributions on the diagonal

$$\Sigma_{ij}^{\gtrless,\mathrm{SOA}}(t,t') = -(i\hbar)^2 \sum_{klpqrs} w_{iklp}^{-}(t) w_{qrjs}^{-}(t') G_{lq}^{\gtrless}(t,t') G_{pr}^{\gtrless}(t,t') G_{sk}^{\lessgtr}(t',t).$$

2.2.5 HF-GKBA and equivalence to the G1–G2 scheme

In some applications, it is not unreasonable to discard accurate spectral information in exchange for a less expensive propagation. In fact, we can even go one step further by considering only the evolution of the one-particle Green's function along the time-diagonal

$$i\hbar \frac{\partial}{\partial t} G_{ij}^{<}(t) - \left[\boldsymbol{h}^{\mathrm{HF}}, \boldsymbol{G}^{<}\right]_{ij}(t) = i\hbar \sum_{k} \int_{t_0}^{t} \mathrm{d}\,\bar{t}\, \left[\Sigma_{ik}^{\mathrm{SOA},>}(t,\bar{t}) G_{kj}^{<}(\bar{t},t) - \Sigma_{ik}^{\mathrm{SOA},<}(t,\bar{t}) G_{jk}^{>}(\bar{t},t)\right].$$

Since the evolution on the time-diagonal still depends on the off diagonal elements, the EOM is not fully time-diagonal and the costly memory integral still occurs.

For this reason, a common way to approximate the full two-time solution is to use a reconstruction of the off-diagonal part of the one-particle Green's function [8]

$$G_{ij}^{\gtrless}(t,t') = i\hbar \sum_{k} \left\{ G_{ik}^{\mathrm{R}}(t,t') G_{kj}^{\gtrless}(t') - G_{ik}^{\gtrless}(t) G_{kj}^{\mathrm{A}}(t,t') \right\}, \tag{2.7}$$

with the retarded and advanced Green's functions

$$G_{ij}^{\mathrm{R/A}}(t,t') = \pm\Theta[\pm(t-t')]\left\{ G_{ij}^{>}(t,t') - G_{ij}^{<}(t,t') \right\}.$$

The reconstruction already represents an approximation since all terms, involving temporal integrals as well as the self-energy, were neglected. This ansatz for the off-diagonal parts is more commonly known as the Generalized Kadanoff–Baym Ansatz (GKBA). To apply this reconstruction, we also need to know the off-diagonal propagators $G^{\mathrm{R/A}}$ and the most common choices are either the free GKBA or the HF-GKBA where the propagators are the free and the Hartree-Fock propagators respectively. In SOA, this approximation reduces the computational cost significantly but for higher order self-energies the cubic scaling remains. Furthermore, since the ansatz affects the off-diagonal elements of the Green's function, the spectral properties will only be available in the approximation order chosen for the propagators.

As described in [27] and further expanded upon in [9–11], one can, in fact, by using the GKBA, completely remove the memory integral from the EOM for the Green's function on the time-diagonal. This is achieved by utilizing the KBEs defined in terms of the two-particle Green's function instead of the self-energy approach in Eq. (2.5). The strategy is fairly straight forward:

I.) Choose a specific self-energy and insert it into the KBEs on the time-diagonal

II.) Compare the expressions on the right hand side to the first equation of the Martin-Schwinger-hierarchy[12]

III.) Identify the appropriate reconstruction of $G^{(2)}$

IV.) Using the HF-GKBA, compute the EOM for $G^{(2)}$

The result is the G1–G2 scheme which has been proven to exhibit linear scaling in the propagation time at the cost of propagating the two-particle Green's function [27].

---

[11] The similarity to the HF contribution in the RDM framework (compare Sec. 2.2.1) is no coincidence.

[12] Meaning the KBEs without the self-energy.

To illustrate this procedure, we will quickly demonstrate the derivation of the G1–G2 scheme in SOA. The EOM on the diagonal reads

$$
\begin{aligned}
i\hbar\frac{\mathrm{d}}{\mathrm{d}t}G^{<}_{ij}(t)-\left[\boldsymbol{h}^{0},\boldsymbol{G}^{<}\right]_{ij}(t) &= \sum_{k}\Sigma^{\mathrm{HF}}_{ik}(t)G^{<}_{kj}(t)\\
&\quad-\sum_{k}\int_{t_t}^{\mathrm{t}}\mathrm{d}\bar{t}\left[\Sigma^{>,\mathrm{SOA}}_{ik}(t,\bar{t})G^{<}_{kj}(\bar{t},t)-\Sigma^{<,\mathrm{SOA}}_{ik}(t,\bar{t})G^{>}_{kj}(\bar{t},t)\right] &&(2.8)\\
&= -i\hbar\sum_{klp}w_{iklp}(t)G^{(2)}_{lpjk}(t). &&(2.9)
\end{aligned}
$$

Next, we split $G^{(2)}$ into two parts

$$
G^{(2)}_{ijkl}(t)=G^{(2),\mathrm{HF}}_{ijkl}(t)+\mathcal{G}_{ijkl}(t),
$$

where the first and second part account for the HF and SOA self-energies respectively. By comparing Eqs. (2.8) and (2.9), we can conclude the following identities

$$
G^{\gtrless,(2),\mathrm{HF}}_{ijkl}(t)=G^{\gtrless}_{ik}(t)G^{\gtrless}_{jl}(t)-G^{\gtrless}_{il}(t)G^{\lessgtr}_{jk}(t)=G^{\gtrless,(2),\mathrm{H}}_{ijkl}(t)-G^{\gtrless,(2),\mathrm{F}}_{ijkl}(t)
$$

and

$$
\mathcal{G}_{ijkl}(t)=i\hbar\sum_{pqrs}\int_{t_0}^{\mathrm{t}}\mathrm{d}\bar{t}w^{-}_{pqrs}(\bar{t})\left[G^{>,(2),\mathrm{H}}_{ijpq}(t,\bar{t})G^{>,(2),\mathrm{H}}_{rskl}(\bar{t},t)-G^{<,(2),\mathrm{H}}_{ijpq}(t,\bar{t})G^{<,(2),\mathrm{H}}_{rskl}(\bar{t},t)\right].
$$

Finally, by applying the HF-GKBA and differentiating the expression of $G^{(2)}$ with respect to time we obtain the coupled set of EOMs for the G1–G2 scheme in SOA [14]

$$
\begin{aligned}
i\hbar\frac{\mathrm{d}}{\mathrm{d}t}G^{<}_{ij}(t)-\left[\boldsymbol{h}^{\mathrm{HF}},\boldsymbol{G}^{<}\right]_{ij}(t)&=\left[\boldsymbol{I}+\boldsymbol{I}^{\dagger}\right]_{ij}(t),\quad I_{ij}(t)=-i\hbar\sum_{klp}w_{iklp}(t)\mathcal{G}_{lpjk}(t),\\
i\hbar\frac{\mathrm{d}}{\mathrm{d}t}\mathcal{G}_{ijkl}(t)-\left[\boldsymbol{h}^{(2),\mathrm{HF}},\boldsymbol{\mathcal{G}}\right]_{ijkl}(t)&=\frac{1}{2}\sum_{pq}w^{-}_{ijpq}(t)G^{<}_{pk}(t)G^{<}_{ql}(t)+i\hbar\sum_{pqr}w^{-}_{ipqr}(t)G^{<}_{jp}(t)G^{<}_{qk}(t)G^{<}_{rl}(t).
\end{aligned}
$$

Using the same strategy, one can find EOMs for all higher order self-energies, as demonstrated in [11]. There, comparisons between the RDM and the G1–G2 approach were performed. The authors conclude that both methods are equivalent in HF, SOA and TPP approximation with and without exchange, meaning that for all known NEGF self-energies one can find an equivalent G1–G2 formulation. Since approximations stemming from self-energies can be better understood in terms of the diagrams they include, it is very useful to be able to assign them to the time-diagonal contributions. At the same time, no direct self-energy equivalent to the full DSL approximation in the context of the G1–G2 scheme and RDMs were identified. Therefore, the time-diagonal methods allow us to study new approximations that were previously not reachable. Since we can also find these approximations in the spinless RDM approach, we can study the effects in a much more intuitive framework without exchange effects.

In this work we will focus on HF and SOA and make use of the G1–G2 framework which has now been tested multiple times for simple Hubbard chains and more complex finite graphene clusters. [11, 14]

2.3 Embedding

In the following, we focus on a special case of the G1–G2 scheme, namely the description of a system which can in some sense be described by a system and an environment. Possible applications for such a framework might be the description of electron dynamics in a crystal with metal contacts or, as we will discuss later in Ch. 3, a charged particle like an ion colliding with a graphene or MoS_2 monolayer.

Of course the G1–G2 scheme could be used to describe the full system in detail but that might require unnecessary computation cost since the system and the environment might evolve on completely different time scales and correlation effects might not be of equal importance. The goal of the embedding scheme is therefore to be able to make different approximations for the correlations in both the system and the environment. For example, in the ion stopping scenario, one might want to use a higher order self-energy in the system such as SOA while treating the ion without correlations altogether.

The derivation of such a framework from the NEGF perspective is demonstrated in [15, 28]. The Hamiltonian of such a system can be written in the following form

$$\hat{H}(t) = \sum_{\alpha,\beta\in\Omega} \sum_{ij} h_{ij}^{\alpha\beta}(t)\hat{c}_i^{\alpha,\dagger}\hat{c}_j^{\beta,\dagger} + \frac{1}{2}\sum_{\alpha,\beta,\gamma,\delta\in\Omega}\sum_{ijkl} w_{ijkl}^{\alpha\beta\gamma\delta}(t)\hat{c}_i^{\alpha,\dagger}\hat{c}_j^{\beta,\dagger}\hat{c}_l^{\delta}\hat{c}_k^{\gamma},$$

where $\Omega = \{e, s\}$ is a set of indices with e for states of the environment and s for states of the system. The creation and annihilation operators likewise refer to state i of α and create or annihilate a particle in this specific state. The one-particle Hamiltonian now includes three parts

$$\boldsymbol{h} = \begin{pmatrix} \boldsymbol{h}^{\mathrm{ss}} & \boldsymbol{h}^{\mathrm{se}} \\ \boldsymbol{h}^{\mathrm{es}} & \boldsymbol{h}^{\mathrm{ee}} \end{pmatrix},$$

with $h^{\mathrm{se}} = h^{\mathrm{es},\dagger}$, which represent the one-particle Hamiltonian on the system (ss), in the environment (ee) and the possible transition between the two (es). The same is true for the interaction pair potential w. Because we introduced different kinds of operators, we also need to introduce the corresponding Green's functions

$$G_{ij}^{\alpha\beta}(z, z') = \frac{1}{i\hbar}\big\langle \mathcal{T}_{\mathcal{C}}\big\{\hat{c}_i^{\alpha,\dagger}(z)\hat{c}_j^{\beta}(z')\big\}\big\rangle.$$

Eventually, this approach will lead to four sets of KBEs for all combinations of α and β in the one-particle Green's function

$$i\hbar\frac{\mathrm{d}}{\mathrm{d}z}G_{ij}^{\alpha\beta}(z,z') - \sum_{\delta\in\Omega}\sum_k h_{ik}^{\alpha\delta,(\mathrm{HF})}(z)G_{kj}^{\delta\beta}(z,z') = \delta_{ij}^{\alpha\beta}\delta_{\mathcal{C}}(z,z') + \sum_{\delta\in\Omega}\sum_k \int_{\mathcal{C}} \mathrm{d}\bar{z}\Sigma_{ik}^{\alpha\delta}(z,\bar{z})G_{kj}^{\delta\beta}(\bar{z},z').$$

2.3.1 NEGF embedding equations

To neglect correlation in the environment, as well as in the transfer between system and environment, we adopt a specific form of the self-energies. One such choice, which would be in line with the previous statement about the neglect of correlations in the environment, would be

$$\boldsymbol{\Sigma}^{\mathrm{es}} = \boldsymbol{\Sigma}^{\mathrm{ee}} = 0, \quad \boldsymbol{\Sigma}^{\mathrm{ss}} = \boldsymbol{\Sigma}.$$

This ansatz enables us to write the equations of motion for the whole system as [15]

$$i\hbar\frac{\mathrm{d}}{\mathrm{d}z}G_{ij}^{\mathrm{ss}}(z,z') - \sum_k h_{ik}^{\mathrm{ss},(\mathrm{HF})}(z)G_{kj}^{\mathrm{ss}}(z,z') = \delta_{ij}\delta_{\mathcal{C}}(z,z') + \sum_k \int_{\mathcal{C}}\mathrm{d}\bar{z}\big\{\Sigma_{ik}(z,\bar{z}) + \Sigma_{ik}^{\mathrm{emb}}(z,\bar{z})\big\}G_{kj}^{\mathrm{ss}}(\bar{z},z'),$$

$$\Sigma_{ij}^{\mathrm{emb}}(z,z') = \sum_k h_{ik}^{\mathrm{se},(\mathrm{HF})}(z)G_{kl}^{\mathrm{ee}}(z,z')h_{lj}^{\mathrm{es},(\mathrm{HF})}(z'),$$

$$i\hbar\frac{\mathrm{d}}{\mathrm{d}z}G_{ij}^{\mathrm{ee}}(z,z') - \sum_k h_{ik}^{\mathrm{ee},(\mathrm{HF})}(z)G_{kj}^{\mathrm{ee}}(z,z') = \sum_{ik} h_{ik}^{\mathrm{es},(\mathrm{HF})}(z)G_{kj}^{\mathrm{se}}(z,z') + \delta_{ij}\delta_{\mathcal{C}}(z,z'),$$

$$i\hbar\frac{\mathrm{d}}{\mathrm{d}z}G_{ij}^{\mathrm{es}}(z,z') = \sum_k h_{ik}^{\mathrm{es},(\mathrm{HF})}(z)G_{kj}^{\mathrm{ss}}(z,z') - \sum_k h_{ik}^{\mathrm{ee},(\mathrm{HF})}(z)G_{kj}^{\mathrm{es}}(z,z').$$

To derive the time-local G1–G2 embedding scheme, the remaining steps are to transition to the real-time plane, apply the HF-GKBA and differentiate the resulting expressions with respect to time. With that, we obtain the coupled set of EOMs

$$i\hbar\frac{\partial}{\partial t}G_{ij}^{\mathrm{ss},<}(t) - \big[\boldsymbol{h}^{\mathrm{ss},(\mathrm{HF})}, \boldsymbol{G}^{\mathrm{ss},<}\big]_{ij}(t) = \big[\boldsymbol{I}(t) + \boldsymbol{I}^{\dagger}(t)\big], \tag{2.10}$$

$$\boldsymbol{I}(t) = \boldsymbol{I}^{\mathrm{corr}}(t) + \boldsymbol{I}^{\mathrm{emb}}(t), \quad I_{ij}^{\mathrm{corr}}(t) = -i\sum_{klp} w_{iklp}(t)\mathcal{G}_{lpjk}(t), \quad I_{ij}^{\mathrm{emb}}(t) = \sum_k h_{ik}^{\mathrm{se},(\mathrm{HF})}(t)G_{kj}^{\mathrm{es},<}(t),$$

$$\begin{aligned} i\hbar\frac{\partial}{\partial t}G_{ij}^{\mathrm{es},<}(t) = {} & \sum_k h_{ik}^{\mathrm{es},(\mathrm{HF})}(t)G_{kj}^{\mathrm{ss},<}(t) - \sum_k G_{ik}^{\mathrm{ee},<}(t)h_{kj}^{\mathrm{es},(\mathrm{HF})}(t) \\ & + \sum_k h_{ik}^{\mathrm{ee},(\mathrm{HF})}(t)G_{kj}^{\mathrm{es},<}(t) - \sum_k G_{ik}^{\mathrm{es},<}(t)h_{kj}^{\mathrm{ss},(\mathrm{HF})}(t), \end{aligned} \tag{2.11}$$

$$i\hbar\frac{\partial}{\partial t}G_{ij}^{\mathrm{ee},<}(t) - \big[\boldsymbol{h}^{\mathrm{ee},(\mathrm{HF})}, \boldsymbol{G}^{\mathrm{ee},<}\big]_{ij}(t) = \sum_k h_{ik}^{\mathrm{es},(\mathrm{HF})}(t)G_{kj}^{\mathrm{se},<}(t) - \sum_k G_{ik}^{\mathrm{es},<}(t)h_{kj}^{\mathrm{se},(\mathrm{HF})}(t), \tag{2.12}$$

$$i\hbar\frac{\partial}{\partial t}\mathcal{G}_{ijkl}(t) - \big[\boldsymbol{h}^{(2),(\mathrm{HF})}, \boldsymbol{\mathcal{G}}\big]_{ijkl}(t) = C_{ijkl}(t).$$

Here, we used the shorthand $C_{ijkl}(t)$ to denote any kind of approximation for the two-particle interactions one might choose in the system. Note also that we do not have to define an EOM for $G^{\mathrm{se},<}$ since

$$\boldsymbol{G}^{\mathrm{se},<}(t) = -\left[\boldsymbol{G}^{\mathrm{es},<}\right]^{\dagger}(t).$$

2.3.2 Derivation of the embedding scheme from a time-local framework

A different route to the G1–G2 embedding scheme can be taken if one starts already with the conventional EOM for the real-time single-particle Green's function

$$i\hbar\frac{\partial}{\partial t}G^{<}_{ij}(t) - \left[\boldsymbol{h}^{(\mathrm{HF})}, \boldsymbol{G}^{<}\right]_{ij}(t) = \left[\boldsymbol{I}(t) + \boldsymbol{I}^{\dagger}(t)\right]_{ij}, \tag{2.13}$$

where the collision integral I contains the coupling to the correlation part of the two-particle Green's function $\mathcal{G}$, which we will put aside for the moment. Consider now a reinterpretation of the basis indices i, j as referring to states that either live in the system or the environment

$$|i\rangle = |\alpha, \underline{i}\rangle\,, \quad \alpha \in \Omega = \{e, s\}, \underline{i} \in \{\underline{i}\,, |\underline{i}\rangle \in e\}.$$

In this representation the one-particle Green's function and all other single particle quantities become

$$\boldsymbol{G}^{<} \to \begin{pmatrix} \boldsymbol{G}^{\mathrm{ss},<} & \boldsymbol{G}^{\mathrm{se},<} \\ \boldsymbol{G}^{\mathrm{es},<} & \boldsymbol{G}^{\mathrm{ee},<} \end{pmatrix}, \quad \boldsymbol{h}^{(\mathrm{HF})} \to \begin{pmatrix} \boldsymbol{h}^{\mathrm{ss},(\mathrm{HF})} & \boldsymbol{h}^{\mathrm{se},(\mathrm{HF})} \\ \boldsymbol{h}^{\mathrm{es},(\mathrm{HF})} & \boldsymbol{h}^{\mathrm{ee},(\mathrm{HF})} \end{pmatrix} \text{ and } \boldsymbol{I} \to \begin{pmatrix} \boldsymbol{I}^{\mathrm{ss}} & \boldsymbol{I}^{\mathrm{se}} \\ \boldsymbol{I}^{\mathrm{es}} & \boldsymbol{I}^{\mathrm{ee}} \end{pmatrix}.$$

Inserting this into Eq. (2.13) we get

$$i\hbar\frac{\partial}{\partial t}G^{\alpha\beta,<}_{\underline{ij}}(t) - \sum_{\delta\in\Omega}\sum_{\underline{k}}\left(h^{\alpha\delta,(\mathrm{HF})}_{\underline{ik}}(t)G^{\delta\beta,<}_{\underline{kj}}(t) - G^{\alpha\delta,<}_{\underline{jk}}(t)h^{\delta\beta,(\mathrm{HF})}_{\underline{kj}}(t)\right) = \left[\boldsymbol{I}(t) + \boldsymbol{I}^{\dagger}(t)\right]^{\alpha\beta}_{\underline{ij}}.$$

Now we can simply read of the EOM for the (ss) component of the single particle Green's function

$$\begin{aligned}
i\hbar\frac{\partial}{\partial t}G^{\mathrm{ss},<}_{\underline{ij}}(t) - \sum_{\underline{k}}\Big(&h^{\mathrm{ss},(\mathrm{HF})}_{\underline{ik}}(t)G^{\mathrm{ss},<}_{\underline{kj}}(t) - G^{\mathrm{ss},<}_{\underline{ik}}(t)h^{\mathrm{ss},(\mathrm{HF})}_{\underline{kj}}(t) \\
&+ h^{\mathrm{se},(\mathrm{HF})}_{\underline{ik}}(t)G^{\mathrm{es},<}_{\underline{kj}}(t) - G^{\mathrm{se},<}_{\underline{ik}}(t)h^{\mathrm{es},(\mathrm{HF})}_{\underline{kj}}(t)\Big) \\
= i\hbar\frac{\partial}{\partial t}G^{\mathrm{ss},<}_{\underline{ij}}(t) - &\left[\boldsymbol{h}^{\mathrm{ss},(\mathrm{HF})}, \boldsymbol{G}^{\mathrm{ss},<}\right]_{\underline{ij}}(t) - \underbrace{\sum_{\underline{k}} h^{\mathrm{se},(\mathrm{HF})}_{\underline{ik}}(t)G^{\mathrm{es},<}_{\underline{kj}}(t)}_{\boldsymbol{I}^{\mathrm{ss},\mathrm{emb}}(t)} + \underbrace{\sum_{\underline{k}} G^{\mathrm{se},<}_{\underline{ik}}(t)h^{\mathrm{es},(\mathrm{HF})}_{\underline{kj}}(t)}_{\boldsymbol{I}^{\mathrm{ss},\mathrm{emb},\dagger}(t)},
\end{aligned}$$

Thus, in total, we get

$$\Leftrightarrow i\hbar\frac{\partial}{\partial t}G^{\mathrm{ss},<}_{\underline{ij}} - \left[\boldsymbol{h}^{\mathrm{ss},(\mathrm{HF})}, \boldsymbol{G}^{\mathrm{ss},<}\right]_{\underline{ij}}(t) = \left[\boldsymbol{I}(t) + \boldsymbol{I}^{\dagger}(t)\right]^{\mathrm{ss}}_{\underline{ij}} + \left[\boldsymbol{I}^{\mathrm{emb}}(t) + \boldsymbol{I}^{\mathrm{emb},\dagger}(t)\right]^{\mathrm{ss}}_{\underline{ij}},$$

which is equivalent to the EOM derived from the NEGF approach Eq. (2.10). The remaining components can be inferred analogously

$$\begin{aligned}
i\hbar\frac{\partial}{\partial t}G^{\mathrm{ee},<}_{\underline{ij}}(t) - \left[\boldsymbol{h}^{\mathrm{ee},(\mathrm{HF})}, \boldsymbol{G}^{\mathrm{ee},<}\right]_{\underline{ij}}(t) &= \left[\boldsymbol{I}(t) + \boldsymbol{I}^{\dagger}(t)\right]^{\mathrm{ee}}_{\underline{ij}} \\
&\quad + \sum_{\underline{k}}\left(h^{\mathrm{es},(\mathrm{HF})}_{\underline{ik}}(t)G^{\mathrm{se},<}_{\underline{kj}}(t) - G^{\mathrm{es},(\mathrm{HF})}_{\underline{ik}}(t)h^{\mathrm{se},(\mathrm{HF})}_{\underline{kj}}(t)\right) \\
&=: \left[\boldsymbol{I}(t) + \boldsymbol{I}^{\dagger}(t)\right]^{\mathrm{ee}}_{\underline{ij}} + \left[\boldsymbol{I}^{\mathrm{emb}}(t) + \boldsymbol{I}^{\mathrm{emb},\dagger}(t)\right]^{\mathrm{ee}}_{\underline{ij}}, \\
i\hbar\frac{\partial}{\partial t}G^{\mathrm{es},<}_{\underline{ij}}(t) &= \left[\boldsymbol{I}(t) + \boldsymbol{I}^{\dagger}(t)\right]^{\mathrm{es}}_{\underline{ij}} + \sum_{\underline{k}}\left(h^{\mathrm{es},(\mathrm{HF})}_{\underline{ik}}(t)G^{\mathrm{ss},<}_{\underline{kj}}(t) + h^{\mathrm{ee},(\mathrm{HF})}_{\underline{ik}}(t)G^{\mathrm{es},<}_{\underline{kj}}(t)\right) \\
&\quad - \sum_{\underline{k}}\left(G^{\mathrm{es},<}_{\underline{ik}}(t)h^{\mathrm{ss},(\mathrm{HF})}_{\underline{kj}}(t) + G^{\mathrm{ee},(\mathrm{HF})}_{\underline{ik}}(t)h^{\mathrm{es},(\mathrm{HF})}_{\underline{kj}}(t)\right) \\
&=: \left[\boldsymbol{I}(t) + \boldsymbol{I}^{\dagger}(t)\right]^{\mathrm{es}}_{\underline{ij}} + \left[\boldsymbol{I}^{\mathrm{emb}}(t) + \boldsymbol{I}^{\mathrm{emb},\dagger}(t)\right]^{\mathrm{es}}_{\underline{ij}}.
\end{aligned}$$

By comparing the equations to Eqs. (2.11) and (2.12), it should become clear that they are almost equivalent. The only difference is the appearance of the collision integrals I^{ee} and I^{es}, which were previously removed by choosing a specific ansatz for the self-energies in these subspaces. So in this case, to achieve the same results as in the previous section, we neglect all collision integrals except for I^{ss}, which takes the usual form

$$I^{\mathrm{ss}}_{ij}(t) = (i\hbar)^2 \sum_{klp} w_{iklp}(t)\mathcal{G}_{lpjk}(t),$$

with the equation of motion

$$i\hbar\frac{\partial}{\partial t}\mathcal{G}_{ijkl} - \left[\boldsymbol{h}^{(2),(\mathrm{HF})}, \boldsymbol{\mathcal{G}}\right]_{ijkl}(t) = C_{ijkl}(t).$$

It is apparent that, in the general case, this is a quite severe approximation, as we did not only neglect the collision integrals but also the coupling between the subspaces in the EOM for $\mathcal{G}$. The treatment is analogous to the non-embedding case and therefore represents the approximation of only including correlational effects in the system. However, the magnitude of the deviation is not quantified in this approach and should therefore be tested for each specific case. A more thorough study of the different collision integrals and the complete EOMs that include all the $\mathcal{G}^{\mathrm{ssss}}$, $\mathcal{G}^{\mathrm{eses}}$ and so on, should be performed in order to make this approach more systematic. For the time being, we will use these equations in the G1–G2 embedding framework in the following chapter applied to the aforementioned ion stopping scenario.

3 Ion stopping with charge transfer

In this chapter, we will describe how the G1–G2 embedding scheme is applied to the specific situation of electronic stopping of slow moving, highly charged ions in graphene and molybdenum disulfide (MoS_2) monolayers with an explicit model for the charge transfer between the two systems. The specific lattice model chosen for the materials as well as the parameters for the ion energy levels and the modeling of the charge transfer are presented in Sec. 3.1. The model presented there was developed in Ref. [28] and subsequently used in Ref. [16]. We will then go on to present our simulation results by starting with an ion velocity dependency study of the total charge transfer in Sec. 3.2 and compare the results to experimental data from Refs. [29, 30]. Following that, we will discuss charge density profiles in the monolayers during the interaction with the ion in Sec. 3.3 and link the observations to the emission of secondary electrons in Sec. 3.4. Finally, we will present spectral information about the electronic system in Sec. 3.5 using the Koopmans' theorem [31].

3.1 Introduction

The goal of this work is to accurately simulate the ultrafast electron dynamics in response to a strong excitation of effective two dimensional materials. The specific situation is modeled after a set of experiments [16, 29, 30], in which the authors were able to radiate free standing single layer graphene crystals (SLG) with highly charged, slow moving Xenon ions. In addition to SLG, monolayers of the popular transition metal dichalcogenite (TMDC) MoS_2 were also used as targets for the ion beam. 2D materials such as SLG and TMDCs have drawn significant interest since the discovery of the exfoliation technique [32], which allows for the conistent production of single atom layers of graphene. In such a monolayer, the orbitals of the carbon atoms hybridize to produce three sp^2 and one 2p orbital. While the electrons in the sp^2 orbitals form the strong, planar σ-bonds, the 2p orbitals form the effectively delocalised π bonds in which the electrons are able to move across the crystal, giving rise to the conductive properties of SLGs. In recent years, techniques for the synthesis of TMDCs have also been developed. TMDCs consist of an alternating, three layer structure made up of triagonal lattices stacked on top of each other. These three layers are held together by strong ionic-covalent bonds between the transition metal and the chalcogenide atoms.

However, while the conduction and valence bands form the famous Dirac cones in SLG leading to the high carrier mobility, TMDCs in general form a bandgap. In fact, it was discovered that, monolayers of MoS_2 exhibit semiconducting properties, with a direct band gap in the visible range [33].

To calculate the electron dynamics in condensed matter, we have to first find a suitable basis, since the physical orbitals in solid matter can be highly complex or might not even have an analytical expression. A good approximation for systems that can be interpreted as having some kind of discretization in space is the Tight-Binding (TB) framework. It describes the electrons as being localized at the atoms of the crystal and approximates the overlap of neighboring orbitals as well as the kinetic energy of the electrons in terms of a hopping operator. The Hamiltonian in the TB framework reads

$$\hat{H} = \sum_{i,\sigma} \epsilon_i \hat{c}^\dagger_{i,\sigma} \hat{c}_{i,\sigma} + \sum_{i,j,\sigma} t_{ij} \hat{c}^\dagger_{i,\sigma} \hat{c}_{j,\sigma},$$

where σ is the spin and can either be up ($\uparrow$) or down ($\downarrow$). The matrix-elements t_{ij} represent the hopping amplitude while ϵ_i represent an on site energy contribution due to the potential of the atom. The basis states $|i\rangle$ are the so-called sites of the lattice, given by the positions of the atoms. When describing a single band system, such as the π electrons in SLGs, an even stronger approximation suffices, in which we write the hopping matrix and the on-site energy as

$$t_{ij} = -J\delta_{\langle i,j \rangle}, \quad \epsilon_i = \epsilon.$$

Here we introduced the hopping amplitude J and the nearest neighbor Kronecker symbol $\delta_{\langle i,j\rangle}$, indicating that only electron transitions to the next nearest neighbor in the crystal lattice are allowed.[1] The main influence on the physical properties of the model is then given by the lattice geometry. One such physical property that contains a lot of information about the lattice is the so-called Density of States (DOS), which is given by the spectrum of the Hamiltonian of the system, i.e. the eigenvalues of the Hamiltonian in a given basis. For an infinite lattice we can perform a transformation of basis from the spatial basis to the k-space basis via a spatial Fourier transform of the form

$$\langle k_1|\,\hat{H}\,|k_2\rangle = \frac{1}{V}\sum_{n,m} e^{-i(k_1 r_n - k_2 r_m)}\,\langle r_n|\,\hat{H}\,|r_m\rangle\,.$$

The k-space basis is exceptionally useful for infinite lattices, since the TB Hamiltonian is diagonal in such a basis. Therefore, we can find the dispersion relation of for example the honeycomb lattice [34]

$$\langle\hat{H}\rangle\,(k) = \pm J\sqrt{3 + 2\cos\left(\sqrt{3}k_y\right) + 4\cos\left(\frac{\sqrt{3}}{2}k_y\right)\cos\left(\frac{3}{2}k_x\right)}.$$

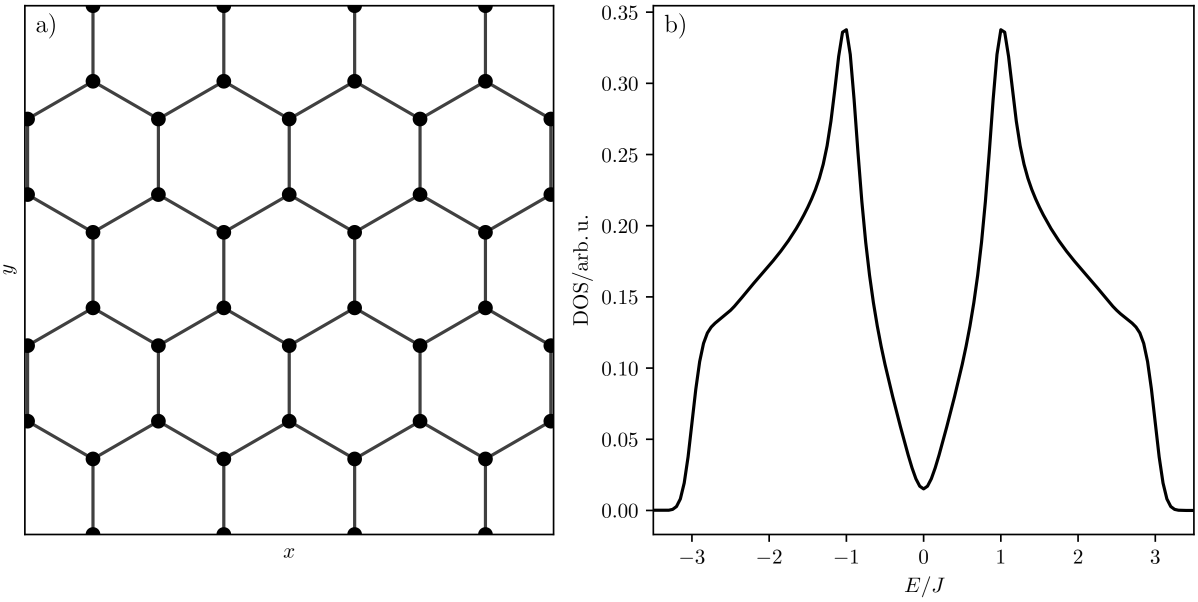

Figure 3.1: TB density of states of the infinite honeycomb lattice. Panel a) displays the spatial lattice structure with the lattice sites as black dots and the nearest neighbor connections as solid, black lines. Panel b) shows the resulting DOS calculated from the TB Hamiltonian. The energy is given in units of the hopping amplitude J.

To obtain the DOS from this expression, we can calculate the dispersion relation on a k grid and then integrate over the first Brillouin zone. The resulting energy spectrum is shown in Fig. 3.1, b)[2] and the spatial lattice structure is shown in Fig. 3.1, a). The bandwidth depends solely on the hopping amplitude J and at $E = 0$ we find the famous Dirac cone of graphene.

A downside to these analytical results is that they do not allow for an integration of inhomogeneous excitations, such as the impact of a highly charged ion in the monolayer. One way to solve this problem is to use a periodic structure, in which supercells that contain the inhomogeneous excitation are repeated. However, in this work, we will focus on finite sized monolayer clusters. By using the TB approach we are not limited to periodic structure but can also calculate physical properties of finite clusters directly in the spatial basis.

---

[1] We will see later in Ch. 4, how such a simple model can be expanded to capture more of the actual band structure

[2] Note that the peaks in the spectrum were artificially broadened

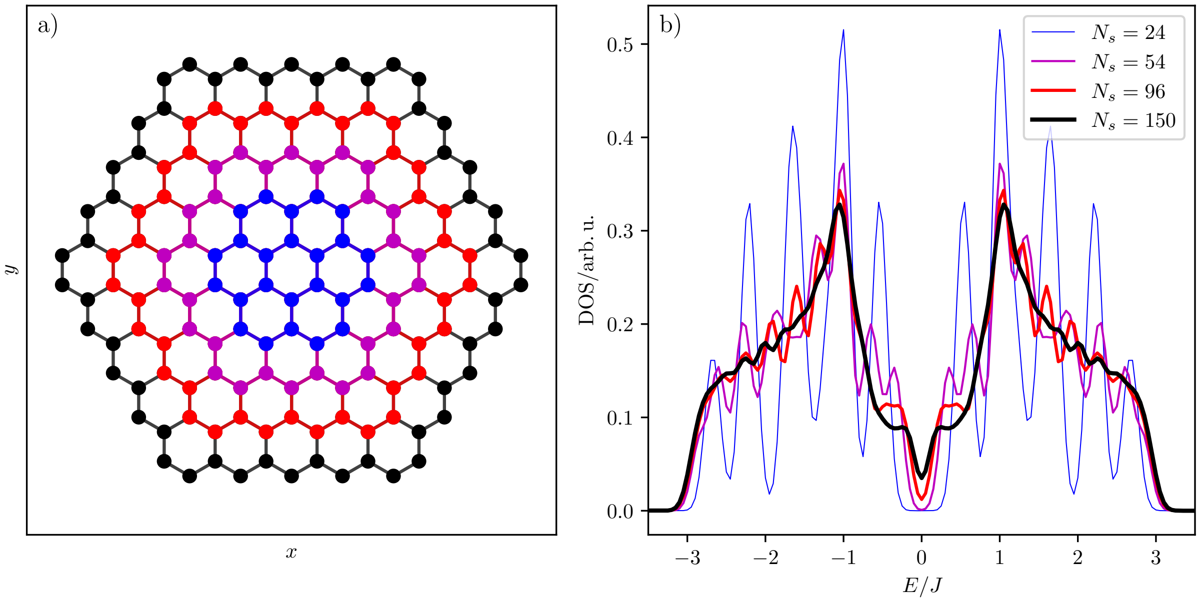

Figure 3.2: TB density of states for finite honeycomb clusters. Panel a) displays the spatial lattice structures for four flake sizes. Panel b) displays the DOS corresponding to the TB Hamiltonian solved for the different flake sizes. The energy is given in units of the hopping amplitude J.

In Fig. 3.2, a) honeycomb flakes of different sizes are displayed, accompanied by their respective DOS in Fig. 3.2, b), which can be calculated by diagonalizing the TB Hamiltonian in the spatial basis. It is apparent that the DOS differs significantly from the DOS of the infinite lattice. This is due to the influence of the edges of the lattice. However, by increasing the system size, we find that the DOS converges towards the DOS of the infinite lattice, with remnants stemming from so-called edgestates. If we want to compare our simulation results to experimental measurements with macroscopic monolayers, we have to acknowledge the fact that these will resemble the infinite lattice more closely. This is because macroscopic flakes are significantly larger than the interatomic distance of $\sim$ Å with diameters in the range of $\sim \mu$m. It is therefore apparent that we will need to simulate the largest possible systems, since in those the relative contributions of the edgestates compared to the bulk states become negligible. However, since the spatial basis size N_s scales with the system size, we face serious computational limitations when propagating $N_s \times N_s$ density matrices or in the case of higher order approximations $N_s \times N_s \times N_s \times N_s$ correlation functions. Therefore, the scope of this work is limited to systems of up to $N_s = 150$.

As a next step, we want to include Coulomb type interactions between the electrons. Since these interactions are completely neglected in the TB framework and the full treatment of the pairwise Coulomb interaction is costly, we can compromise with an approximative treatment of the interaction via the Hubbard model [35]. To do so, we extend the TB Hamiltonian with an additional term

$$\hat{H} = \epsilon \sum_{i,\sigma} \hat{c}^\dagger_{i,\sigma} \hat{c}_{i,\sigma} - J \sum_{\langle i,j \rangle,\sigma} \hat{c}^\dagger_{i,\sigma} \hat{c}_{j,\sigma} + U \sum_i \hat{n}_{i,\uparrow} \hat{n}_{i,\downarrow},$$

which corresponds to an energy contribution on each site, proportional to the product of the density operators $\hat{n}$ on the site.[3] This specific choice of the interaction already accounts for Pauli's principle by only allowing for electrons of different spins on the same site.[4] This addition to the model, that resembles a highly localized interaction, has a remarkable predictive power in quantum-mechanical systems with a finite basis. This model is used in ultracold atoms [37] and condensed matter [38] and can serve as a test bed for methodological studies [39]. Although the addition seems straight forward, analytical solutions only exist for very simple systems such as the 1D finite Hubbard chain [40].

To describe real materials with the Hubbard model,[5] we have to choose appropriate values for ϵ, J and U. The typical procedure to find optimal values is to calculate some observable, such as the band structure

---

[3] Note that the density operator is nothing more than the diagonal of the 1-pRDM we discussed in Sec. 2.2.

[4] Different versions of the Hubbard interaction without explicit Pauli blocking are also used [36].

[5] In the following we will refer to the TB model + Hubbard interactions simply as the Hubbard model.

or the DOS and compare them to experimental or more likely density functional theory calculations. For SLG and MoS_2 we use the values from Ref. [16], which are shown Tab. 3.1.

Material	ϵ/J_0	J/J_0	U/J_0	a/a_0
SLG	1.22	0.74	1.19	1
MoS_2	1.19	0.29	1.19	1.29

Table 3.1: Material parameters taken from Ref. [16]. ϵ, J_0 and U carry the unit of energy and are given in the scale of $J_0 = \frac{\hbar^2}{m_e a_0^2} \approx 3.78\,\text{eV}$, with the electron mass m_e and the carbon-carbon bond length $a_0 \approx 1.42\,\text{Å}$. a is the interatomic distance in both materials.

We can already observe the key difference between SLG and MoS_2 in this model. The electron mobility, which is represented by the hopping amplitude J, is much smaller in MoS_2 than in SLG. Another key difference between the two materials is the spacing of the atoms in the lattice. While in SLG the interatomic distance is $a_{\text{SLG}} = a_0 \approx 1.42\,\text{Å}$, which is the carbon-carbon bond length, the spacing between atoms in MoS_2 is much larger with $a_{\text{Mos}_2} \approx 1.29a_0$.

In order to include the highly charged ion (HCI) as an excitation in the model, we extend the Hubbard model with four additional terms, following the argumentation in Ref. [28]. First, we introduce the external Coulomb potential of the ion

$$w[\boldsymbol{r}, \boldsymbol{S}(t)] = -\frac{Z_0 W_0 a_0}{|\boldsymbol{r} - \boldsymbol{S}(t)|}, \quad \boldsymbol{S}(t) = (z_0 + v_0 t)\boldsymbol{e}_z,$$

with the charge of the ion Z_0 and the rescaled Coulomb constant $W_0 = e^2/(4\pi\epsilon_0 a_0) \approx 2.68J_0$. The potential is a function of the parametrized trajectory of the ion $\boldsymbol{S}(t)$, which in this work will be a straight line trajectory, starting at $(0, 0, z_0)^T$, with a constant velocity $(0, 0, v_0)^T$ and passing the plane of the lattice at $(0, 0, 0)^T$. This external potential disturbs the electronic structure of the system, by changing the orbitals of the electrons. We can approximate this effective with a diagonal contribution

$$W_{ii}[\boldsymbol{S}(t)] \approx w[\boldsymbol{r}_i, \boldsymbol{S}(t)],$$

corresponding to a reduction of the on-site energy due to the attractive Coulomb potential and a non-diagonal contribution, stemming from the change in the overlap of neighboring orbitals

$$W_{ij}[\boldsymbol{S}(t)] = \frac{\lambda}{2}\big(w[\boldsymbol{r}_i, \boldsymbol{S}(t)] + w[\boldsymbol{r}_j, \boldsymbol{S}(t)]\big).$$

For the overlap integral λ we use the value from Ref. [28] of $\lambda = 0.153$ for both materials in Sec. 3.2. In the later parts of this work (Sec. 3.4) we use, in order to compare our results to the findings of Ref. [16], $\lambda = 0$, effectively neglecting the effect of the off-diagonal contributions of the ion.

To describe both the cluster (from hereon called the system s) and the ion (the environment e) we will make use of the embedding scheme (see Sec. 2.3), by separating the basis into system states $|i\rangle$, $i \in s$ and environment states $|k\rangle \in e$. The system Hamiltonian is then given by

$$\hat{H}^{\text{ss}} = \sum_{i \in s, \sigma} \big(\epsilon - W_{ii}[\boldsymbol{S}(t)]\big)\hat{c}^\dagger_{i,\sigma}\hat{c}_{i,\sigma} + \sum_{\langle i,j\rangle \in s, \sigma} \big(W_{ij}[\boldsymbol{S}(t)] - J\big)_{ij}\hat{c}^\dagger_{i,\sigma}\hat{c}_{j,\sigma} + U\sum_{i \in s}\hat{n}_{i,\uparrow}\hat{n}_{i,\downarrow}.$$

Next, in order to allow for the transfer of electrons between the cluster and the environment, we introduce the charge transfer term, which couples the system (i.e. the cluster) to the environment (i.e. the ion) and allows for the exchange of electrons. To simplify the model, we use an approximate approach to describe this, in general highly complex, interaction

$$\gamma[\boldsymbol{S}(t)] = \gamma_0 \exp\left(-\frac{\big(z(t) + z_{\text{res}}\big)^2}{2d_{\text{w}}^2}\right)J_0, \tag{3.1}$$

which is a Gaussian function of the z-coordinate of the ion trajectory with a width of d_{w} and peaked around a resonant distance z_{res}. The amplitude γ_0 was used as a fit parameter in Ref. [28], to reproduce experimental charge transfer data from [29]. Also the remaining parameters $d_{\text{w}} = 0.6a_0$ and $z_{\text{res}} = -\sqrt{3}a_0$ were chosen such that the neutralization of the HCI qualitatively matches experimental observations.

The system-environment Hamiltonian is then given by

$$\hat{H}^{\text{se}} = \gamma[\boldsymbol{S}(t)]\sum_{i \in s,\sigma}\sum_{k \in e}\hat{c}^\dagger_{i,\sigma}\hat{a}_{k,\sigma}, \quad \hat{H}^{\text{es}} = \gamma[\boldsymbol{S}(t)]\sum_{k \in e}\sum_{i \in s}\hat{a}^\dagger_{k,\sigma}\hat{c}_{i,\sigma},$$

where the operator $\hat{a}^{(\dagger)}$ is the annihilation (creation) operator for electrons in the environment. The only missing term is the environment Hamiltonian, describing the orbital structure of the ion. Again, to keep the model simple, we will follow the approximation taken in Ref. [28], where the authors used the modified on-site energy at the point of resonant charge transfer as the on-site energy of the environment

$$\hat{H}^{\mathrm{ee}} = \tilde{\epsilon} \sum_{k \in e, \sigma} \hat{a}^{\dagger}_{k,\sigma} \hat{a}_{k,\sigma}, \quad \tilde{\epsilon} = -\frac{Z_0 W_0}{\sqrt{1 + z_{res}^2 / a_0^2}} - \epsilon = -\frac{Z_0 W_0}{2} - \epsilon$$

and no additional contributions, meaning that the electrons in the environment can not move around. Also notice that neither the *ee* nor the *es* Hamiltonian include interactions between the electrons, since we want to treat both the charge transfer, as well as the ion, uncorrelated.
With all terms in place, we can now use the embedding G1–G2 scheme (see Sec. 2.3) to derive the EOMs for the coupled system in SOA[6]

$$\begin{aligned}
i\hbar \frac{\partial}{\partial t} G^{\mathrm{ss},<}_{ij}(t) - \left[\boldsymbol{h}^{\mathrm{ss},(\mathrm{HF})}, \boldsymbol{G}^{\mathrm{ss},<}\right]_{ij}(t) &= \left[\boldsymbol{I}^{\mathrm{emb}}(t) + \boldsymbol{I}^{\mathrm{emb},\dagger}(t)\right]^{\mathrm{ss}}_{ij} + \left[\boldsymbol{I}(t) + \boldsymbol{I}^{\dagger}(t)\right]_{ij}, \\
i\hbar \frac{\partial}{\partial t} G^{\mathrm{es},<}_{kj}(t) &= \sum_{i \in s} h^{\mathrm{es}}_{ki}(t) G^{\mathrm{ss},<}_{ij}(t) + \sum_{l \in e} h^{\mathrm{ee}}_{kl}(t) G^{\mathrm{es},<}_{lj}(t) \\
&\quad - \sum_{i \in s} G^{\mathrm{es},<}_{ki}(t) h^{\mathrm{ss}}_{ij}(t) - \sum_{l \in e} G^{\mathrm{ee},<}_{kl}(t) h^{\mathrm{es}}_{lj}(t), \\
i\hbar \frac{\partial}{\partial t} G^{\mathrm{ee},<}_{kl}(t) - \left[\boldsymbol{h}^{\mathrm{ee}}, \boldsymbol{G}^{\mathrm{ee},<}\right]_{kl}(t) &= \left[\boldsymbol{I}^{\mathrm{emb}}(t) + \boldsymbol{I}^{\mathrm{emb},\dagger}(t)\right]^{\mathrm{ee}}_{kl}, \\
i\hbar \frac{\partial}{\partial t} \mathcal{G}_{i_1 j_1 i_2 j_2} - \left[\boldsymbol{h}^{(2),(\mathrm{HF})}, \boldsymbol{\mathcal{G}}\right]_{i_1 j_1 i_2 j_2}(t) &= \frac{1}{2} \delta_{i_1 j_1} U G^{\mathrm{ss},<}_{i_1 i_2}(t) G^{\mathrm{ss},<}_{j_1 j_2}(t) + i\hbar U G^{\mathrm{ss},<}_{j_1 i_1}(t) G^{\mathrm{ss},<}_{i_1 i_2}(t) G^{\mathrm{ss},<}_{i_1 j_2}(t).
\end{aligned}$$

with

$$\begin{aligned}
&h^{\mathrm{ss},(\mathrm{HF})}_{ij}(t) = \big(\epsilon - W_{ii}[\boldsymbol{S}(t)]\big)\delta_{i,j} + \big(W_{ij}[\boldsymbol{S}(t)] - J\big)\delta_{\langle i,j \rangle} + U n^{\mathrm{ss}}_i(t) \delta_{i,j}, \; h^{\mathrm{ee}}_{kl} = \tilde{\epsilon} \delta_{k,l}, \; h^{\mathrm{se}}_{ik}(t) = \gamma[\boldsymbol{S}(t)] \delta^{\mathrm{CT}}_{i,k}, \\
&I^{\mathrm{emb},\mathrm{ss}}_{ij}(t) = \sum_{k \in e} h^{\mathrm{se}}_{ik}(t) G^{\mathrm{es},<}_{kj}(t), \; I^{\mathrm{emb},\mathrm{ee}}_{kl}(t) = \sum_{i \in s} h^{\mathrm{es}}_{ki}(t) G^{\mathrm{se},<}_{il}(t), \; I^{\mathrm{ss}}_{ij}(t) = -i\hbar U \mathcal{G}_{iiji}(t), \\
&h^{(2)}_{i_1 j_1 i_2 j_2}(t) = \delta_{j_1 j_2} h^{\mathrm{ss},(\mathrm{HF})}_{i_1 i_2}(t) + \delta_{i_1 i_2} h^{\mathrm{ss},(\mathrm{HF})}_{j_1 j_2}(t).
\end{aligned}$$

We also introduced the charge transfer delta function δ^{CT}, that will determine which system sites couple to which environment sites and therefore contribute to the charge transfer.

---

[6] Note that we have neglected the spin indices, since in all further calculations, we will assume spin symmetry with $G_{\uparrow\uparrow} = G_{\downarrow\downarrow}$ and $G_{\uparrow\downarrow} = G_{\downarrow\uparrow} = 0$. This assumption is reasonable, since the model does not allow for spin flips.

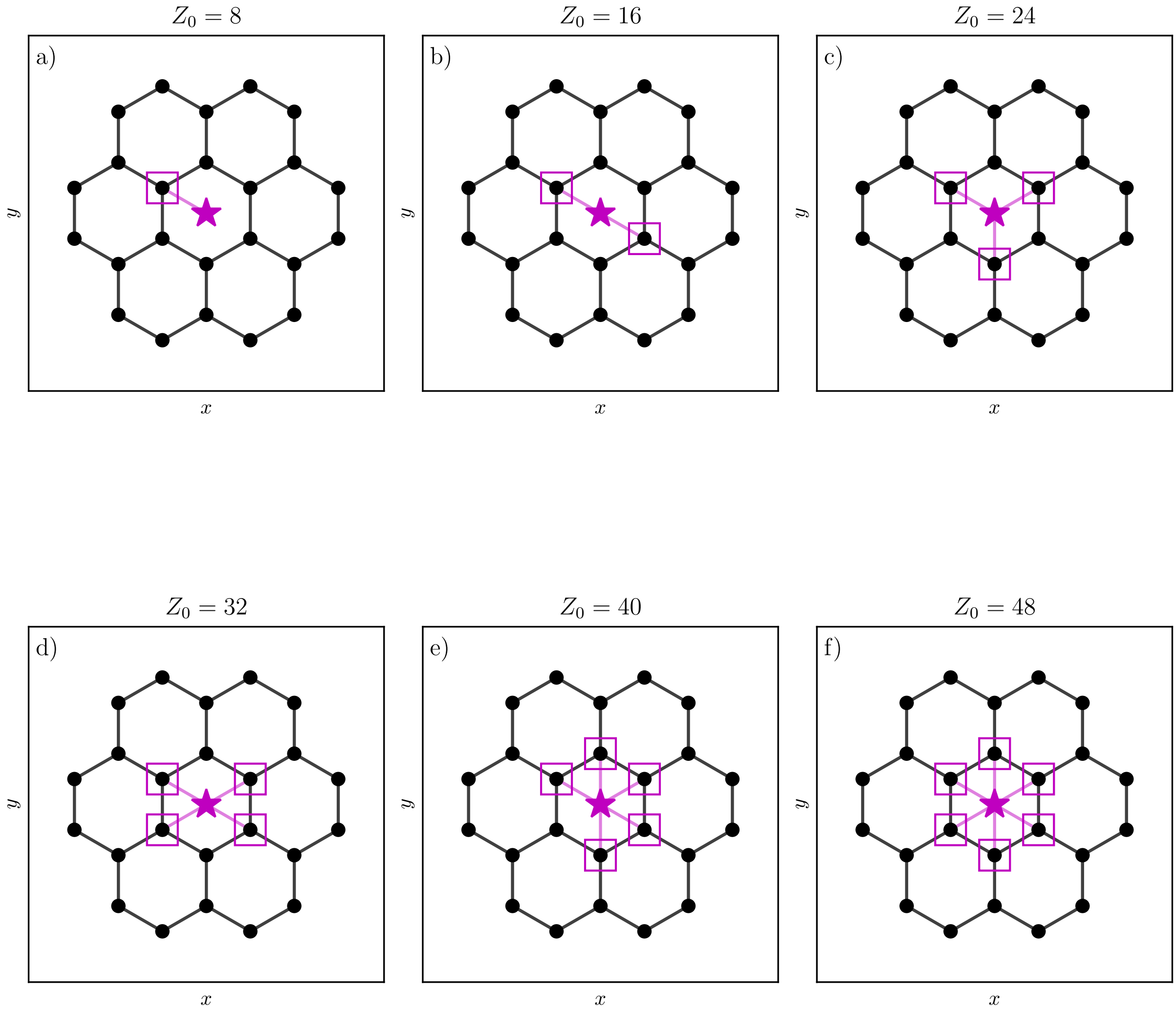

Figure 3.3: Visualization of the charge transfer delta function δ^{CT}. The ion passing through the center of the honeycomb cluster is marked by a purple star, while the charge transfer channels are indicated by purple lines. On the cluster site each coupled atom is marked by a purple square. Panels a)-f) show the different coupling schemes for different initial charge states of the ion.

To make a reasonable choice for the charge transfer delta function, the authors in Ref. [28] presented the following argument:
At each site in the SLG,[7] there are eights orbitals in total, the three sp^2 σ bands and the 2p π band, multiplied by the two possible spin channels. The authors argue that all four bands can be approximated by four, non-interacting bands, each of which can be modeled with the above described Hamiltonian. Now, since the ion sites start initially unoccupied and can hold up to two electrons (spin up + spin down), the authors introduce $Z_0/8$ charge transfer channels via the δ^{CT} function. Each of the transfer channels includes one central site of the cluster and one site on the ion. Fig. 3.3 shows how these charge transfer channels are realized for different initial charge states of the ion. The ion is placed at the center of the cluster, indicated by the purple star, the charge transfer channels are indicated by the purple lines

---

[7] SLGs are used here for the argumentation. The same procedure is used for MoS_2 even if the arguments are not directly applicable.

and the coupled cluster sites are marked by purple squares. Note that for each line in the diagram, a separate level on the ion is introduced. This setup allows for the complete neutralization[8] of the ion by transferring exactly Z_0 electrons to the environment.
All simulations for this work were performed using a Runge-Kutta method of order 4 (for a review of the method see [41]) with a time step of $\Delta t = 0.01 t_0$, $t_0 = \hbar/J_0 \approx 0.17\,\mathrm{fs}$. Initially the state was prepared as the half filled TB groundstate after which the interacting ground state was obtained via adiabatic switching.

3.2 Velocity dependency of the total charge transfer

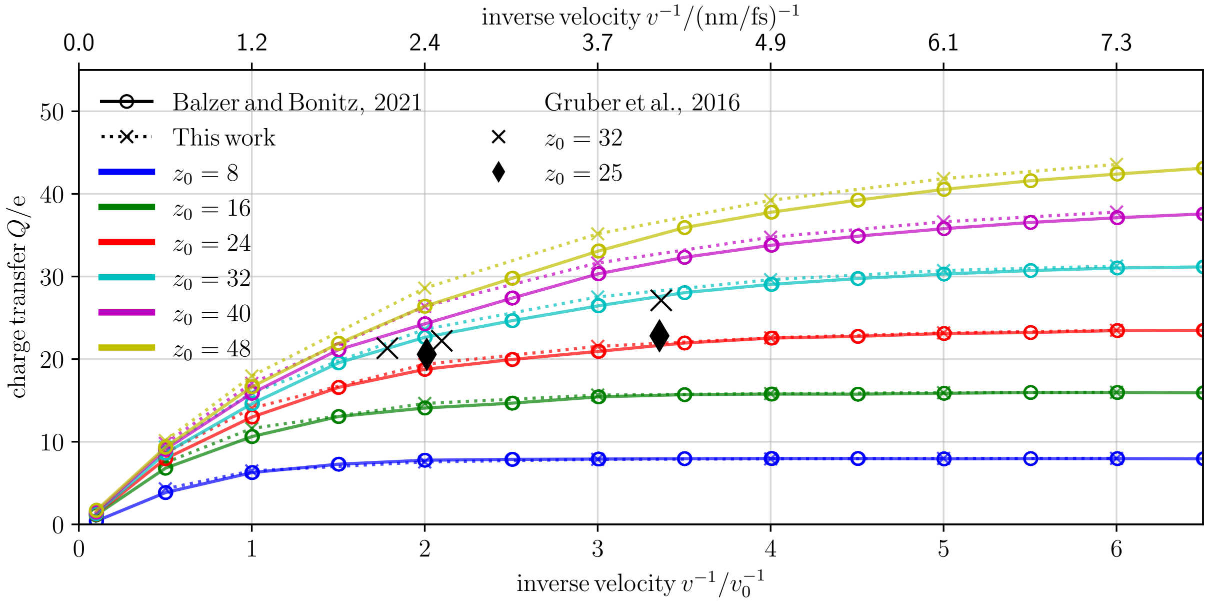

Figure 3.4: Total charge transfer in SLG targets as a function of the inverse velocity of Xe ions for different initial charge states. Solid lines give the NEGF results from Ref. [28], while dashed lines give our results obtained from the time-local embedding scheme. Both data are compared to the experimental results from [29]. Aside from the velocity and charge states of the ion, the simulation parameters are found in Tab. B.1. The velocity on the bottom axis is given in units of $v_0 = 0.82\,\mathrm{nm/fs}$.

In order to determine the last parameters, the charge transfer amplitude γ_0 of the model (Eq. (3.1)), the authors in Ref. [28] performed an extensive parameter study of the velocity dependency of the total charge transfer

$$Q = 4\big(N_\mathrm{s} - \langle \hat{N} \rangle (t \to +\infty)\big),$$

in which N_s is the number of sites in the system, which is for a half filled initial state, equal to the total number of electrons (spin up + spin down). The particle number operator

$$\langle \hat{N} \rangle (t) = \sum_{i \in s, \sigma} \hat{n}_{i,\sigma}(t),$$

is evaluated well after the interaction with the ion is completed, to determine the number of electrons removed from the system by the charge transfer with the ion. The solid lines in Fig. 3.4 show the total charge transfer for different initial charge states and velocities of the ion for $\gamma_0 = 2.12$. The parameter is the result of a fit to the experimental data from Ref. [29] where Xe ions were targeted at an SLG sample and their charge state before and after the impact were measured. The experimental results are indicated by the black symbols in the figure. We compare to our results of the same study performed

---

[8] This neutralization has to be understood only as an interpretation of the reduction of the electron number in the cluster. In all simulations the charge state of the ion is not updated but kept constant.

in the time-local embedding framework, corresponding to the dashed lines in the figure. All calculations were performed on $N_s = 24$ clusters, which were shown already in Fig. 3.3 and in HF approximation. The comparison reveals a good agreement between the computational results of [28] and the experimental data, while the time-local results show slight deviations especially for high velocity ions. Our results agree with the results from Ref. [28] for low ion velocities and low initial charge states where the ion is completely neutralized over the course of the interaction since the interaction time with the cluster increases with the inverse ion velocity.

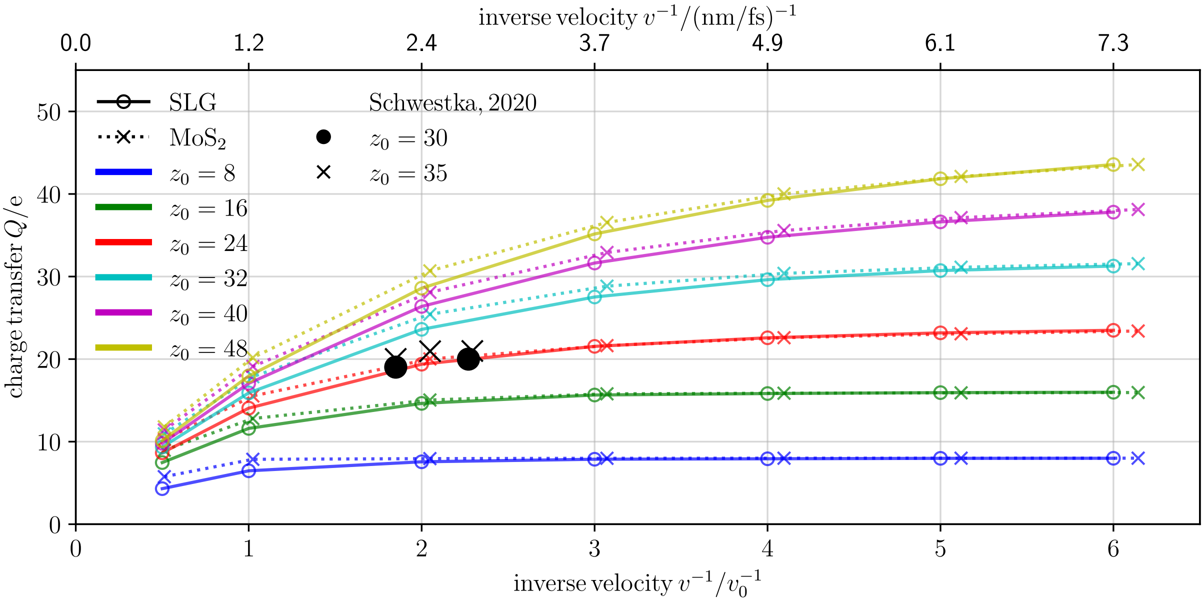

Figure 3.5: Total charge transfer in SLG and MoS$_2$ targets as a function of the inverse velocity of Xe ions for different initial charge states. Solid lines give the SLG results, while dashed lines give the MoS$_2$ results obtained from the time-local embedding scheme. Both data are compared to the experimental results from [30]. Aside from the velocity and charge states of the ion, the simulation parameters are found in Tab. B.2. The velocity on the bottom axis is given in units of $v_0 = 0.82\,\text{nm/fs}$.

In Fig. 3.5, we compare our results for SLG (solid lines) and MoS$_2$ (dashed lines) to test the applicability of the model to MoS$_2$. The black symbols indicate experimental results from Ref. [30], where MoS$_2$ monolayers were used as a target. Our findings indicate that the model has systematic deviations from the experimental results in the form of overestimating the total charge transfer as a function of the initial charge state. Also, despite of the decreased carrier mobility in MoS$_2$, our results indicate that the total charge transfer is larger than for SLG, especially for high velocity ions. This counterintuitive finding, as well as the deviation from the experimental results, indicate that the charge transfer amplitude of $\gamma_0 = 2.12$ is not optimal for MoS$_2$ targets and should probably be lowered.

In addition, we also performed the same study for different cluster sizes and included correlations via SOA, but no significant differences were observed.

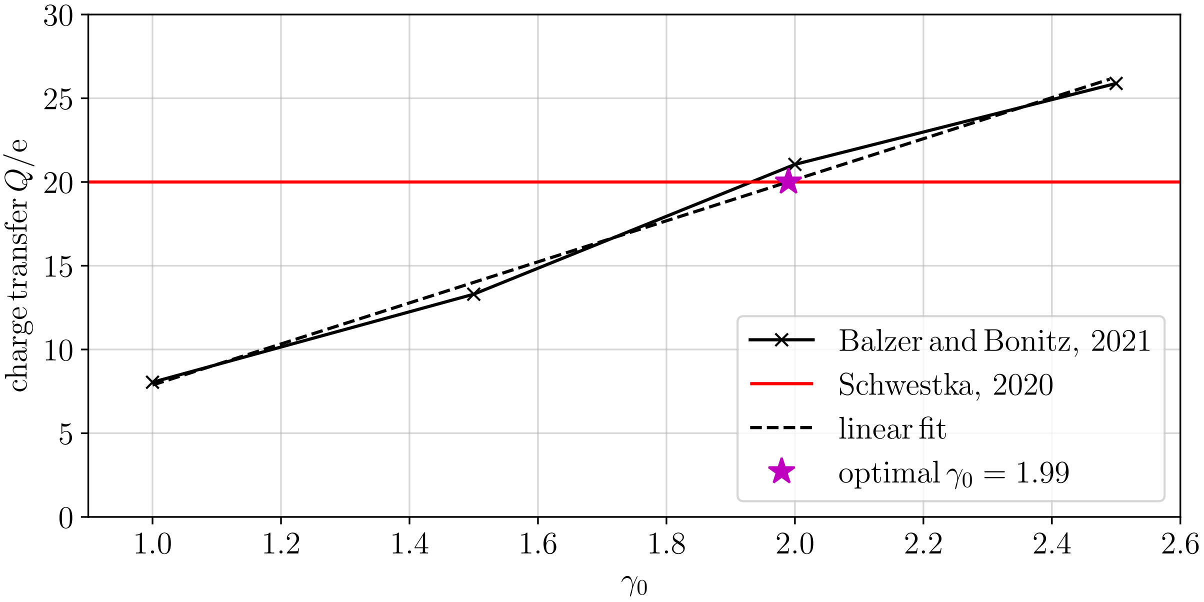

Figure 3.6: Estimate for the correct charge transfer amplitude. Shown are the charge transfer data from [28] (solid black lines with crosses) for a Xe^{+32} ion with an inverse velocity of $v^{-1} = 2v_0$ and a SLG target, for different charge transfer amplitudes. Additionally, a linear fit to the data (black dashed line) is shown. The expected charge transfer from [30] (horizontal red line) is also included for comparison. The intersection of the two curves (purple star) is obtained from the linear fit.

To estimate the correct charge transfer amplitude without performing the complete fit of [28], we first realize, by looking at Fig. 3.5, that the total charge transfer does not differ by much between the two targets in our simulation. Therefore, we take the charge transfer data from Ref. [28] for a Xe^{+32} ion, with an inverse velocity of $v^{-1} = 2v_0$, with SLG as a target but for different charge transfer amplitudes (see solid black line in Fig. 3.6) as a starting point. These datapoints can then be used to try to obtain the correct charge transfer amplitude for MoS_2. One possible way to do so would be to find a simple relation between γ_0 and the charge transfer and then determine the value for which the correct experimental data is reproduced.

The data in Fig. 3.6 allows for a linear fit (dashed black line) and from this fit we can calculate the intersection with the expected charge transfer of around $\sim 20\,\mathrm{e}$ [30]. The optimal charge transfer amplitude of $\gamma_0 = 1.99$, is slightly lower than the one for MoS_2. This is, of course, merely a rough estimate, assuming a linear relation between the charge transfer and γ_0. In order to obtain the best values for γ_0, multiple simulations with MoS_2 targets should be performed and then the charge transfer should be fitted to the experimental data.

3.3 Charge transfer to the ion and electron dynamics in the cluster

One easily accessible output of the G1–G2 scheme is the site resolved density n_i or, in other words, the diagonal of the 1-pRDM (see Sec. 2.2). This is because it is easily calculated from the one-particle Green function

$$n_i(t) = -i\hbar G^{<}_{ii}(t)$$

and can be used to calculate a number of properties of the system. In order to compare our results to Ref. [16],[9] we use the time series of the density in the cluster $n_i^{\mathrm{ss}}(t)$ and take the mean over the honeycomb rings r of the cluster. From this mean density we can calculate the average deviation from

---

[9] Note that the authors in this article used the model described above, but with $\lambda = 0$.

charge neutrality

$$\langle \Delta\rho \rangle_r (t) = 4|e|\bigl(1 - \sum_\sigma n^{\mathrm{ss}}_{r,\sigma}(t)\bigr),$$

which indicates the inhomogeneous charge up or down of the cluster due to the interaction with the ion.

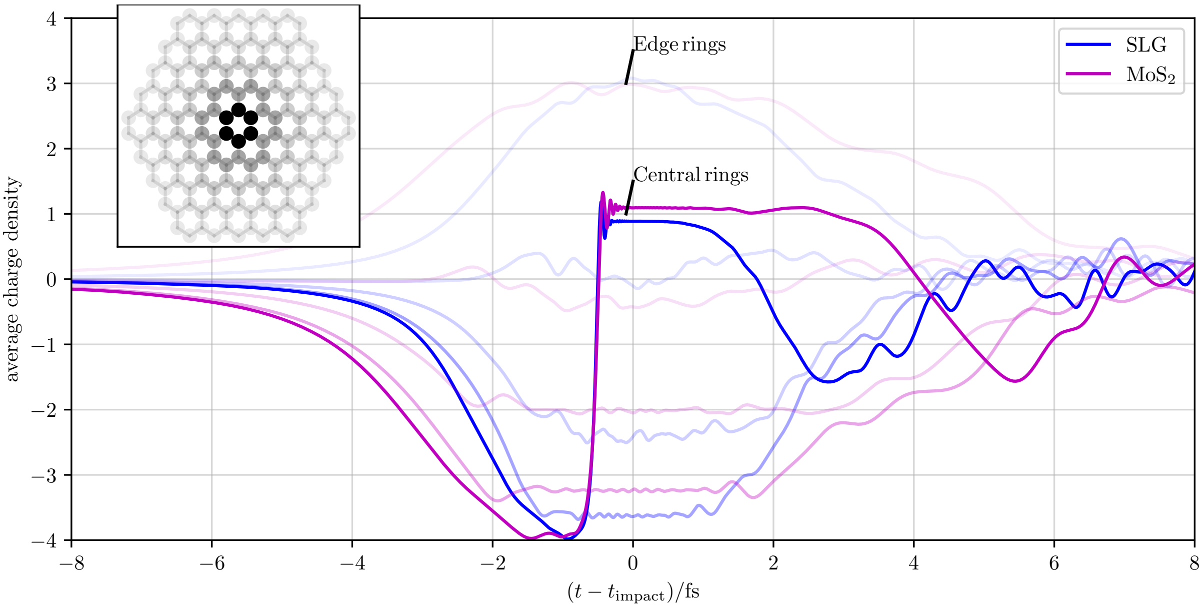

Figure 3.7: Average charge density profiles $\langle \Delta\rho \rangle_r (t)$ resolved for the different honeycomb rings during the interaction with the ion. Compared are the time series for SLG (blue solid lines) and MoS$_2$ (purple solid lines) in HF approximation for a Xe^{+32} ion with a kinetic energy of $E_{\mathrm{ion}} = 113\,\mathrm{keV}$. The opacity of the lines indicates which ring of the cluster is represented, corresponding to the opacity of the atomic sites represented by black dots in the inset. The central rings (outermost rings) are marked explicitly in the figure with the labels "Central rings" ("Edge rings"). The timescale has been shifted such that the ion passes through the plane of the cluster at 0 fs. Parameters for the simulation can be found in Tab. B.3.

In Fig. 3.7 we compare our results for SLG and MoS$_2$ in this manner. The blue (purple) solid lines represent the SLG (MoS$_2$) results, while the opacity of the lines indicates which ring of the cluster is represented. The inset displays the spatial structure of the cluster, with black dots at the atom sites in the lattice and black lines indicating the nearest neighbor connections. The opacity of the dots maps to the opacity of the lines to indicate the respective ring.

The innermost ring is coupled to the ion in the scheme described in Sec. 3.1. The figure presents the results for a Xe^{+32} ion with a kinetic energy of $E_{\mathrm{ion}} = 113\,\mathrm{keV}$. The timescale is shifted, so that the ion passes through the plane of the cluster at 0 fs.

The dynamics start with the accumulation of electrons on the central sites due to the attractive Coulomb potential of the ion, leading to the build up of negative charge in this region. The strength of the potential is large enough to overcome the repulsive Hubbard forces, leading to a larger than half-filled occupation of the central ring. Because of particle number conservation, the outer rings subsequently get depopulated, leading to a positive charge on the edges of the cluster where no new electrons can come in (see Fig. 3.7). Once the point of resonant charge transfer ($z_{\mathrm{res}} = -\sqrt{3}/a_0$) is reached, electrons from the cluster start to transfer to the ion, removing the excess negative charge in the center of the honeycomb almost instantaneously. This sub-femtosecond process is not immediately felt by the rest of the cluster, but propagates in the form of a charge density wave outwards. The free space in the center is then filled by the remaining electrons in the system. Since the system is now slightly below half filling, oscillations of the electron density can be observed.

During the interaction time of the ion with the cluster, which is mainly determined by the velocity of the ion, electrons can transfer back and forth between system and environment. This process results in a dynamic stability of a slight positive charge density in the center of the honeycomb. The charge up of around $\sim 1|e|$ is held constant over a short period of time. The length of that period differs between

SLG and MoS_2. Specifically, the lowered carrier mobility in MoS_2 results in a longer period of positive charge up in the center, due to the increased time it takes the carriers to equilibrate.

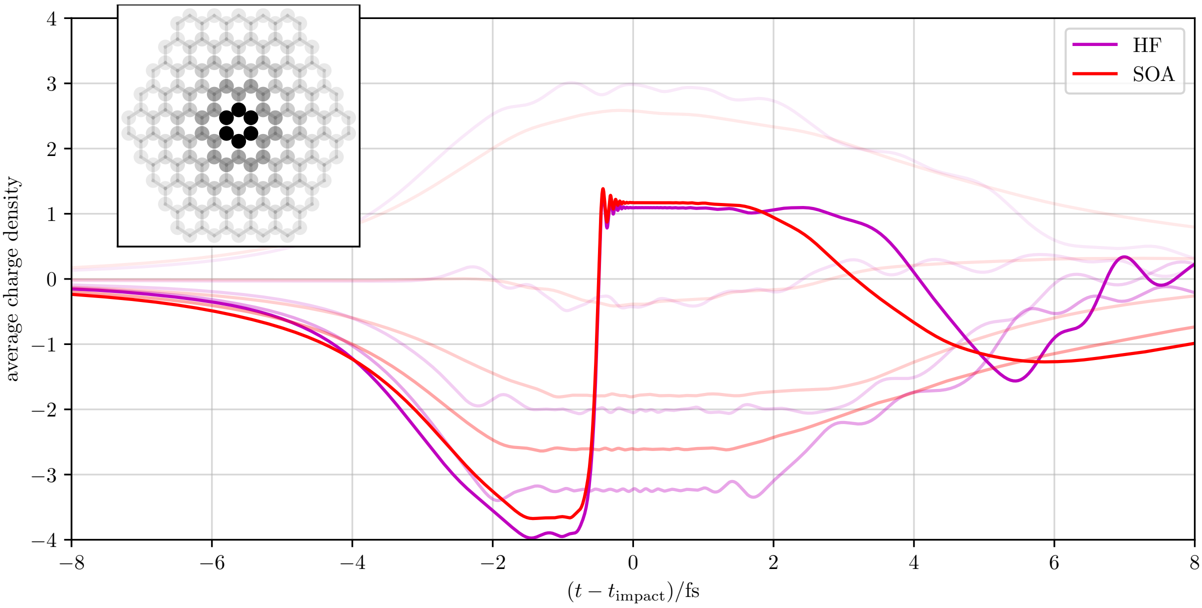

Figure 3.8: Average charge density profiles $\langle \Delta\rho \rangle_r(t)$ resolved for the different honeycomb rings during the interaction with the ion. Compared are the time series for MoS_2 in HF approximation (purple solid lines) and SOA (red solid lines) for a Xe^{+32} ion with a kinetic energy of $E_{\mathrm{ion}} = 113\,\mathrm{keV}$. The opacity of the lines indicates which ring of the cluster is represented, corresponding to opacity of the atomic sites represented by black dots in the inset. The timescale has been shifted such that the ion passes through the plane of the cluster at 0 fs. Parameters for the simulation can be found in Tab. B.4.

In Fig. 3.8 we compare the HF results (purple) to the correlated SOA calculation (red) and find that the inclusions of correlations in the model result in an overall damping of the systems response to the excitation. The period of positive charge up in the center during the interaction time gets reduced, as well as the charge deviations from neutrality on all rings. Furthermore, the high frequency oscillations around the mean of the charge density dynamic on all rings is reduced by the inclusion of correlations.
Another interesting observation can be made by focusing on the initial build up of negative charge in the central ring. In Fig. 3.7, we saw that the accumulation of negative charge occurs much faster for MoS_2 than for SLG. This could be explained by the fact that while the electrons have a higher mobility in SLG, the reduced mobility in MoS_2 results in electrons following the external potential into the center and not being able to tunnel back out due to the low hopping amplitude. Also the increased doublon production rate[10]

$$d_i(t) = G^{(2)}_{iiii}(t) = G^{\mathrm{ss},<}_{ii}(t) G^{\mathrm{ss},<}_{ii}(t) + \mathcal{G}_{iiii}(t),$$

in materials with a high U/J ratio, effectively stabilizes the high occupancy of the central ring. This phenomenon is suppressed by the inclusion of correlations as can be inferred from Fig. 3.8.

---

[10] Doublons refer to the double occupation of a single site.

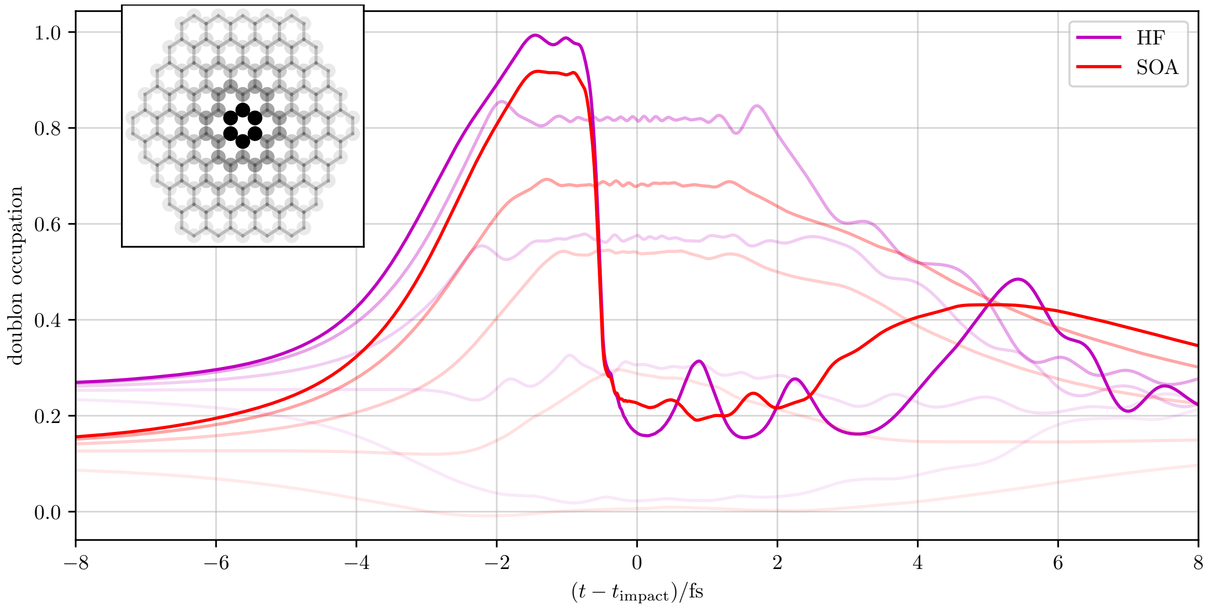

Figure 3.9: Doublon occupation $d_r(t)$ resolved for the different honeycomb rings during the interaction with the ion. Compared are the time series for $\mathrm{MoS_2}$ in HF (purple solid lines) and SOA (red solid lines) approximation. Linestyles and simulation parameters are as in Fig. 3.8.

Fig. 3.9 directly shows the doublon dynamic on the different rings for $\mathrm{MoS_2}$ and we see that it is greatly reduced in the SOA approximation, especially in the inner rings. So while the dynamics in Fig. 3.8 for SOA are qualitatively similar, in that the initial charge up starts faster for $\mathrm{MoS_2}$ than for SLG, the amplitude is then slightly reduced due to the suppression of the doublon production.

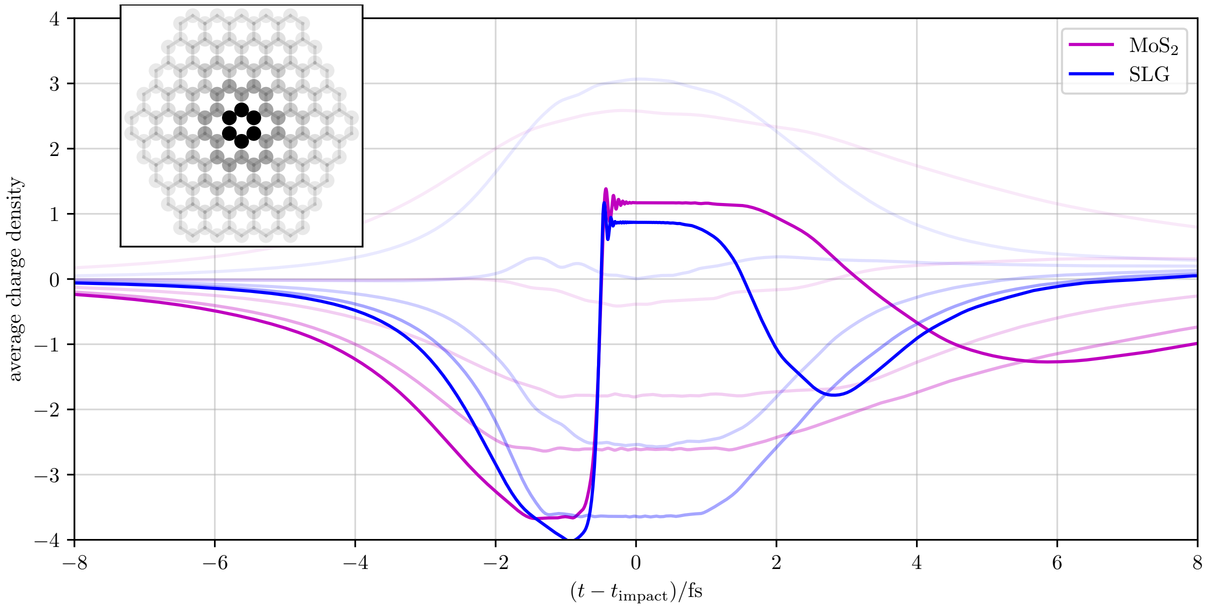

Figure 3.10: Average charge density profiles resolved for the different honeycomb rings during the interaction with the ion. Compared are the time series for $\mathrm{MoS_2}$ (purple solid lines) and SLG (red solid lines) in SOA approximation for a Xe^{+32} ion with a kinetic energy of $E_{\mathrm{ion}} = 113\,\mathrm{keV}$. The opacity of the lines indicates which ring of the cluster is represented, corresponding to the opacity of the atomic sites represented by black dots in the inset. The timescale has been shifted such that the ion passes through the plane of the cluster at 0 fs. Parameters for the simulation can be found in Tab. B.5.

In Fig. 3.10, we compare the charge density profiles for SOA calculations with SLG and MoS_2 and we find that the inclusion of correlations has a much greater effect in MoS_2 than in SLG (compare to Fig. 3.7). The reason for that is again the reduction of the doublon production rate due to the correlations. Since no high doublon production was observed in the SLG results, the inclusion of correlations has almost no effect on the dynamics.

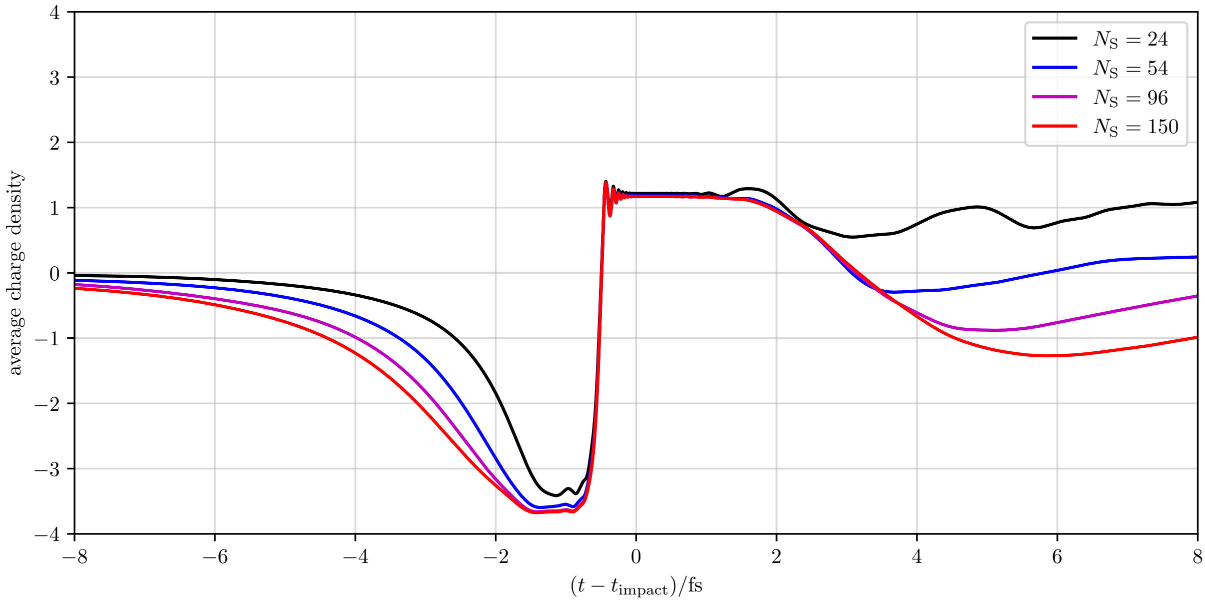

Figure 3.11: Average charge density profile on the central honeycomb ring during the interaction with the ion. Compared are the time series for MoS_2 in SOA approximation for different cluster sizes (see legends) for a Xe^{+32} ion with a kinetic energy of $E_{\mathrm{ion}} = 113\,\mathrm{keV}$. The timescale has been shifted such that the ion passes through the plane of the cluster at 0 fs. Parameters for the simulation can be found in Tab. B.6.

In Fig. 3.11, we compare the charge density dynamics on the central honeycomb ring in clusters of different sizes. We find that with increasing system size the initial charge up due to the positive ion potential is amplified. This is due to the increase in available charge carriers in the larger clusters which move towards the ion. In larger clusters this leads to an increased pressure on the electrons in the central ring, which are thereby incentivised to form double occupations. In a smaller cluster this pressure is not large enough so the Coulomb and Pauli repulsive forces on the central ring can hinder the accumulation of charge, up to a specific potential strength.

A similar effect can be reported after the interaction time with the ion, when the holes in the central ring are filled by the remaining electrons. This flow of electrons towards the center, amplified by the attractive ion potential is much larger in the larger system, since more electrons can participate. Therefore, an overcompensation effect emerges, in which the flowing electrons recharge the center in the larger systems. For the smallest system with $N_s = 25$, we find almost the opposite effect, because instead of the holes being filled by a charge density wave from the outer rings the charge density oscillates around the previous positive charge plateau. There are simply not enough electrons in the system to fill the holes in the center and outer rings completely, resulting in outward traveling charge density waves, which then reflect on the edges of the cluster and return to the center.

3.4 Secondary electron emission

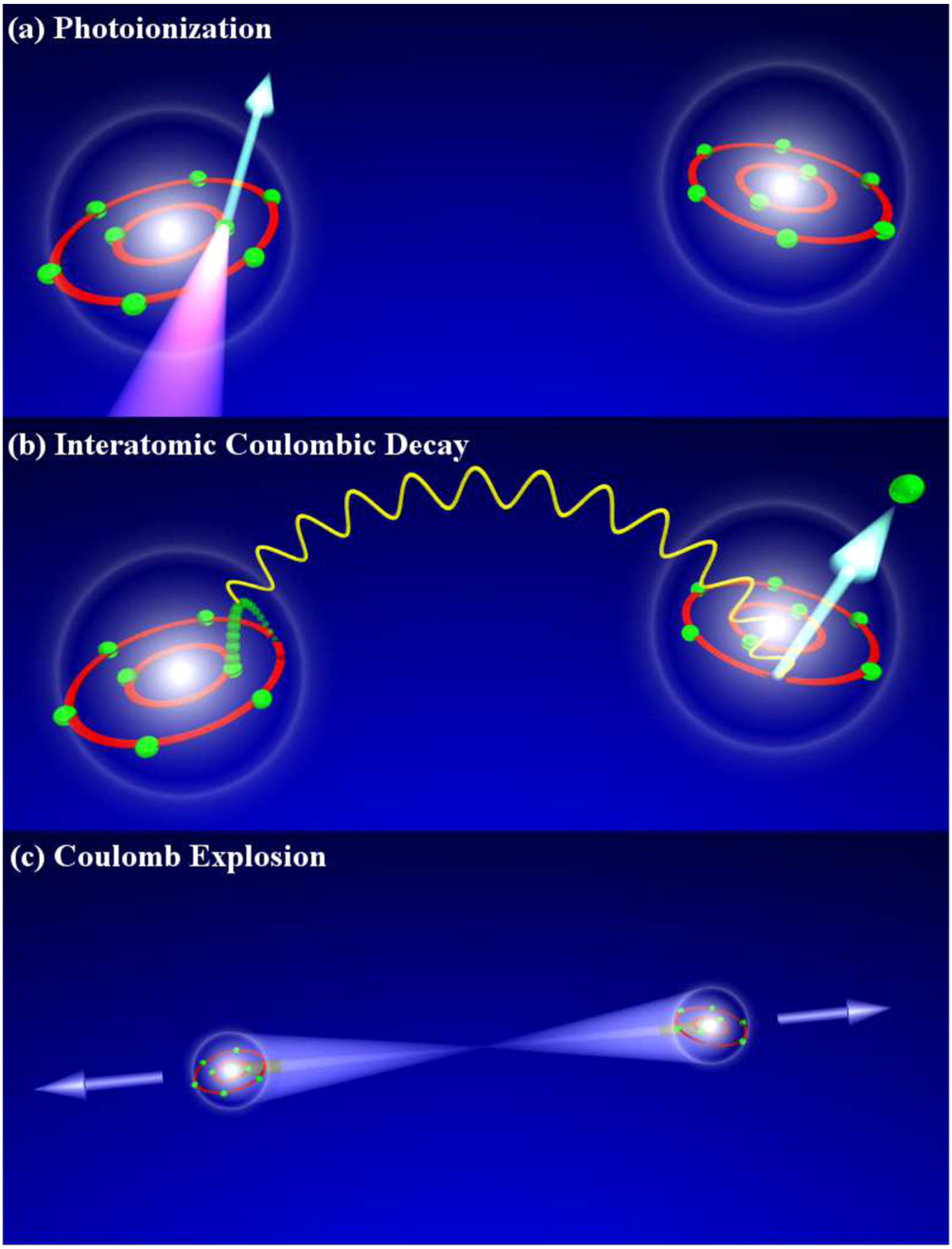

Figure 3.12: Schematic representation of the interatomic Coulomb decay in a dimer. Panel a) displays the initial emission of a core hole in one of the atoms via photoionization. This hole is then filled in b) and the excess energy is transferred to the second atom, resulting in the creation of a secondary electron. Panel c) shows the resulting Coulomb explosion, stemming from the now positively charged atoms. This repulsive force might result in local expansions of the cluster. The figure was taken from Ref. [42].

During the interaction between the ion and the cluster, the emission of secondary electrons can be observed. These free electrons are created by a process called interatomic Coulomb decay [43] (see

Ref. [44] for an extensive review). It stems from the transition of electrons in high-lying orbitals of the ion either due to core holes in the initial electronic structure of the ion or due to the capture of electrons by the outermost orbitals. When these electrons decay to lower orbitals, the excitation energy can be transferred to nearby atoms, such as the atoms of the innermost honeycomb ring. If the gain in kinetic energy is high enough, electrons of the cluster could be emitted into the surrounding vacuum from these central sites. A schematic visualization of the process can be found in Fig. 3.12. This process is similar to the conventional Auger decay, in which a high-lying electron decays and in the process excites a low lying electron in the same atom. This process is included in SOA, because all relevant states for this process are included in the basis.

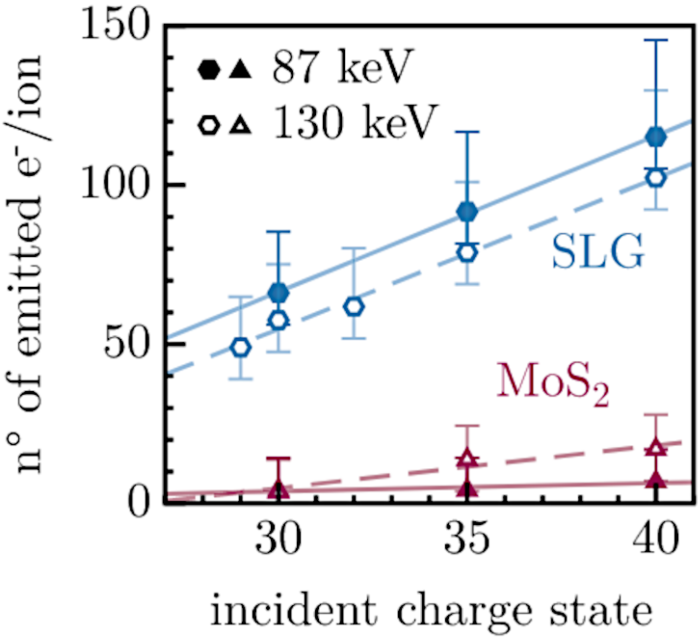

Figure 3.13: Measured number of emitted secondary electrons in ion stopping experiments with Xe ions of different incident charge states and two kinetic energies 87 keV and 130 keV for SLG (blue) and MoS_2 (red). Figure adapted from Ref. [16].

As can be inferred from the experimental results of Ref. [16] (see Fig. 3.13), the number of secondary electrons emitted differs drastically between the two targets. In particular, the emission rate is higher in SLG compared to MoS_2. In this work, we did not include the vacuum around the monolayer explicitly but instead tried to gauge the emission rate qualitatively from the charge density. An alternative might be to include a second set of environmental sites into which the electrons can also transfer.

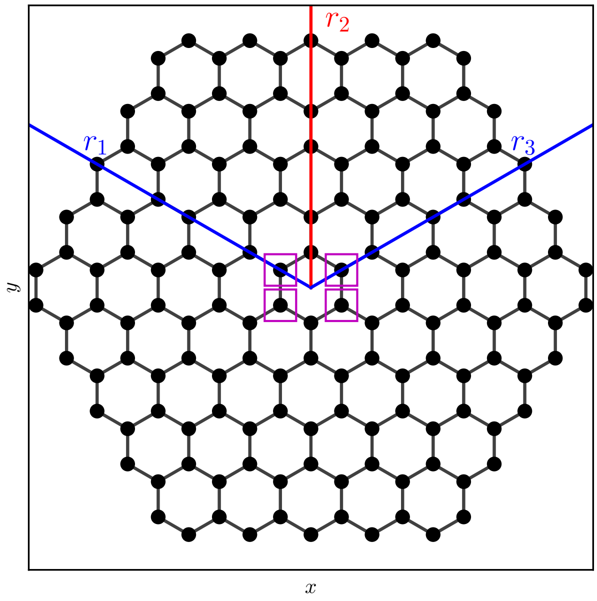

Figure 3.14: Visualization of the calculation of the electrostatic potential. The directions $\boldsymbol{r}_1$ and $\boldsymbol{r}_3$ (blue) correspond to paths including a coupled site, while $\boldsymbol{r}_2$ (red) corresponds to a path including a site that is not coupled to the ion. The potential is then averaged over all three directions.

To characterize the behavior of electrons which are emitted from the flake at a specific point in time, we compute the electrostatic potential from the electron density at that point in time and at a specific distance from the cluster. To remove the effect of the coupling scheme between the central honeycomb sites and the ion we average over different directions in the cluster as demonstrated in Fig. 3.14. We choose three directions $\boldsymbol{r}_1$, $\boldsymbol{r}_2$ and $\boldsymbol{r}_3$. Two of these include coupled sites in their path and the third includes a central site that is not coupled. Averaging the electrostatic potential

$$V(\boldsymbol{r}, t) = \frac{1}{4\pi\epsilon_0} \sum_i \frac{\Delta\rho_i(t)}{\boldsymbol{r} - \boldsymbol{r}_i}, \tag{3.2}$$

should therefore result in the correct potential an emitted electron would feel at that point in time regardless of the direction it is traveling in.

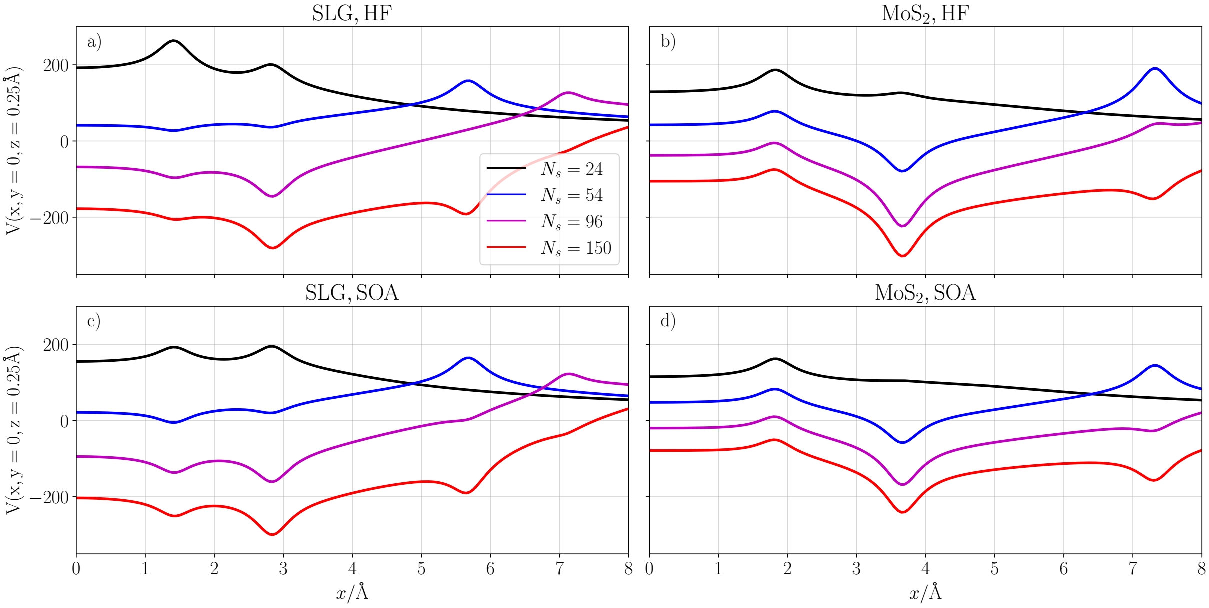

Figure 3.15: Electrostatic potentials for different simulations (SLG, MoS$_2$ and HF, SOA) and different system sizes (see legend). The potentials are calculated with Eq. (3.2) and the averaging scheme is displayed in Fig. 3.14.

Fig. 3.15 displays the results of the calculation for SLG in HF approximation [a)] and in SOA [c)], as well as for MoS$_2$ in HF approximation [b)] and in SOA [d)]. The potential is calculated at $t = 2\,\mathrm{fs}$ and $z = 0.25\,\text{Å}$. The first peak at around $x = 1.42\,\text{Å}$ for SLG and $x = 1.83\,\text{Å}$ corresponds to the potential at the central honeycomb ring. We find that the potential for SLG at the central honeycomb cluster has a local minimum for systems larger than $N_\mathrm{s} = 24$, while showing a maximum for $N_\mathrm{s} = 24$ in both HF and SOA approximations. The local minimum implies that an electron emitted at this time would be free to leave the cluster regardless of its energy, while the local maximum would act as a barrier. The potential barrier would result in a lower electron emission rate, since depending on their kinetic energy, electrons might be trapped by the potential.

For MoS$_2$, we find that regardless of the system size and approximation, the potential at the central honeycomb ring always has a local maximum. So regardless of the system size the electron emission rate will be diminished when compared to a similar SLG cluster, which is in accordance with the numerical and experimental findings in Ref. [16].

To explain these findings, we need to combine the previous observations. Because of the increased carrier mobility in SLG, the electrons can fill the positive charge density in the central honeycomb ring relatively fast, resulting in a neutral or negative charge at 2 fs. In contrast, the reduced carrier mobility in MoS$_2$ leads to a remnant positive charge at 2 fs. This positive charge of the cluster acts as an attractive force on the emitted electrons. The local maximum in the electrostatic potential for SLG and $N_\mathrm{s} = 24$ results from the lower number of carriers in the smaller system, which are not able to compensate the positive charge in the center.

In addition, we find that the inclusion of correlations does not significantly affect the behavior of the larger SLG cluster, while it has a visible effect on the electrostatic potentials calculated for MoS$_2$. Here, the intensity of the peaks is diminished, along with the strength of the potentials over the entire profile. This can be explained with the diminished doublon production due to the inclusion of correlations, which leads to a reduced charge density, especially in the center of the cluster where the differences are largest. Interestingly, for the $N_\mathrm{s} = 24$ SLG cluster, the correlations lead to a significant reduction of the central ring peak in the electrostatic potential. This could possibly be explained by the fact that the SOA correlations can compensate some of the positive charge in the center and on the edges, so that, even if the electron number is too low to fill all the holes, the positive charge density is lowered.

3.5 Spectral information

Before we can investigate the spectra of the different simulations, we first have to discuss how to obtain them. The main problem in time diagonal methods is that spectral information is lost when using HF-propagators for the retarded and advanced Green's function in Eq. (2.7) in order to achieve linear time scaling. In two-time approaches like NEGF theory, we have direct access to the spectra of our system. Since time and energy are conjugate variables in quantum mechanics, we can obtain the spectrum from a NEGF calculation by way of a Fourier transform with respect to the relative time. For example, the time resolved DOS can be calculated from [14]

$$\begin{aligned} A^{<}_{ij}(\omega, T) &= -i\hbar \int \mathrm{d}t\mathrm{d}t' \mathcal{S}(t-T)\mathcal{S}(t'-T)e^{-i\omega(t-t')}G^{<}_{ij}(t,t'), \\ A^{>}_{ij}(\omega, T) &= i\hbar \int \mathrm{d}t\mathrm{d}t' \mathcal{S}(t-T)\mathcal{S}(t'-T)e^{-i\omega(t-t')}G^{>}_{ij}(t,t'), \\ \mathrm{DOS}(\omega, T) &= \sum_i \Big(A^{>}_{ii}(\omega, T) + A^{<}_{ii}(\omega, T) \Big), \end{aligned}$$

where $\mathcal{S}$ is an artificial broadening, meant to resemble the spectral width of an experimental probe. However, since we do not have access to these two-time quantities, we have to approximate the spectrum using the time-diagonal quantities from the simulation.

One such method is given by Koopmans' theorem [31], which states that the ionization energies of a quantum mechanical system can be approximated by the eigenvalues of the single-particle Hamiltonian. The approximative nature of this approach becomes clear when considering the removal of an electron from a highly correlated system. In this case, the complete orbital structure of the system might be changed, resulting in a different spectrum.

However, keeping these potential pitfalls in mind, the Koopmans' theorem is optimal for our situation, since the single-particle HF Hamiltonian can be directly calculated from the one-particle density matrix. To do so we diagonalize the single-particle Hamiltonian

$$H^{\mathrm{ss},(1)}_{ij}(t) = \big(\epsilon - W_{ii}\big[\boldsymbol{S}(t)\big]\big)\delta_{i,i} - J\delta_{\langle i,j\rangle} + Un_{ii}(t)\delta_{i,i},$$

to obtain the eigenvalues $\{E_i\}$, as well as the corresponding eigenstates $|\phi_i\rangle$. The time dependent DOS is then given by

$$\mathrm{DOS}(E, t) = \sum_i \mathcal{S}(E - E_i), \quad \mathcal{S}(E) = \frac{1}{2\sigma^2} e^{-\frac{E^2}{\sigma^2}},$$

with a spectral width of $\sigma = 0.1J_0$. To calculate the ionization spectrum we also need the spectral weights

$$p_i(t) = \langle \phi_i | \,\hat{n}(t)\, | \phi_i \rangle,$$

which are the diagonal elements of the single-particle density matrix $\boldsymbol{n}$ in the eigenbasis of the single-particle Hamiltonian, giving the occupation of those states. The full spectrum is then given by

$$A^{<}(E, t) = \sum_i p_i(t)\mathcal{S}(E - E_i).$$

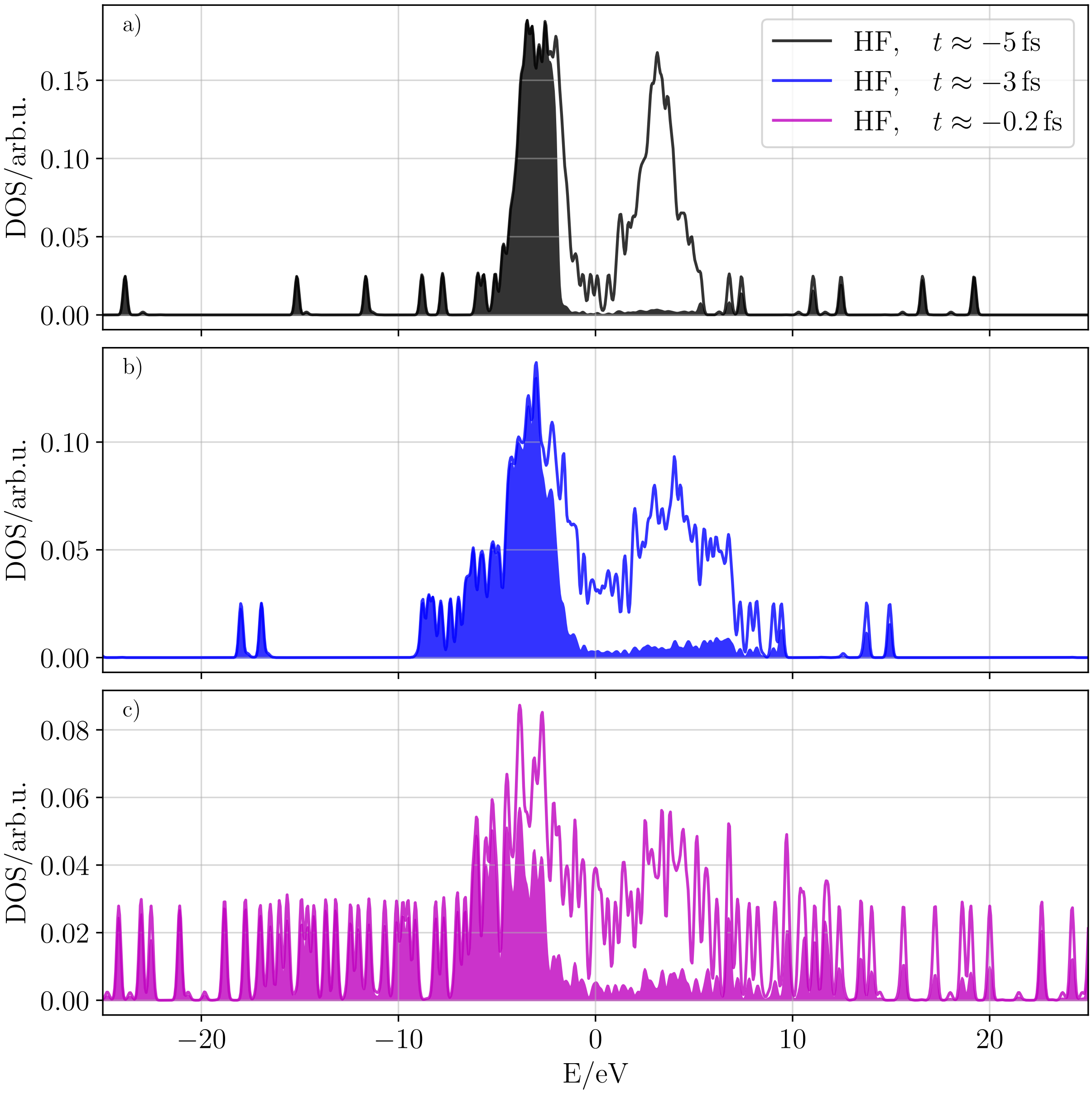

Figure 3.16: Time resolved DOS and occupation of the HF spectrum of MoS_2, at different times during the approach of the ion. All spectra were calculated under the assumption of Koopmans' theorem, from a HF simulation. The solid outline represents the density of states, while the filled regions represent the occupied states. The spectra were averaged over a small temporal window centered at the given times.

Fig. 3.16 shows the time resolved ionization spectra for MoS_2 in HF approximation at the times a) $t \approx -5\,\mathrm{fs}$, b) $t \approx -3\,\mathrm{fs}$ and c) $t \approx -0.2\,\mathrm{fs}$. Giving exact times for the spectra is not sensible, as the uncertainty relation between time and energy does not allow for a high time and energy resolution simultaneously. To compensate this effect, the spectra have been averaged across a small time window, centered at the given times, with a width of $0.1\,t_0$. Note that all three times lie before the ion impact, so that we can follow the effect of the approaching ion on the spectrum of the cluster. The solid outlines correspond to the density of states, while the filled region gives the occupancy of the corresponding states. In panel a), we see the system starting in almost the TB honeycomb DOS (compare to Fig. 3.2), with half of the states filled. Because the potential of the ion is already acting on the cluster, some electrons already start traveling towards the center, which explains the occupation of the high-lying states. In panel b), we see that the ion starts significantly warping the DOS of the system by broadening the honeycomb peaks. The portion of electrons in excited states also grows, again due to the accumulation in the center of the cluster. In panel c), 0.2 fs before the impact of the ion, the charge transfer has already started and the ion potential reaches a maximum. The combined influence on the DOS spreads it out across the whole energy range with some electrons occupying very high-lying states.

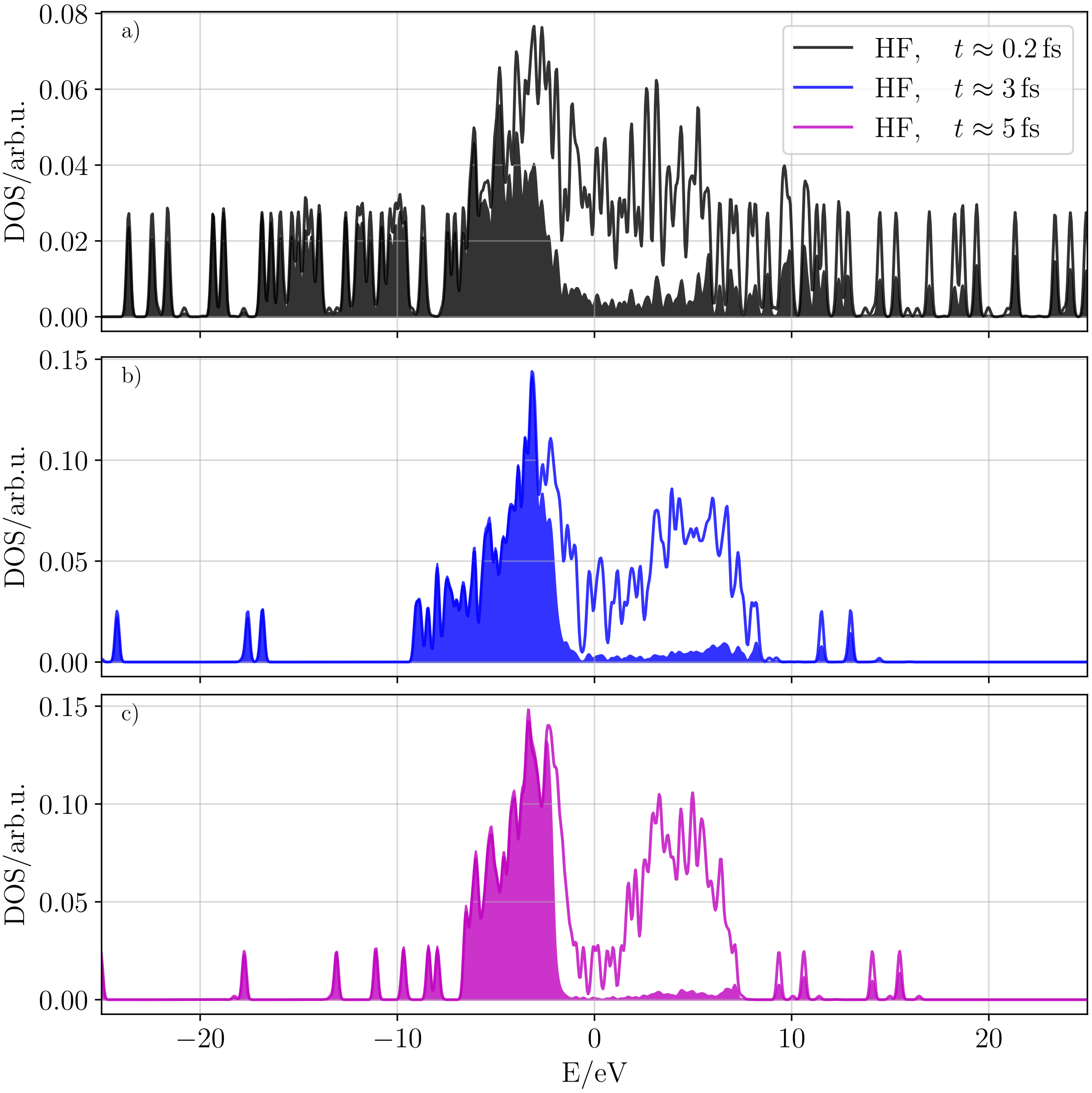

Figure 3.17: Time resolved DOS and occupation of the HF spectrum of MoS_2, at different times after the impact of the ion. All spectra were calculated under the assumption of Koopmans' theorem, from a HF simulation. The solid outline represents the density of states, while the filled regions represent the occupied states. The spectra were averaged over a small temporal window centered at the given times.

After the interaction with the ion, the DOS of the system relaxes back to the honeycomb DOS as shown in Fig. 3.17. In panel a), shortly after the ion impact, the spectrum is still highly disturbed by the ionic potential with highly excited electrons. However, shortly after, at around $t \approx 3\,\mathrm{fs}$ (panel b)), the DOS relaxes and now already resembles the DOS of the TB honeycomb lattice with the two main peaks visible. The asymmetry, especially regarding the width of the two peaks has increased due to the excitation. But most of the electrons reside again in the lower states. The main difference compared to before the impact of the ion seems to stem from the missing electrons in the system. Because of the reduced electron number, no static ground state of half filling can be reached, which leads to a distortion of the DOS due to the Hubbard repulsion. Also, it should be noted that at this point in time, the electron density oscillates, which is reflected in the fact that still high-lying states remain visibly occupied.

Long after the ion impact in panel c), the spectrum resembles that of Fig. 3.16, a) with a slightly increased occupation in the higher-lying states, which can again be attributed to the oscillations in the electron density. Also the right peak is broadened compared to the start.

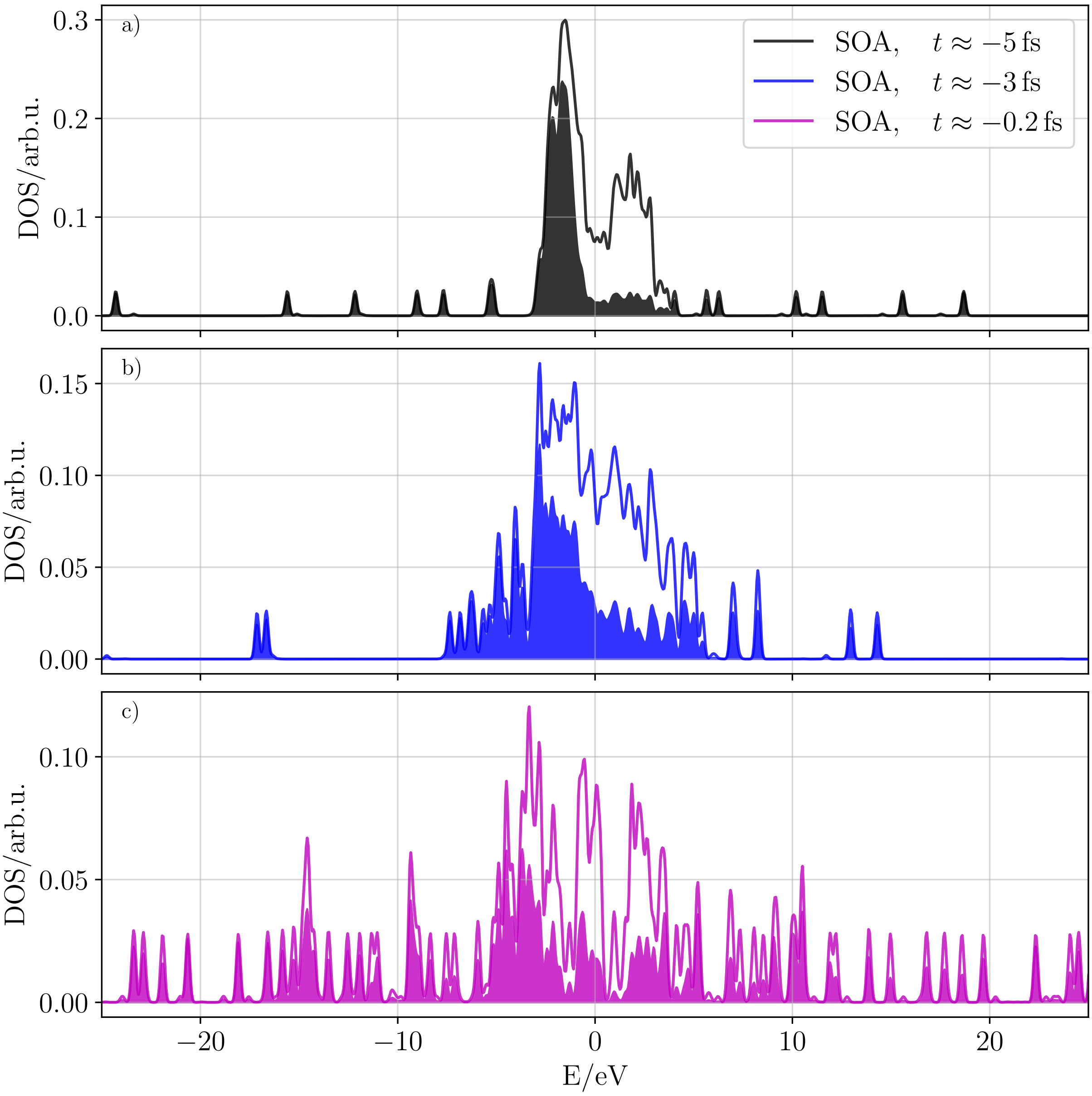

Figure 3.18: Time resolved DOS and occupation of the HF spectrum of MoS_2, at different times during the approach of the ion. All spectra were calculated under the assumption of Koopmans' theorem, from a SOA simulation. The solid outline represents the density of states, while the filled regions represent the occupied states. The spectra were averaged over a small temporal window centered at the given times.

By including correlations in the simulation of the ion impact, the evolution of the spectra changes significantly as shown in Fig. 3.18. First and foremost, the initial spectrum in panel a) is already broadened after the adiabatic switching routine, which results in a correlated groundstate. In addition to the broadening of the spectral peaks, the right peak is also substatially reduced in intensity compared to the left peak. The electrons in the system already reside in higher lying shells. This could be explained by the fact that in all practical adiabatic switching routines, the resulting state is not guaranteed to be the groundstate of the system but can oscillate due to excited electrons. Also the potential of the ion, which pulls the electrons towards the center of the cluster, already results in additional correlations. Since the Koopmans' theorem neglects these correlational effects, the spectrum might include systematic errors in the form of deviations from the groundstate.
In panel b), the ion is close to the cluster and the strong external potential broadens the peaks signifi-

cantly so that they visibly merge into a single peak in the center of the spectrum.
Close to the point of impact, the spectrum in panel c) no longer resembles the honeycomb DOS. However, the interpretation of this result is highly speculative, since the system is far from equilibrium and the effect of correlations is difficult to gauge accurately.

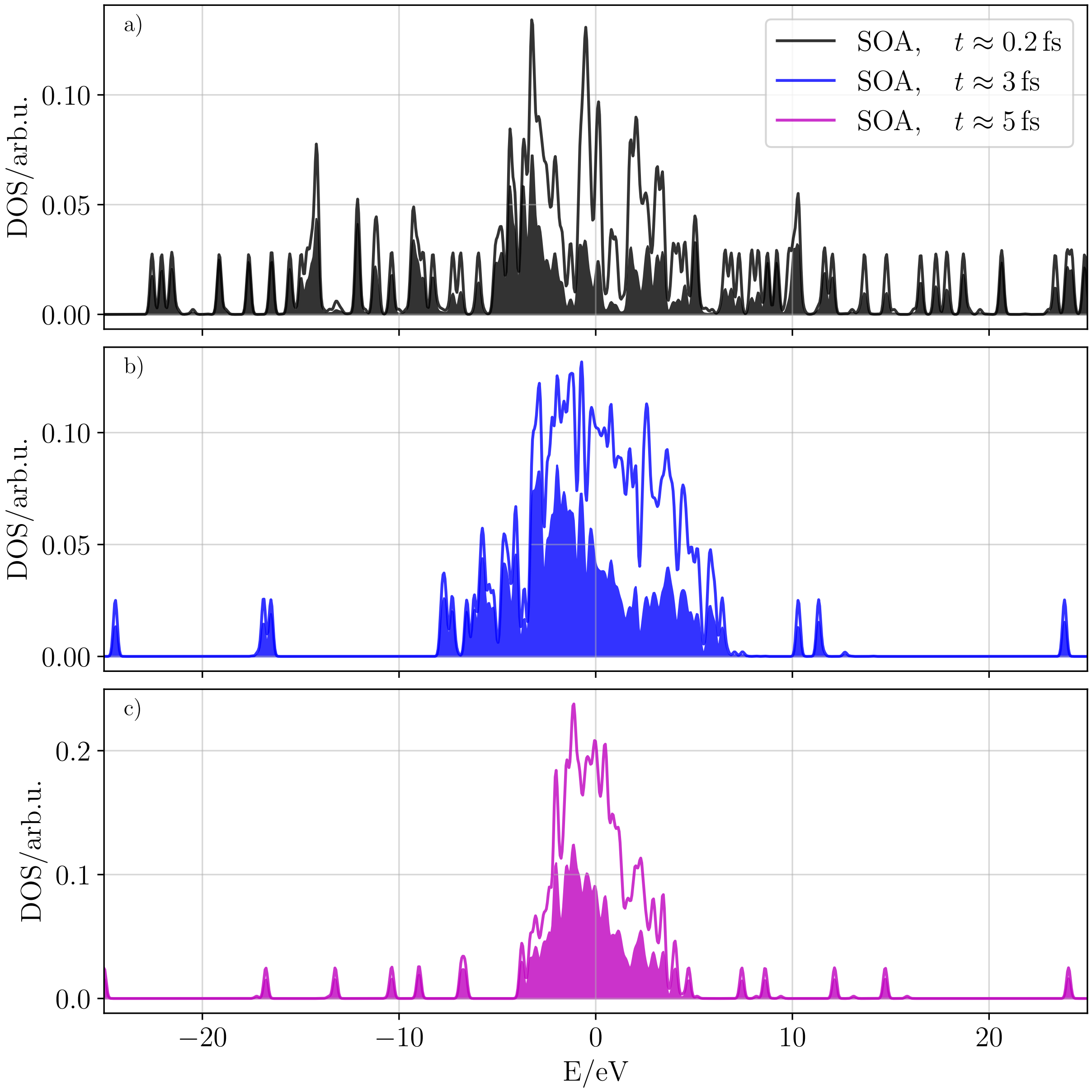

Figure 3.19: Time resolved DOS and occupation of the HF spectrum of MoS_2, at different times after the impact of the ion. All spectra were calculated under the assumption of Koopmans' theorem, from a SOA simulation. The solid outline represents the density of states, while the filled regions represent the occupied states. The spectra were averaged over a small temporal window centered at the given times.

After the ion has impacted the honeycomb cluster in the SOA simulation, the resulting spectra in Fig. 3.19 differ significantly from those of the HF simulation in Fig. 3.17. Instead of relaxing towards the TB DOS, the two peaks stay as one. Shortly after the ion impact in panel a), the spectrum is still strongly broadened by the potential of the ion and far from equilibrium. However, at later times in panel b), the new DOS looks very different from the TB DOS. The two peaks can not be distinguished anymore and instead form a central peak in the spectrum, which is roughly at half occupation with a few high lying states occupied.
This form of the spectrum becomes even more apparent at the latest time in panel c), where the system seems to have equilibrated. Instead of a fully occupied lower peak, which would correspond to the valence

band of the system and an almost empty conduction band, we find just a single band in the center of the spectrum at half occupation, with the electrons distributed corresponding to the intensity of the spectral peaks. This, in turn, could be interpreted as the system being conductive, since almost all electrons are free to move between states and can therefore contribute to currents across the system.

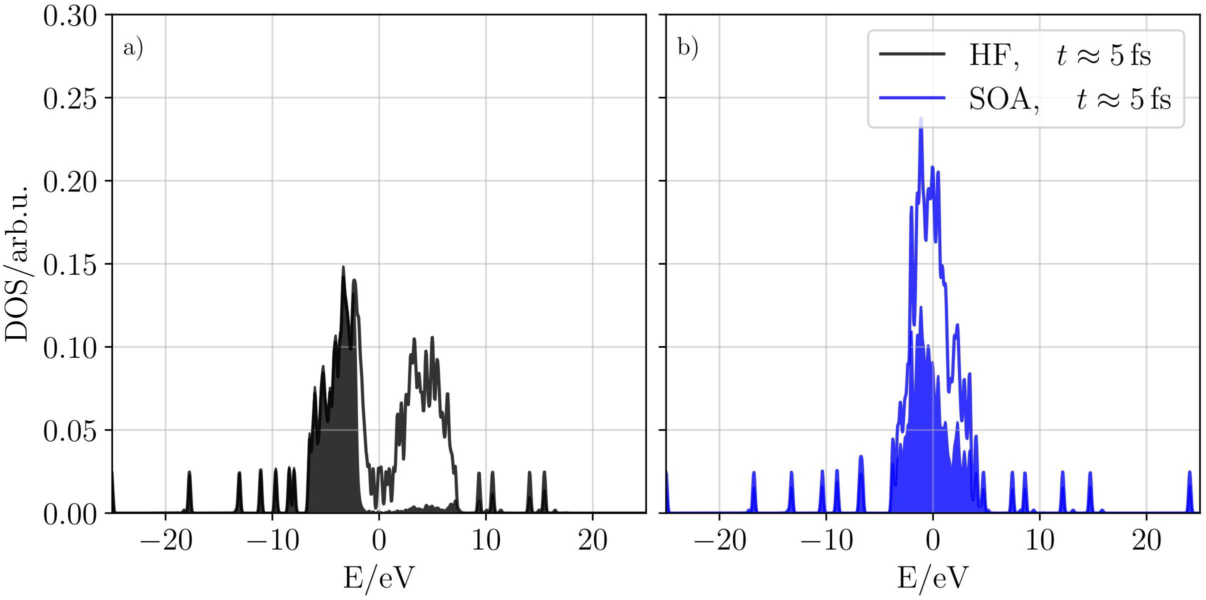

Figure 3.20: Time resolved DOS and occupation of the HF spectrum of MoS_2, at the end of the simulation, long after the ion impact. Compared are the final states of the system in the HF [a)] and SOA [b)] simulations.

We find that the inclusion of correlations in the system results in a significant alteration of the material properties by the ion impact, as clearly shown in Fig. 3.20. In this figure we compare the final states of the system in HF and SOA to emphasize the difference between the two results. It is apparent that the SOA result in panel b) does not match the expected spectrum of a semiconductor, while the HF result can clearly be split into conduction and valence band. The inclusion of correlations and the loss of particles resulted in the formation of a single, half-filled band, reminiscent of a conductor. This change of the spectrum can be partly attributed to the broadening of the two initial peaks, which is commonly know effect due to correlations. The two peaks become so broad, that they in fact overlap to form the single peak.

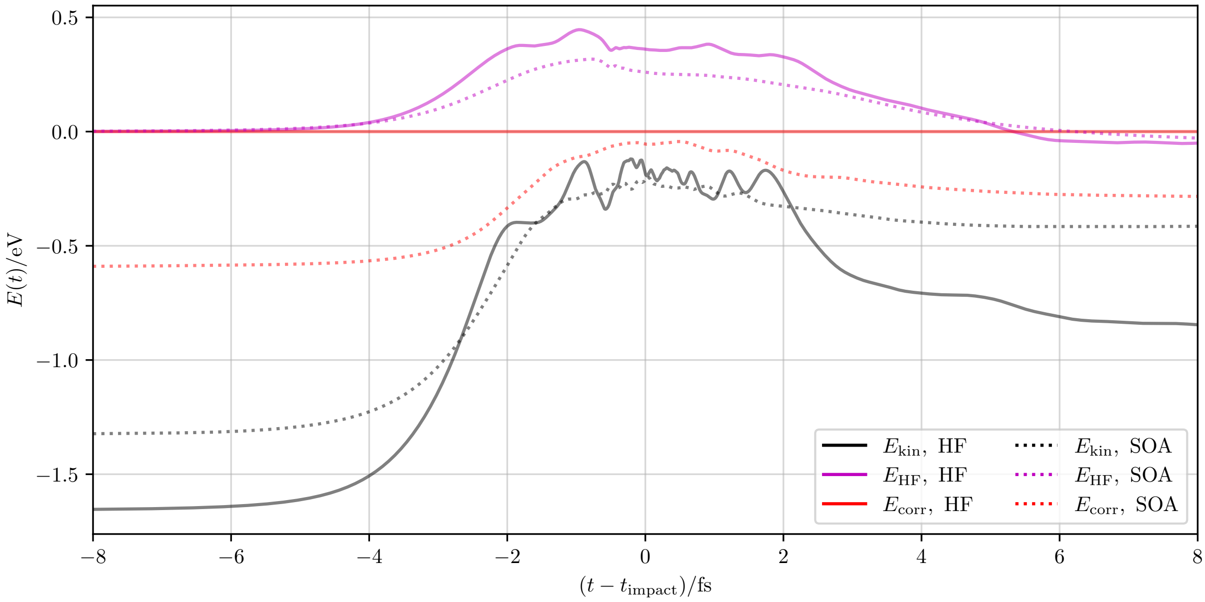

Figure 3.21: Different energy profiles over the course of the simulation of a $N_\mathrm{s} = 150$ $\mathrm{MoS_2}$ cluster, interacting with a Xe^{+32} ion with a kinetic energy of $E_{\mathrm{ion}} = 113\,\mathrm{keV}$. Solid lines represent the results of a HF simulation while dotted lines represent the results of a SOA simulation. The different energy forms are kinetic energy E_{kin} (black), HF energy E_{HF} (purple) and correlation energy E_{corr} (blue).

To explain this finding, we examine the different energy profiles over the course of the simulation in Fig. 3.21. There we find the kinetic, HF and correlation energies at various times compared between a HF and SOA simulation for $N_\mathrm{s} = 150$. The correlation energy, which of course stays constant at 0 in the HF simulation is increased significantly in the SOA simulation when compared between the initial state before the impact of the ion and the later state after the ion has passed the cluster. After the interaction with the ion, we observe that the correlation energy is higher than before because of a change in the electron correlations due to the interaction with the ion. Also, the kinetic energy is higher compared to the HF simulation, since again the doublon occupation is diminished due to the correlations in the system.

4 Multiband models

In this chapter, we are going to show how a more complex model of the bandstructure in MoS_2, namely the 3-band model [45], can be used to describe the MoS_2 monolayer in the ion stopping simulation. The goal of this chapter is to investigate whether such a model can improve the numerical predictions of the method. The potential upside of the 3-band model is that it accurately describes the band structure around the band-gap of MoS_2 monolayers without the need for an interaction term.

4.1 Introduction

In Ch. 3, we have seen that even a very simple, effective one-band model can be used to describe the electron dynamics in MoS_2 monolayers effectively. However, the actual band structure of MoS_2 is more closely matched with an eleven band model. To understand why, we can examine the orbitals of the Molybdenum and Sulfur atoms separately, to get an idea of how many distinct energy bands the compound could possibly form. The electron configuration of Mo is given by [Kr]$4d^5 5s^1$, which is often simplified to [Kr]$4d^5$ in the literature. This means that in total there are five possible electron d-orbitals per spin component. Sulfur is described by [Ne]$3s^2 3p^4$, which indicates that there are already three outermost p-orbitals per spin component. Therefore, for each unit cell consisting of S-Mo-S, there are a total of eleven orbitals per spin component, meaning that under the assumption of spin symmetry, the band structure will consist of up to eleven bands. Such an eleven-band, tight-binding model has been developed and fitted to density functional theory results [46] and was shown to accurately reproduce the electronic structure of MoS_2 mono- and multilayers. However, for the purpose of simulations in the framework of the G1–G2 scheme, such a model is not suitable as it would introduce a factor of eleven in the number of basis sites and therefore reduce the possible number of lattice sites that can be efficiently simulated even further. More suitable descriptions of the material can be obtained by focusing on the Mo d-orbitals, since these contribute mainly to the DOS near the band gap [47]. Nevertheless, only describing MoS_2 in terms of one atomic species will introduce systematic errors, since the presence of S atoms in the crystal is not taken into account.

In order to include the symmetry breaking effects of Sulfur the atoms, the authors of Ref. [48] included virtual s-orbitals in the model to effectively model the presence of the Sulfur s-orbitals. The resulting seven-band tight binding model can then be downfolded to obtain a five-band model which encodes the Sulfur orbitals in its parameters.

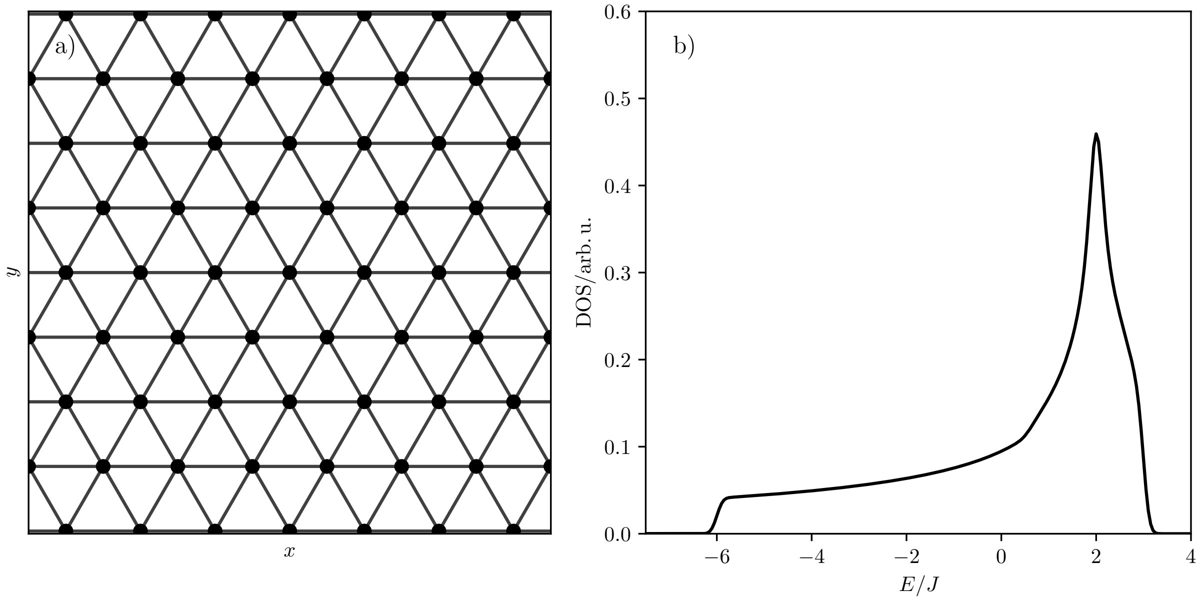

Figure 4.1: TB density of states of the infinite triagonal lattice. Panel a) displays the spatial lattice structure with the lattice sites as black dots and the nearest neighbor connections as solid, black lines. Panel b) shows the resulting DOS calculated from the TB Hamiltonian. The energy is given in units of the hopping amplitude J.

An even more condensed model that we will discuss in this section was presented in Ref. [45], where the authors focused on the three d-orbitals of Molybdenum d_{z^2}, d_{xy} and $\mathrm{d}_{x^2-y^2}$. Since this model is restricted to the Mo atoms of the lattice, the geometry is now given by a triagonal lattice, which is displayed in Fig. 4.1, a). Panel b) displays the DOS of a single-band TB model on an infinite triagonal lattice. Comparing the DOS to the one of the honeycomb lattice in Fig. 3.1, we can see that instead of the two peaks around $E = 0$, we get only a single, asymmetric peak, which is not suitable to describe a semiconductor like MoS_2.

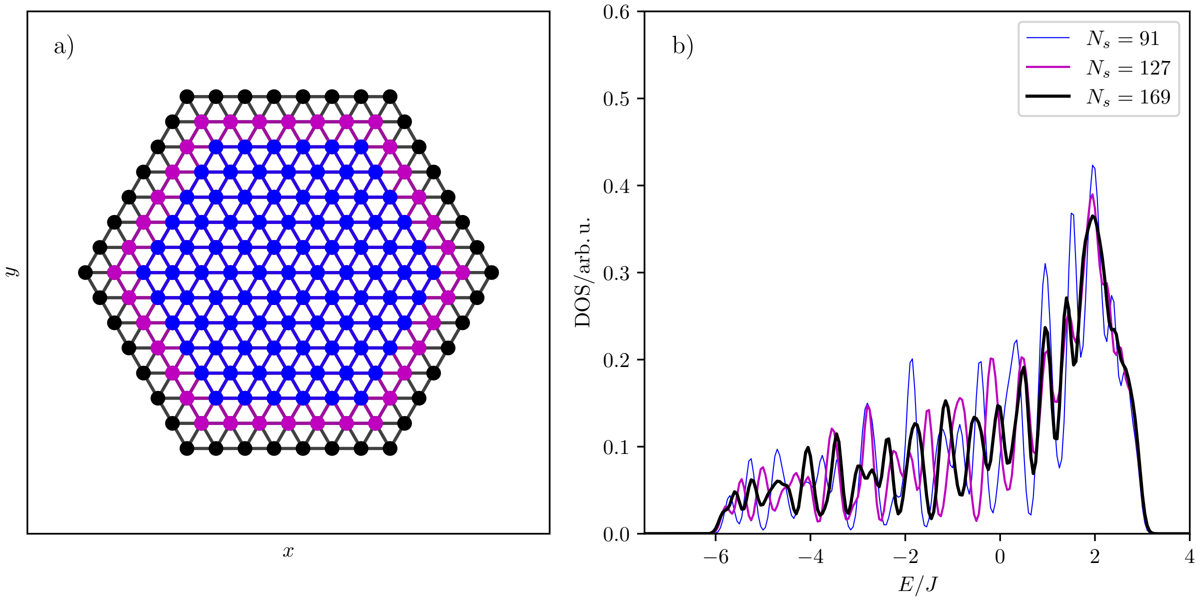

Figure 4.2: TB density of states for finite triagonal clusters. Panel a) displays the spatial lattice structures for three flake sizes. Panel b) displays the DOS corresponding to the TB Hamiltonian solved for the different flake sizes. The energy is given in units of the hopping amplitude J.

Also, when transitioning to finite clusters, which we considered in the previous chapter to model the MoS_2 monolayers used in the ion stopping experiments, we find that while the DOS converges with increasing system size towards the DOS of the infinite lattice in Fig. 4.2, b), the DOS for a considerable large system remains very noisy and dominated by the effects of edgestates.

To better model MoS_2, we will describe in detail in the following section (Sec. 4.2) the strategy the authors of Ref. [45] used to obtain the so-called 3-band TB model for MoS_2 monolayers.

4.2 The 3-band model

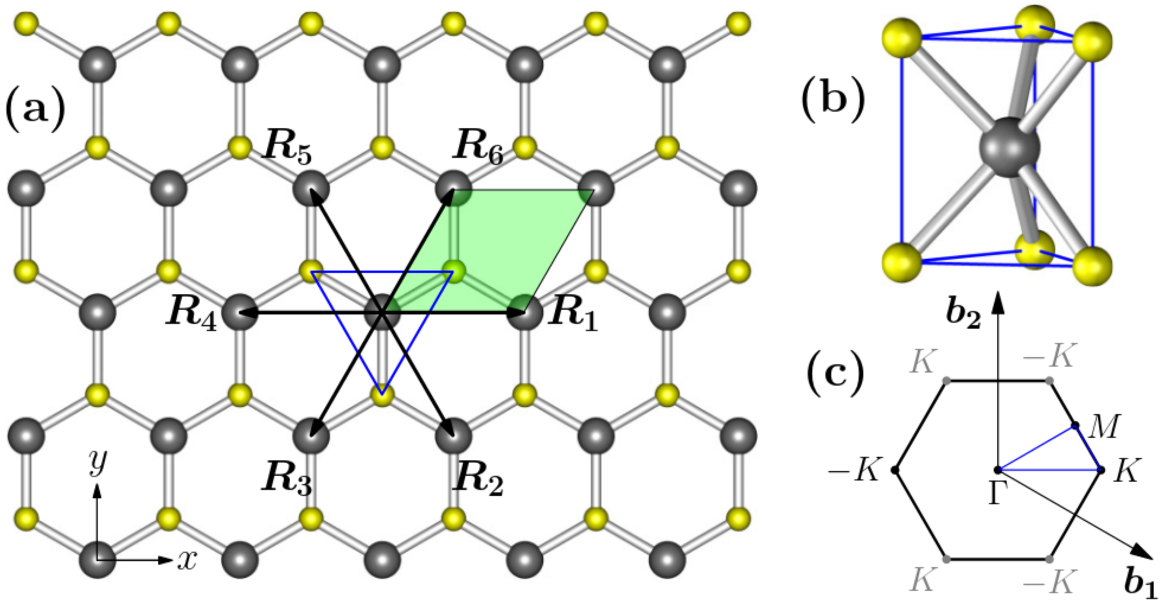

Figure 4.3: Visualization of the lattice geometry of a MoS_2 monolayer. Panel a) shows the spatial lattice structure in a top down view along the z-axis, with yellow dots representing the Sulfur atoms, while gray dots represent the Molybdenum atoms. The white lines represent the nearest neighbor connections. The black arrows give the six lattice vectors along which the lattice can be translated. The green area represents the unit cell and the blue triangle is the triagonal prismatic coordination also displayed in panel b) in the side view. Panel c) shows the first Brillouin zone. The diagram was taken from Ref. [45].

The full symmetries of the MoS_2 crystal structure are given by the D_{3h} point-group, which includes the two rotations around the z-axis $\{\hat{C}_3, \hat{C}_3^2\}$ with degrees of $2\pi/3$ and $4\pi/3$ respectively, as well as the vertical mirrors $\{\hat{\sigma}_v, \hat{\sigma}'_v, \hat{\sigma}''_v\}$, where $\hat{\sigma}_v$ is the plane perpendicular to the xy-plane at the angular bisector of $\boldsymbol{R}_1$ and $\boldsymbol{R}_2$ in Fig. 4.3. The other two mirrors are then $\hat{\sigma}_v$ rotated by $2\pi/3$ and $4\pi/3$.
If we limit the description to the three most dominant Mo d-orbitals near the band gap, namely the d_{z^2}, d_{xy} and $\mathrm{d}_{x^2-y^2}$, we obtain a triangular lattice of Mo atoms like the one shown in Fig. 4.1. However, since the orbitals are still shaped by the presence of the Sulfur atoms in the actual lattice, instead of the triangular symmetries, they transform according to the D_{3h} point-group of the full system. These transformations group the three orbitals into two classes, namely $\mathrm{A}'_1 = \{\mathrm{d}_{z^2}\}$ and $\mathrm{E}' = \{\mathrm{d}_{xy}, \mathrm{d}_{x^2-y^2}\}$. This is because the d_{z^2} points perpendicular to the xy-plane and is rotation symmetric with respect to rotations around the z-axis. Therefore, it only transforms into itself, when the lattice is rotated with the $\hat{C}_3$ operation and mirrored with the vertical mirror $\hat{\sigma}'$. The other two orbitals in contrast have only discrete symmetries with respect to rotations around the z-axis, meaning that they transform into linear combinations of each other with the different symmetry operations.
With this classification in place we can write the basis of the system in the following way

$$|\phi_1^1\rangle = \mathrm{d}_{z^2}, \quad |\phi_1^2\rangle = \mathrm{d}_{xy}, \quad |\phi_2^2\rangle = \mathrm{d}_{x^2-y^2},$$

where the superscripts refer to the symmetry class, while the subscripts refer to the basis element. The hopping integrals in the basis are then given by

$$E^{\mathrm{jj}'}_{\mu\mu'}(\boldsymbol{R}_i) = \langle \phi^{\mathrm{j}}_{\mu}(\boldsymbol{r})| \hat{H} |\phi^{\mathrm{j}}_{\mu'}(\boldsymbol{r}-\boldsymbol{R}_i)\rangle . \tag{4.1}$$

Using the matrix representations of the relevant symmetry operations $D^{\mathrm{j}}(\hat{g})$ with the symmetry operations $\hat{g} = \{\hat{E}, \hat{C}_3, \hat{C}_3^2, \hat{\sigma}_v, \hat{\sigma}'_v, \hat{\sigma}''_v\}$,[1] all integrals between the lattice sites separated by the translation vectors

---

[1] $\hat{E}$ is the identity operation

$\{\boldsymbol{R}_i\}$ (see Fig. 4.3) can be obtained from

$$E^{\mathrm{jj}'}_{\mu\mu'}(\hat{g}\boldsymbol{R}_1) = \left[D^{\mathrm{j}}(\hat{g})E^{\mathrm{jj}'}(\boldsymbol{R}_1)\left[D^{\mathrm{j}'}(\hat{g})\right]^{\dagger}\right]_{\mu\mu'}. \tag{4.2}$$

Eq. (4.2) follows from Eq. (4.1), by applying the necessary symmetry transformations to the orbitals to reflect the transformation of the coordinate system.

The authors then go on to calculate from the above expressions the TB Hamiltonian in momentum representation and solve for the band structure by diagonalizing the result. The resulting dispersion relations are then fitted to the band structure results from their own density functional theory (DFT) calculations in both generalized-gradient approximation (GGA) and local-density approximation (LDA). By fitting the dispersion relations to the band structure at the high-symmetry $\boldsymbol{k}$ points they obtained values for the eight independent parameters

$$\begin{gathered}\epsilon_1, \quad \epsilon_2, \quad t_0 = E^{11}_{11}(\boldsymbol{R}_1), \quad t_1 = E^{12}_{11}(\boldsymbol{R}_1), \quad t_2 = E^{12}_{12}(\boldsymbol{R}_1), \\ t_{11} = E^{22}_{11}(\boldsymbol{R}_1), \quad t_{12} = E^{22}_{12}(\boldsymbol{R}_1), \quad t_{22} = E^{22}_{22}(\boldsymbol{R}_1).\end{gathered}$$

Here ϵ_i are the two on-site energies in the two different symmetry classes, while the other parameters are the hopping amplitudes in and between the three bands for the nearest neighbors separated by $\boldsymbol{R}_1$. Since we want to perform our simulations in the spatial instead of the momentum basis we can use Eq. (4.2) to obtain the remaining hopping parameters for the other translation vectors.

However, since the authors reported an even more accurate reproduction of the DFT band structure over the full first Brillouin zone rather than just the high symmetry points in their extended tight-binding model, which includes electron hopping between up to third nearest neighbors on the lattice, we are going to use these results for our TB model. This extension of the model introduces more hopping parameters for the second- and third-nearest neighbors

$$\begin{gathered}r_0 = E^{11}_{11}(\tilde{\boldsymbol{R}}_1), \quad r_1 = E^{12}_{11}(\tilde{\boldsymbol{R}}_1), \quad r_2 = E^{12}_{12}(\tilde{\boldsymbol{R}}_1), \\ r_{11} = E^{22}_{11}(\tilde{\boldsymbol{R}}_1), \quad r_{12} = E^{22}_{12}(\tilde{\boldsymbol{R}}_1), \quad r_{22} = E^{22}_{22}(\tilde{\boldsymbol{R}}_1),\end{gathered}$$

with the second-nearest neighbor translation vectors $\tilde{\boldsymbol{R}}_1 = \boldsymbol{R}_1 + \boldsymbol{R}_2$ and

$$\begin{gathered}u_0 = E^{11}_{11}(2\boldsymbol{R}_1), \quad u_1 = E^{12}_{11}(2\boldsymbol{R}_1), \quad u_2 = E^{12}_{12}(2\boldsymbol{R}_1), \\ u_{11} = E^{22}_{11}(2\boldsymbol{R}_1), \quad u_{12} = E^{22}_{12}(2\boldsymbol{R}_1), \quad u_{22} = E^{22}_{22}(2\boldsymbol{R}_1),\end{gathered}$$

with the third-nearest neighbor translation $2\boldsymbol{R}_1$. The results of the fits for all parameters can be found in Tab. 4.1.[2]

ϵ_1	ϵ_2	t_0	t_1	t_2	t_{11}	t_{12}	t_{22}
0.683	1.707	-0.146	-0.114	0.506	0.085	0.162	0.073
		r_0	r_1	r_2	r_{11}	r_{12}	r_{22}
		0.060	-0.236	0.067	0.016	0.087	0
		u_0	u_1	u_2	u_{11}	u_{12}	u_{22}
		-0.038	0.046	0.001	0.266	-0.176	-0.150

Table 4.1: Fitting results for the 3-band model with up to third-nearest neighbor hopping, obtained from fits to a GGA DFT calculation. Values are in units of eV. The parameters have been taken from Ref. [45].

---

[2] It should be noted that the authors repeated this same procedure for a number of TMDCs, so that the model can be used for different materials as well.

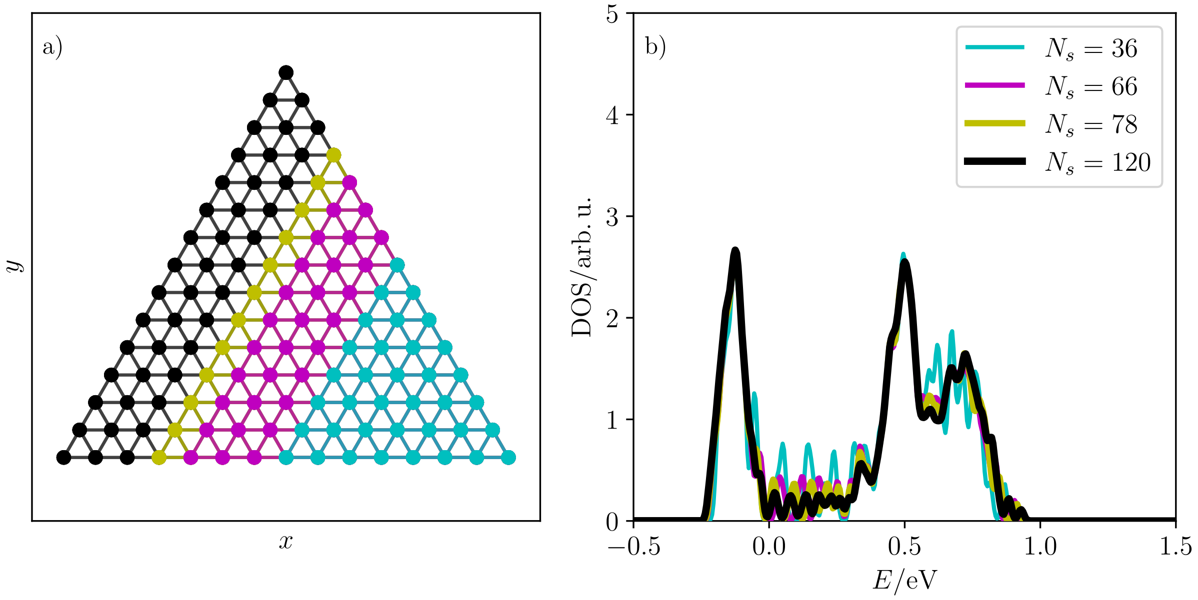

Figure 4.4: Density of states for the three band model for increasing cluster sizes. The clusters are shown in panel a) while the corresponding, color mapped DOS results are shown in panel b).

In Fig. 4.4, b) the DOS is displayed for the different cluster sizes in panel a). We find that with an increase of the system size and the subsequent decrease of the influence of the edgestates in the DOS, the 3-band picture emerges. The first peak below the band gap corresponds to the d_{z^2} orbitals which have a lower on-site energy (compare Tab. 4.1) while the two peaks above the band gap correspond to the two higher energy orbitals d_{xy} and $\mathrm{d}_{x^2-y^2}$. The bandgap of MoS_2 which is around 1.8 eV [33] can also be approached by this model, by increasing the system size.

4.3 Ion stopping with charge transfer in the 3-band-model

In order to apply the 3-band model in the ion stopping simulations, we use the parameters from Tab. 4.1, to compute the TB Hamiltonian. This Hamiltonian now not only includes the three different bands and the new interband hopping terms, but also direction dependent hopping amplitudes stemming from the symmetry transformations of the orbitals. The Hamiltonian can therefore be written as

$$\hat{H} = \sum_{\alpha,i,\sigma} \epsilon_\alpha \hat{c}_{i,\alpha,\sigma} \hat{c}^\dagger_{i,\alpha,\sigma} + \sum_{\alpha,\beta,\langle i,j\rangle^{(3)},\sigma} t^{\alpha\beta}_{ij}(\boldsymbol{r}_i - \boldsymbol{r}_j) \hat{c}_{i,\alpha,\sigma} \hat{c}^\dagger_{j,\beta,\sigma},$$

with the new indices α and β referring to the three different bands. The nearest neighbor sum is now replaced by a sum over all up to third-nearest neighbors $\langle i,j\rangle^{(3)}$. In this Hamiltonian we did not include an explicit interaction term between the electrons. This is because the use of such a contribution is usually to reproduce the band gap in the system. However, since this model has been optimized to reproduce the full band structure from DFT calculations, which themselves already reproduce the correct band gap, a simple Hubbard interaction will not be sufficient. In fact, trying to expand the 3-band model with a simple Hubbard model did not improve the resulting DOS.[3]

We also needed to use triagonal supercells, like the ones displayed in Fig. 4.2, because hexagonal supercells, such as the one in Fig. 4.1 have an odd number of lattice sites, which makes it impossible to start in a spin-symmetric state of half filling. However, for specific sizes of triagonal clusters the number of lattice sites is even and therefore this initial state can be realized.

To couple the ion to the cluster, the same model for the ion and the charge transfer, which was presented in Ch. 3, was used, except for the charge transfer delta function. In the 3-band model we assumed six available electrons per site, so that in order for the ion to be completely neutralized in principle it would

---

[3] It should be noted that only a simplified model in which in each of the bands the same interaction strength is assumed was tried, in order to keep the number of free parameters in the model low.

need a charge that is a multiple of 6. Nevertheless, we chose a Xe^{+32} and coupled all three of the central sites to the ion, which again travels in a straight line with a constant velocity through the center of the cluster, perpendicular to the xy-plane.

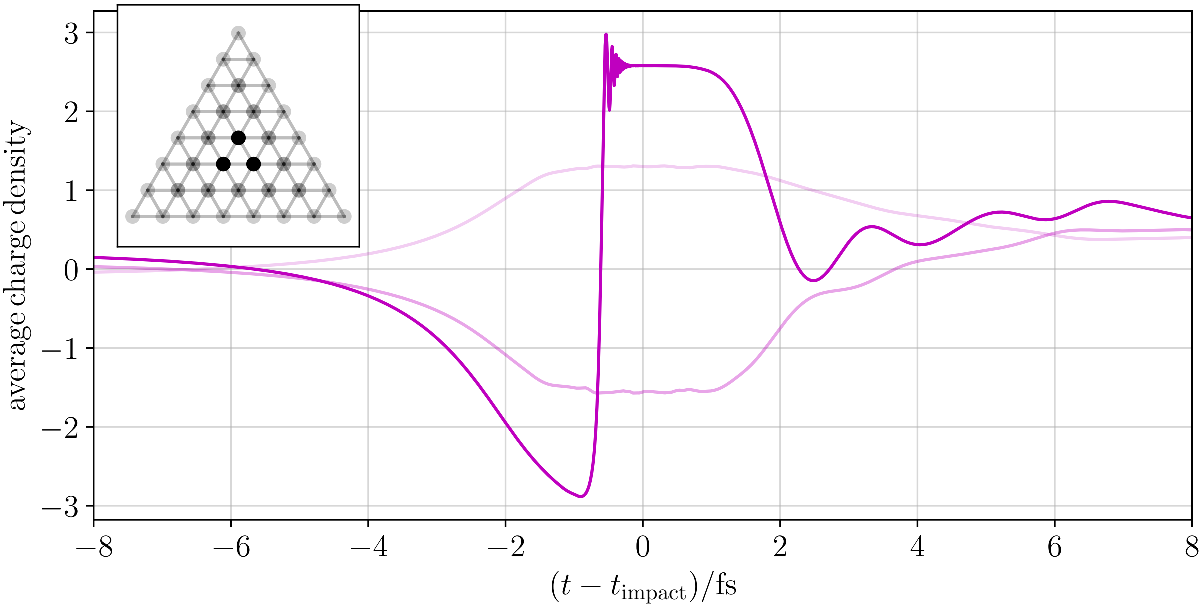

Figure 4.5: Average charge density profiles resolved for the different triangles in the 3-band model during the interaction with the ion. Plotted is the time series for the 3-band model in TB approximation for a Xe^{+32} ion with a kinetic energy of $E_{\text{ion}} = 113\,\text{keV}$. The α value of the lines indicates which triangle of the cluster is represented, corresponding to the α values of the atomic sites represented by black dots in the inset. The timescale has been shifted so that the ion passes through the plane of the cluster at 0 fs.

Fig. 4.5 displays the results of this simulation. Similar to the honeycomb models before, the attractive potential of the ions, creates a positive charge up in the center of the cluster, while the outermost ring accumulates a positive charge, due to the reduction of the charge carriers. Then, once the ion passes the point of resonant charge transfer, the ion exchanges charge carriers with the cluster, leading to an immediate positive charge up of the coupled sites. After a short period of constant positive charge in the center during which the ion and the cluster interact, the remaining electrons fill the holes in the center of the cluster. We find that the dynamics on the central ring resemble more those of the SLG honeycomb model, implying that the carrier mobility in this model is higher than in the honeycomb MoS$_2$ model. This can be explained by the absence of the Hubbard interaction term in the Hamiltonian, since in the HF approximation, the repulsive force can lead to a stabilizing effect on the doublon occupation. Because this model does not include an interaction term, this effect is absent. This also implies that this model can not include correlations, even in higher order approximations such as SOA. Therefore, if this model should prove to be more accurate than the honeycomb model, it would greatly reduce the numerical costs of simulating MoS$_2$ monolayers. However, since the TB-parameters only capture the groundstate-correlations, the accuracy for a system far from equilibrium, will not be high.

5 Summary and Discussion

We started this work by deriving the equations of motion of the dynamically screened ladder approximation in the framework of reduced density matrices. Then we presented the findings of Ref. [11] in which the equivalence between the reduced density matrix method and the recently developed G1–G2 scheme was established. The G1–G2 scheme is derived as the time-diagonal case from non-equilibrium Green function theory which is used to compute the dynamics of non-equilibrium quantum-mechanical systems with correlational effects. We demonstrated how different approximation can be obtained in this framework and concluded with the embedding scheme for the G1–G2 scheme [15]. The embedding scheme enables us to reduce the computational cost of simulations of coupled systems in which the two subsystems are treated with different approximations.

Afterwards, we applied the time-local embedding scheme to physical situation of highly charged Xe ions interacting with monolayers of graphene and MoS_2 and described how the interaction between the two systems can be modeled using a single-band approximation for both materials, which was presented and used in [16, 28]. Using this model, we then simulated ion stopping experiments with the Hartree–Fock and second order Born approximations, in order to obtain the electron dynamics in the monolayers which play a key role in the modification of material properties and can not be directly observed in experiments. From the dynamics of the charge density in the monolayers, we concluded that due to the reduced carrier mobility in MoS_2, the electrons form stable doublons in the central rings where they accumulate as a result of the strong, attractive force of the highly charged ion. This doublon formation is exaggerated in the Hartree–Fock approximation and was reduced when including electronic correlations via the second order Born approximation. This mainly resulted in a reduction of the period of positive charge up in the center of the monolayer where the ion impacted the crystal. Including correlations in the simulation of the graphene monolayer did not have a significant effect except for the dampening of high frequency oscillations.

From the charge density dynamics, we calculated the electrostatic potential over the monolayer shortly after the ion impact to infer the emission rates of secondary electrons. Since we did not include the emission of electrons explicitly in the model, this method serves as a qualitative measure of the electron emission rate. We found that in MoS_2, the electron emission rate is reduced when compared to graphene. This finding was explained by the lowered carrier mobility in MoS_2, which resulted in an attractive electrostatic potential at the central ring of the cluster. This positive charge up would then act as a potential barrier for electrons emitted from the monolayer. In contrast, the electrostatic potential in graphene was repulsive as a consequence of the high carrier mobility, which resulted in a shorter period of positive charge in the center. These findings are in good agreement with the results of [16].

Using Koopmans' theorem, we obtained spectral information from the single particle Hamiltonian and saw that by including correlations in the simulation, the spectrum of MoS_2 was significantly changed after the ion impact. The resulting density of state resembled more the one of a conductor than a semiconductor, implying that the interaction with the ion changed the material properties of the monolayer. This effect was also reflected in the fact that the correlation energy was increased by the interaction with the ion.

As a last step, we showed that the framework allows for a more complex model of the materials by employing the 3-band model developed by the authors of Ref. [45] for the description of MoS_2 in our simulations. Due to the absence of an interaction term in this tight binding model, we found that the dynamics in the MoS_2 monolayer resembled those of graphene by effectively increasing the electron mobility in the cluster.

5.1 Charge transfer amplitude for MoS_2

In Sec. 3.2, we observed that while the parameters of Ref. [28] for the single band model were optimally tuned for SLG, the total charge transfer for MoS_2 computed in the simulations did not match the experimental results. The reason for this is that the charge transfer amplitude $\gamma_0 = 2.12$ was obtained by fitting the charge transfer model to said experimental results for SLG. The comparisons to the total charge transfer in MoS_2 experiments from Ref. [30] suggest that this amplitude is too large for MoS_2 targets and should be lowered. A separate fit to the MoS_2 could resolve this issue.
In the velocity dependency study, a modification of the hopping amplitudes, proportional to the difference in the Coulomb potential at both sites, was used, which we neglected in order to compare our results to those of Ref. [16]. There the authors used the simpler model without hopping modification. Preliminary results revealed that the total charge transfer measured in the experiments of Ref. [29] could also not be reproduced for SLG by neglecting the modification of the hopping amplitudes by the ion.
Further studies are necessary to gauge the effect and necessity of the hopping modification of the simulation results, which could then be used to find optimal parameters for SLG and MoS_2, respectively. However, as was demonstrated in this work, the simpler model without hopping modification and with the same charge transfer amplitudes is sufficient to reproduce qualitative differences between the materials. It should also be noted that the hopping modification is itself an approximation of the complex effect the Coulomb potential has on the spectral structure of the lattice. Therefore, a more accurate model will also depend on the model of the ion, which we will discuss in the following section.

5.2 Model of the ion

In order to find a minimal model for the ion that still captures the physics of the charge transfer process in some detail, the authors of Ref. [28] used hydrogen-like orbitals for the high-lying ion states. This model, while easy to study and implement, neglects the complex orbital structure of a heavy element such as Xe. Also, the neglect of dynamical processes of the electrons, once they have transferred to the ion should be noted. This simple model does not describe the relaxation of the ion towards a more stable, lower energy configuration. Of course, the timescale of the processes are also important, as we do not necessarily need to incorporate the relaxation of the ion, if it takes place on a much longer timescale than the charge transfer between the ion and the cluster. Further studies could shed light on the effect that a more complex model for the ion could have on the results of the simulation. However, accurate benchmarking data is difficult to obtain since the electron dynamics are not directly accessible by experimental measurements. In order to correctly assess the accuracy of a more complex ion model, one first needs to define observables which are sensitive to these changes and can be compared with experiments to avoid introducing unnecessary complexity in the description of the system.
It should also be noted that the minimal hydrogen-orbital model seems to reproduce the total charge transfer of the ion [28], while the explicit electronic structure of the ion is more relevant for Auger-processes and the ICD.
A more detailed analysis of the ionic states could also serve to improve the charge transfer model. The assumption of a Gaussian is based on experimental observations, but additional details could prove useful in the description of the coupling between the ion and the system.

5.3 Correlations

In this work, we have focused on comparing the HF approximation to the inclusions of correlations via SOA. However, the framework provided by the G1–G2 scheme provides several higher-order approximations, which include the different kinds of two-particle interactions, such as strong interactions via the T-matrix approximations or dynamical screening effects via the GW approximation. While these methods improve the description of correlations in the system, they also increase the computational cost of the simulations as well as introduce instabilities. Therefore, it is important to quantify the effects these approximations have on the results in this specific physical system, by comparing the emission of secondary electrons to experimental results, in order to decide which method to use. This highlights the problem of accurately benchmarking the results of the simulation, since correlational effects can be even more difficult to quantify and compare to experimental results, since representative observables have to be extracted in both cases. As we saw earlier in Sec. 3.5, the process of extracting observables such as spectral information can itself introduce approximations into the results.

In order to couple the ion to the cluster during the charge transfer, we used the embedding scheme with the approximation of neglecting electronic correlations both on the ion and in the charge transfer channels. This approach seems reasonable since the ion behaves roughly classically because of its large mass compared to the electrons and its low velocity. However, the neglect of all correlation functions

$$\mathcal{G}^{\mathrm{eeee}}, \quad \mathcal{G}^{\mathrm{eses}},$$

and so on, might introduce large systematic errors, especially in the case of the $s-e$ contributions. In order to properly gauge the accuracy of such an approximation, a detailed study of these contributions should be performed. For the specific system, it might be possible to find sound arguments for neglecting these contributions due to small, physical parameters. It would also be interesting to compare the embedding scheme with this approximation to the full treatment of correlations in both systems. This might, of course, only be feasible in a smaller, less complex basis, such as a one dimensional Hubbard chain, but it could provide valuable insights on the impact of these correlations on the overall results.

5.4 Spectral information via Koopmans' theorem

As mentioned above, in order to obtain comparable observables from the computed quantities, such as the single-particle Green's function, it is sometimes necessary to use approximative methods, such as Koopmans' theorem, for the spectral information. Methods like this, while widely used and well formulated, inevitably introduce systematic errors into the results. Especially, in the case of Koopmans' theorem where multi-particle effects are neglected in order to compute the spectrum. Assuming that the ionization spectrum is given by the single particle Hamiltonian alone, we can not fully quantify the effect correlations have on the spectrum. While comparisons between the spectra of HF and SOA simulations can imply some qualitative differences between the correlated and the uncorrelated system, the extent to which the interpretation of these differences is reliable is unclear. Especially in highly non-equilibrium situations, such as the point of resonant charge transfer between the ion and the cluster, the spectrum of the single particle Hamiltonian can change significantly on very short timescales. Therefore, the spectral resolution in these situations is not optimal, which requires averaging over a small temporal window. This then reduces the temporal resolution of the results. While extensions of the method exist, such as the extended Koopmans' theorem I [49], one should note that the problem lies in the time-diagonal framework itself. If we use methods like the G1–G2 scheme or reduced density matrix methods in order to benefit from the linear scaling in the simulation time, we effectively lose accurate spectral information, which is available for example in NEGF simulations. However, it is beneficial to have multiple independent methods at ones disposal. Also, the high temporal resolution time-diagonal methods offer, at a much smaller computational cost, can be important in many cases.

A possible solution was presented in [50], where the authors suggested a way to reconstruct spectral properties with dynamical correlations from off-diagonal contributions in a small neighborhood close to the time-diagonal. However, this method is not yet ready for application and is part of the current research into NEGF theory [51].

5.5 The 3-band model

In order to show the flexibility of the theoretical framework, we used the 3-band model presented in Ref. [45] to describe the MoS_2 monolayer as a substitute for the much simpler single-band model. When we used this model in the ion stopping simulation in Sec. 4.3, we kept the ion and charge transfer parameters unchanged. Since the more complex band structure should also have an effect on observables such as the total charge transfer, the parameters should be tuned to match the experimental results. In the single-band models, we assumed four non-interacting copies of the SLG π bands to participate in the charge transfer. This assumption does not seem sensible for the 3-band model, so we only included these three bands when calculating the charge transfer between the ion and the cluster as well as the charge density. That would imply that, in order to enable the ion to completely neutralize during the interaction, only charge states that are multiples of six can be considered, which makes the comparisons between the different models difficult. Further studies should be performed to tune the external parameters to work accurately with the 3-band model in order to obtain comparable results.

Since the 3-band model already includes an accurate reproduction of the bandgap calculated from DFT, it was not necessary to include a Hubbard repulsion term in the Hamiltonian of the cluster. This has the beneficial effect of enabling all simulations to be performed within the TB approximation, without requiring additional computation time for correlational effects. The downside of this approach is that the effects of higher-order approximations can not be tested in the 3-band model, since these rely on the electron-electron interactions in the system. Attempts to extend the model with a simple Hubbard interaction which acts only on electrons in the same orbitals did not prove fruitful, since this resulted mainly in the individual splitting of the three bands. More complex interaction models were also tried by approximating the Coulomb interactions between the three orbitals in order to introduce interband interactions between the orbitals. However, these efforts were also unsuccessful and, as stated before, the introduction of up to nine new free parameters into a model that has already been closely fitted to DFT data is challenging with the lack of representative measures of the quality of the model. A different approach, which could be applied to all other models as well, might be to incorporate long-range interactions via the Pariser–Parr–Popel model [52].

Appendix A Reduced density matrix theory

A.1 Equation of motion for $\hat{g}_{12}$

We start with the equations of motion for $\hat{F}_1$ and $\hat{F}_2$

$$i\hbar\frac{\partial}{\partial t}\hat{F}_1 - \big[\hat{T}_1, \hat{F}_1\big] = \mathrm{Tr}_2\big[\hat{V}_{12}, \hat{F}_{12}\big], \tag{A.1}$$

$$i\hbar\frac{\partial}{\partial t}\hat{F}_{12} - \big[\hat{T}_1 + \hat{T}_2 + \hat{V}_{12}, \hat{F}_{12}\big] = \mathrm{Tr}_3\big[\hat{V}_{13} + \hat{V}_{23}, \hat{F}_{123}\big]. \tag{A.2}$$

For the sake of readability we can introduce the following notation

$$\begin{aligned}
\hat{H}_1^{(0)} &:= \hat{T}_1, \\
\hat{H}_{12}^{(0)} &:= \hat{T}_1 + \hat{T}_2, \\
\hat{H}_{12} &:= \hat{H}_{12}^{(0)} + \hat{V}_{12}, \\
\hat{H}_1^{(\mathrm{H})} &:= \hat{T}_1 + \hat{U}_1^{(\mathrm{H})}, \\
\hat{U}_{12}^{(\mathrm{H})} &:= \hat{U}_1^{(\mathrm{H})} + \hat{U}_2^{(\mathrm{H})}, \\
\hat{H}_{12}^{(\mathrm{H})} &:= \hat{H}_{12}^{(0)} + \hat{U}_{12}^{(\mathrm{H})}.
\end{aligned}$$

We already saw that with the reconstruction of the 2-pRDM

$$\hat{F}_{12} = \hat{F}_1\hat{F}_2 + \hat{g}_{12}, \tag{A.3}$$

we can write Eq. (A.1) in the following form, using the Hartree potential

$$i\hbar\frac{\partial}{\partial t}\hat{F}_1 - \big[\hat{H}_1^{(\mathrm{H})}, \hat{F}_1\big] = \mathrm{Tr}_2\big[\hat{V}_{12}, \hat{g}_{12}\big]. \tag{A.4}$$

Now we want to use the cluster expansion

$$\hat{F}_{123} = \hat{F}_1\hat{F}_2\hat{F}_3 + \hat{F}_1\hat{g}_{23} + \hat{F}_2\hat{g}_{13} + \hat{F}_3\hat{g}_{12} + \hat{g}_{123}, \tag{A.5}$$

to derive an equation of motion for the correlation operator $\hat{g}_{12}$. We start by inserting Eq. (A.3) into the EOM for $\hat{F}_{12}$ (Eq. (A.2))

$$i\hbar\frac{\partial}{\partial t}\big(\hat{F}_1\hat{F}_2\big) - \big[\hat{H}_{12}, \hat{F}_1\hat{F}_2\big] + i\hbar\frac{\partial}{\partial t}\hat{g}_{12} - \big[\hat{H}_{12}, \hat{g}_{12}\big] = \mathrm{Tr}_3\big[\hat{V}_{13} + \hat{V}_{23}, \hat{F}_{123}\big]. \tag{A.6}$$

Using Eq. (A.4) we can eliminate the derivative of the product $\hat{F}_1\hat{F}_2$

$$\begin{aligned}
i\hbar\frac{\partial}{\partial t}\big(\hat{F}_1\hat{F}_2\big) &= i\hbar\hat{F}_1\frac{\partial}{\partial t}\hat{F}_2 + i\hbar\frac{\partial}{\partial t}\big(\hat{F}_1\big)\hat{F}_2 \\
&= \hat{F}_1\bigg(\big[\hat{H}_2^{(\mathrm{H})}, \hat{F}_2\big] + \mathrm{Tr}_3\big[\hat{V}_{23}, \hat{g}_{23}\big]\bigg) + \bigg(\big[\hat{H}_1^{(\mathrm{H})}, \hat{F}_1\big] + \mathrm{Tr}_3\big[\hat{V}_{13}, \hat{g}_{13}\big]\bigg)\hat{F}_2 \\
&= \big[\hat{H}_{12}^{(\mathrm{H})}, \hat{F}_1\hat{F}_2\big] + \mathrm{Tr}_3\bigg(\big[\hat{V}_{13}, \hat{g}_{13}\hat{F}_2\big] + \big[\hat{V}_{23}, \hat{g}_{23}\hat{F}_1\big]\bigg).
\end{aligned}$$

Inserting this expression in Eq. (A.6) we are left with

$$i\hbar\frac{\partial}{\partial t}\hat{g}_{12} - \big[\hat{H}_{12}, \hat{g}_{12}\big] = \big[\hat{V}_{12} - \hat{U}_{12}^{(\mathrm{H})}, \hat{F}_1\hat{F}_2\big] + \mathrm{Tr}_3\bigg(\big[\hat{V}_{13} + \hat{V}_{23}, \hat{F}_{123}\big] - \big[\hat{V}_{13}, \hat{g}_{13}\hat{F}_2\big] - \big[\hat{V}_{23}, \hat{g}_{23}\hat{F}_1\big]\bigg). \tag{A.7}$$

In fact we are already able to identify the ladder term

$$\big[\hat{H}_{12}, \hat{g}_{12}\big] = \big[\hat{H}_{12}^{(0)}, \hat{g}_{12}\big] + \hat{L}_{12}, \quad \hat{L}_{12} \coloneqq \big[\hat{V}_{12}, \hat{g}_{12}\big].$$

Further simplification of the EOM requires us to insert the cluster expansion (Eq. A.5). Since this expression is too long, we will start with the commutator with $\hat{F}_{123}$ and try to identify terms in there

$$\begin{aligned}\mathrm{Tr}_3\big[\hat{V}_{13} + \hat{V}_{23}, \hat{F}_{123}\big] &= \mathrm{Tr}_3\bigg(\big[\hat{V}_{13}, \hat{F}_1\hat{F}_2\hat{F}_3 + \hat{F}_1\hat{g}_{23} + \hat{F}_2\hat{g}_{13} + \hat{F}_3\hat{g}_{12} + \hat{g}_{123}\big] \\ &\qquad + \big[\hat{V}_{23}, \hat{F}_1\hat{F}_2\hat{F}_3 + \hat{F}_1\hat{g}_{23} + \hat{F}_2\hat{g}_{13} + \hat{F}_3\hat{g}_{12} + \hat{g}_{123}\big]\bigg) \\ &= \big[\hat{U}_{12}^{(\mathrm{H})}, \hat{F}_1\hat{F}_2\big] + \big[\hat{U}_{12}^{(\mathrm{H})}, \hat{g}_{12}\big] + \hat{C}_{12} + \hat{A}_{12} + \hat{B}_{12}. \end{aligned} \tag{A.8}$$

We can already see that the Hartree terms in Eq. (A.7) and Eq. (A.8) cancel out. Also we were able to identify the three particle correlation contribution

$$\hat{C}_{12} \coloneqq \mathrm{Tr}_3\big[\hat{V}_{13} + \hat{V}_{23}, \hat{g}_{123}\big].$$

So the EOM currently looks like

$$i\hbar\frac{\partial}{\partial t}\hat{g}_{12} - \big[\hat{H}_{12}^{(\mathrm{H})}, \hat{g}_{12}\big] = \hat{\Psi}_{12} + \hat{L}_{12} + \hat{C}_{12} + \underbrace{\hat{A}_{12} - \mathrm{Tr}_3\big[\hat{V}_{13}, \hat{g}_{13}\hat{F}_2\big]}_{\tilde{A}_{12}} + \underbrace{\hat{B}_{12} - \big[\hat{V}_{23}, \hat{g}_{23}\hat{F}_1\big]}_{\tilde{B}_{12}},$$

where we also identified the SOA term

$$\hat{\Psi}_{12} = \big[\hat{V}_{12}, \hat{F}_1\hat{F}_2\big].$$

Now all that is left are these $\tilde{A}, \tilde{B}$ terms, which we already know will contain the polarization terms. Lets start by looking at the first term

$$\begin{aligned}\tilde{A}_{12} &= \mathrm{Tr}_3\bigg(\big[\hat{V}_{13}, \hat{F}_1\hat{g}_{23} + \hat{F}_2\hat{g}_{13}\big] - \big[\hat{V}_{13}, \hat{F}_2\hat{g}_{13}\big]\bigg) \\ &= \mathrm{Tr}_3\big[\hat{V}_{13}, \hat{F}_1\hat{g}_{23}\big]\end{aligned}$$

And the second term contracts analogously

$$\tilde{B}_{12} = \mathrm{Tr}_3\big[\hat{V}_{13}, \hat{F}_1\hat{g}_{23}\big].$$

Together both terms add up to the polarization contribution

$$\tilde{A}_{12} + \tilde{B}_{12} = \mathrm{Tr}_3\bigg(\big[\hat{V}_{13}, \hat{F}_1\hat{g}_{23}\big] + \big[\hat{V}_{23}, \hat{F}_2\hat{g}_{13}\big]\bigg) \eqqcolon \hat{\Pi}_{12}.$$

So in total we get the full EOM for $\hat{g}_{12}$

$$\begin{aligned}i\hbar\frac{\partial}{\partial t}\hat{g}_{12} - \big[\hat{H}_{12}^{(\mathrm{H})}, \hat{g}_{12}\big] &= \hat{\Psi}_{12} + \hat{L}_{12} + \hat{\Pi}_{12} + \hat{C}_{12}, \\ \hat{H}_{12}^{(\mathrm{H})} &= \hat{T}_1 + \hat{T}_2 + \mathrm{Tr}_3\hat{V}_{13}\hat{F}_3 + \mathrm{Tr}_3\hat{V}_{23}\hat{F}_3, \\ \hat{\Psi}_{12} &= \big[\hat{V}_{12}, \hat{F}_1\hat{F}_2\big], \\ \hat{L}_{12} &= \big[\hat{V}_{12}, \hat{g}_{12}\big], \\ \hat{\Pi}_{12} &= \mathrm{Tr}_3\bigg(\big[\hat{V}_{13}, \hat{F}_1\hat{g}_{23}\big] + \big[\hat{V}_{23}, \hat{F}_2\hat{g}_{13}\big]\bigg), \\ \hat{C}_{12} &= \mathrm{Tr}_3\big[\hat{V}_{13} + \hat{V}_{23}, \hat{g}_{123}\big].\end{aligned}$$

A.2 Equation of motion for $\hat{g}_{12}^{-}$

We start with the equations of motion for $\hat{F}_1$ and $\hat{F}_{12}$[1]

$$i\hbar\frac{\partial}{\partial t}\hat{F}_1 - \big[\hat{H}_1^{(0)}, \hat{F}_1\big] = \mathrm{Tr}_2\big[\hat{V}_{12}, \hat{F}_{12}\big], \tag{A.9}$$

$$i\hbar\frac{\partial}{\partial t}\hat{F}_{12} - \big[\hat{H}_{12}, \hat{F}_{12}\big] = \mathrm{Tr}_3\big[\hat{V}_{13} + \hat{V}_{23}, \hat{F}_{123}\big]. \tag{A.10}$$

---

[1] see Sec. A.1 for definitions

To account for the fermionic particle exchange symmetry we have to slightly modify the reconstruction of the 2- and 3-pRDMs, so that

$$\hat{F}^{-}_{12} = -\hat{F}^{-}_{21}.$$

This is accomplished using the antisymmetrization operator (ASO) $\hat{\Lambda}^{-}_{12}$ defined as[2]

$$\hat{\Lambda}^{-}_{12} = \big(1 - \hat{P}_{12}\big), \quad \hat{P}_{12}\left|i,j\right\rangle = \left|j,i\right\rangle.$$

The antisymmetric reconstruction of the 2-pRDM reads

$$\hat{F}^{-}_{12} = \hat{\Lambda}^{-}_{12}\hat{F}_1\hat{F}_2 + \hat{\Lambda}^{-}_{12}\hat{g}_{12} = \hat{\Lambda}^{-}_{12}\hat{F}_1\hat{F}_2 + \hat{g}^{-}_{12}, \tag{A.11}$$

Here we absorbed the ASO into $\hat{g}^{-}_{12}$ so that in the EOM we will get explicit exchange contributions. Substituting this reconstruction into the right hand side of Eq. (A.9) we get

$$i\hbar\frac{\partial}{\partial t}\hat{F}_1 - \big[\hat{H}_1, \hat{F}_1\big] = \mathrm{Tr}_2\Big(\big[\hat{V}_{12}, \hat{\Lambda}^{-}_{12}\hat{F}_1\hat{F}_2\big] + \big[\hat{V}_{12}, \hat{g}^{-}_{12}\big]\Big).$$

To understand the first term on the right hand side, we have to take a closer look at the commutator

$$\begin{aligned}\mathrm{Tr}_2\big[\hat{V}_{12}, \hat{\Lambda}^{-}_{12}\hat{F}_1\hat{F}_2\big] &= \mathrm{Tr}_2\big[\hat{V}_{12}, \hat{F}_1\hat{F}_2\big] - \mathrm{Tr}_2\big[\hat{V}_{12}, \hat{P}_{12}\hat{F}_1\hat{F}_2\big]\\ &= \big[\hat{U}^{(\mathrm{H})}_1, \hat{F}_1\big] - \mathrm{Tr}_2\big(\hat{V}_{12}\hat{P}_{12}\hat{F}_1\hat{F}_2 - \hat{P}_{12}\hat{F}_1\hat{F}_2\hat{V}_{12}\big]\\ &= \big[\hat{U}^{(\mathrm{H})}_1, \hat{F}_1\big] - \mathrm{Tr}_2\big(\hat{V}_{12}\hat{P}_{12}\hat{F}_1\hat{F}_2 - \hat{F}_2\hat{F}_1\hat{V}_{21}\hat{P}_{12}\big),\end{aligned}$$

where in the last line we exchanged the permutation operator with the density matrix operators with

$$\hat{P}_{12}\hat{F}_1 = \hat{F}_2\hat{P}_{12}.$$

Of course since $\hat{F}_1$ and $\hat{F}_2$ live in different subspaces, their order does not matter and we always expect a symmetric interaction potential with $\hat{V}_{12} = \hat{V}_{21}$ we can write

$$\begin{aligned}\mathrm{Tr}_2\big[\hat{V}_{12}, \hat{\Lambda}^{-}_{12}\hat{F}_1\hat{F}_2\big] &= \big[\hat{U}^{(\mathrm{H})}_1, \hat{F}_1\big] - \mathrm{Tr}_2\big[\hat{V}_{12}\hat{P}_{12}\hat{F}_2, \hat{F}_1\big]\\ &=: \big[\hat{U}^{(\mathrm{HF})}_1, \hat{F}_1\big] = \big[\mathrm{Tr}_2\hat{V}^{-}_{12}, \hat{F}_1\big] = \big[\mathrm{Tr}_2\hat{V}_{12}\hat{\Lambda}^{-}_{12}\hat{F}_2, \hat{F}_1\big].\end{aligned}$$

Here we introduced the so-called Fock-potential

$$\hat{U}^{(\mathrm{F})}_1 =: \mathrm{Tr}_2\hat{V}_{12}\hat{P}_{12}\hat{F}_2,$$

which is similar to the Hartree term but instead includes exchange effects with the rest of the particles. The full EOM for $\hat{F}_1$ then reads

$$i\hbar\frac{\partial}{\partial t}\hat{F}_1 - \big[\hat{H}^{(\mathrm{HF})}_1, \hat{F}_1\big] = \mathrm{Tr}_2\big[\hat{V}_{12}, \hat{g}^{-}_{12}\big], \quad \hat{H}^{(\mathrm{HF})}_1 := \hat{H}^{(\mathrm{H})}_1 + \hat{U}^{(\mathrm{F})}_1.$$

In the following we will derive the equation of motion for $\hat{g}_{12}$ using a method which is slightly faster than the one employed in [11] and [7].
We start by looking at the antisymmetric cluster expansion (ACE)

$$\hat{F}^{-}_{123} = \hat{F}_1\hat{F}_2\hat{F}_3\hat{\Lambda}^{-}_{123} + \big(\hat{F}_1\hat{g}_{23} + \hat{F}_2\hat{g}_{13} + \hat{F}_3\hat{g}_{12}\big)\hat{\Lambda}^{-}_{123} + \hat{g}^{-}_{123}.$$

Using the following properties of the ASO

$$\begin{aligned}\hat{\Lambda}^{-}_{12} &= \big(1 - \hat{P}_{12}\big),\\ \hat{\Lambda}^{-}_{(12),3} &= \big(1 - \hat{P}_{13} - \hat{P}_{23}\big),\\ \hat{\Lambda}^{-}_{123} &= \hat{\Lambda}^{-}_{12}\hat{\Lambda}^{-}_{(12),3} = \hat{\Lambda}^{-}_{13}\hat{\Lambda}^{-}_{(13),2} = \hat{\Lambda}^{-}_{23}\hat{\Lambda}^{-}_{(23),1},\\ \hat{\Lambda}^{-}_{123}\hat{F}^{-}_{123} &= \hat{F}^{-}_{123}\hat{\Lambda}^{-}_{123},\end{aligned}$$

---

[2] Note that the scope of this derivation is set on fermionic systems. However, we can switch to bosonic systems simply by changing the sign in the antisymmetrization operator, making it a symmetrization operator. The rest of the derivation will not change.

we can rewrite the ACE in four equivalent forms

$$\hat{F}^-_{123} = \hat{F}^-_{13}\hat{F}_2\hat{\Lambda}^-_{(13),2} + \hat{g}_{23}\hat{F}_1\hat{\Lambda}^-_{(23),1} + \hat{g}^-_{12}\hat{F}_3\hat{\Lambda}^-_{(12),3} + \hat{g}^-_{123}, \tag{A.12}$$

$$\hat{F}^-_{123} = \hat{F}^-_{23}\hat{F}_1\hat{\Lambda}^-_{(23),1} + \hat{g}^-_{13}\hat{F}_2\hat{\Lambda}^-_{(13),2} + \hat{g}^-_{12}\hat{F}_3\hat{\Lambda}^-_{(12),3} + \hat{g}^-_{123}, \tag{A.13}$$

$$\hat{F}^-_{123} = \hat{\Lambda}_{(13),2}\hat{F}_2\hat{F}^-_{13} + \hat{\Lambda}_{(23),1}\hat{F}_1\hat{g}^-_{23} + \hat{\Lambda}^-_{(12),3}\hat{F}_3\hat{g}^-_{12} + \hat{g}^-_{123}, \tag{A.14}$$

$$\hat{F}^-_{123} = \hat{\Lambda}_{(23),1}\hat{F}_1\hat{F}^-_{23} + \hat{\Lambda}_{(13),2}\hat{F}_2\hat{g}^-_{13} + \hat{\Lambda}^-_{(12),3}\hat{F}_3\hat{g}^-_{12} + \hat{g}^-_{123}. \tag{A.15}$$

We also make the sensible definition of

$$i\hbar\frac{\partial}{\partial t}\hat{F}_1 - \big[\hat{H}^{(0)}_1, \hat{F}_1\big] = \mathrm{Tr}_2\big[\hat{V}_{12}, \hat{F}^-_{12}\big] =: \hat{I}^-_1,$$

with which we can write the temporal derivative of the ideal, antisymmetric product as

$$i\hbar\frac{\partial}{\partial t}\big(\hat{F}_1\hat{F}_2\big)\hat{\Lambda}^-_{12} - \big[\hat{H}^{(0)}_{12}, \hat{F}_1\hat{F}_2\hat{\Lambda}^-_{12}\big] = \big(\hat{I}^-_1\hat{F}_2 + \hat{I}_2\hat{F}_1\big)\hat{\Lambda}^-_{12}. \tag{A.16}$$

By substituting Eq. (A.11) into Eq. (A.10) and subtracting Eq. (A.16) we get

$$i\hbar\frac{\partial}{\partial t}\hat{g}^-_{12} - \big[\hat{H}^{(0)}_{12}, \hat{g}^-_{12}\big] = \big[\hat{V}_{12}, \hat{F}^-_{12}\big] - \big(\hat{I}^-_1\hat{F}_2 + \hat{I}^-_2\hat{F}_1\big) + \mathrm{Tr}_3\big[\hat{V}_{13} + \hat{V}_{23}, \hat{F}^-_{123}\big]. \tag{A.17}$$

Lets now focus on the coupling to the 3-pRDM. Evaluating the commutator leads to four terms

$$\begin{aligned} &\mathrm{Tr}_3\hat{V}_{13}\hat{F}^-_{123}, \quad -\mathrm{Tr}_3\hat{F}^-_{123}\hat{V}_{13}, \\ &\mathrm{Tr}_3\hat{V}_{23}\hat{F}^-_{123}, \quad -\mathrm{Tr}_3\hat{F}^-_{123}\hat{V}_{23}. \end{aligned}$$

To greatly reduce the effort for the following derivation we will use a different expression for the 3-pRDM in each of these terms. Starting with the first term, we will use Eq. (A.12) and obtain[3]

$$\mathrm{Tr}_3\hat{V}_{13}\hat{F}^-_{123} = \mathrm{Tr}_3\hat{V}_{13}\hat{F}^-_{13}\hat{F}_2\hat{\Lambda}^-_{(13),2} + \underbrace{\mathrm{Tr}_3\hat{V}_{13}\big(\hat{g}^-_{12}\hat{F}_3\hat{\Lambda}^-_{(12),3} - \hat{g}^-_{23}\hat{F}_1\hat{\Lambda}^-_{(23),1}\big)}_{\hat{A}^{(1)}_1} + \underbrace{\mathrm{Tr}_3\hat{V}_{13}\hat{g}^-_{123}}_{\hat{C}^{-,(1)}_1}.$$

We can simplify the first term by making use of the definition of $\hat{\Lambda}^-_{(13),2}$ and $\hat{I}^-_1$

$$\begin{aligned} \mathrm{Tr}_3\hat{V}_{13}\hat{F}^-_{13}\hat{F}_2\hat{\Lambda}^-_{(13),2} &= \mathrm{Tr}_3\hat{V}_{13}\hat{F}^-_{13}\hat{F}_2 - \mathrm{Tr}_3\hat{V}_{13}\hat{F}^-_{13}\hat{F}_2\hat{P}_{12} - \mathrm{Tr}_3\hat{V}_{13}\hat{F}^-_{13}\hat{P}_{32}\hat{F}_2 \\ &= \hat{I}^{-,(1)}_1\hat{F}_2\hat{\Lambda}^-_{12} - \hat{F}_2\mathrm{Tr}_3\hat{P}_{23}\hat{V}_{12}\hat{F}^-_{12} \\ &= \hat{I}^{-,(1)}_1\hat{F}_2\hat{\Lambda}^-_{12} - \hat{F}_2\hat{V}_{12}\hat{F}^-_{12}, \end{aligned}$$

where we used in the second line

$$\hat{V}_{13}\hat{F}^-_{13}\hat{P}_{32} = \hat{P}_{32}\hat{V}_{12}\hat{F}^-_{12}$$

and in the third line

$$\mathrm{Tr}_3\hat{P}_{32} = \hat{1}.$$

Analogously for the second term of the commutator above together with Eq. (A.13) we get

$$\mathrm{Tr}_3\hat{F}^-_{123}\hat{V}_{13} = \hat{\Lambda}^-_{12}\hat{I}^{-,(2)}\hat{F}_2 - \hat{F}^-_{12}\hat{V}_{12}\hat{F}_2 + \hat{A}^{(2)}_1 + \hat{C}^{(2)}_1.$$

The third and fourth terms of the commutator together with Eq. (A.14) and Eq. (A.15) give

$$\begin{aligned} \mathrm{Tr}_3\hat{V}_{23}\hat{F}^-_{123} &= \hat{I}^{-,(1)}_2\hat{F}_1\hat{\Lambda}^-_{12} - \hat{F}_1\hat{V}_{12}\hat{F}^-_{12} + \hat{A}^{(1)}_2 + \hat{C}^{-,(1)}_2, \\ \mathrm{Tr}_3\hat{F}^-_{123}\hat{V}_{23} &= \hat{\Lambda}^-_{12}\hat{I}^{-,(2)}_2\hat{F}_1 - \hat{F}^-_{12}\hat{V}_{12}\hat{F}_1 + \hat{A}^{(2)}_2 + \hat{C}^{-,(2)}_2. \end{aligned}$$

---

[3] Note that subscripts will always refer to the relevant subspaces, while the superscripts $(1), (2)$ will refer to the first or second term of the commutator: $C = [A, B] = C^{(1)} - C^{(2)}$.

Finally, collecting all results with their respective signs leads to

$$\mathrm{Tr}_3\big[\hat{V}_{13}+\hat{V}_{23},\hat{F}^-_{123}\big]=\hat{A}_1+\hat{A}_2+\big(\hat{I}^-_1\hat{F}_2+\hat{I}^-_2\hat{F}_1\big)\hat{\Lambda}^-_{12}-\big\{\big(\hat{F}_1+\hat{F}_2\big)\hat{V}_{12}\hat{F}^-_{12}-\hat{F}^-_{12}\hat{V}_{12}\big(\hat{F}_1+\hat{F}_2\big)\big\}+\hat{C}^-_{12}.$$

Inserting our result back into Eq. (A.17) we find that the $\hat{I}^-$ terms cancel

$$i\hbar\frac{\partial}{\partial t}\hat{g}_{12}-\big[\hat{H}^{(0)}_{12},\hat{g}_{12}\big]=\big(\hat{1}-\hat{F}_1-\hat{F}_2\big)\hat{V}_{12}\hat{F}^-_{12}-\hat{F}^-_{12}\hat{V}_{12}\big(\hat{1}-\hat{F}_1-\hat{F}_2\big)+\hat{A}_1+\hat{A}_2+\hat{C}^-_{12}.$$

Using the definitions for the Pauli-blocked interaction potential

$$\begin{aligned}\tilde{V}_{12}&:=\big(\hat{1}-\hat{F}_1-\hat{F}_2\big)\hat{V}_{12},\\ \tilde{V}^-_{12}&:=\tilde{V}_{12}\hat{\Lambda}^-_{12},\end{aligned}$$

and inserting Eq. (A.11) we can simplify the expression further to

$$i\hbar\frac{\partial}{\partial t}\hat{g}^-_{12}-\big[\hat{H}^{(0)}_{12},\hat{g}^-_{12}\big]=\underbrace{\tilde{V}^-_{12}\hat{F}_1\hat{F}_2-\hat{F}_1\hat{F}_2\tilde{V}^{-,\dagger}_{12}}_{\hat{\Psi}^-_{12}}+\underbrace{\tilde{V}_{12}\hat{g}^-_{12}-\hat{g}^-_{12}\tilde{V}^\dagger_{12}}_{\hat{L}^-_{12}}+\hat{A}_1+\hat{A}_2+\hat{C}^-_{12}. \tag{A.18}$$

Lets summarize what we have found so far:

I. The modified inhomogeneity $\hat{\Psi}^-_{12}$ that includes SOA effects with exchange contributions

II. The modified ladder contributions $\hat{L}^-_{12}$ that include particle-particle T-matrix effects with Pauli-blocking

III. And the three particle correlation integral $\hat{C}^-_{12}$

The missing polarization effects, as well as the particle-hole T-matrix contributions will be found by evaluating the terms $\hat{A}_1$ and $\hat{A}_2$.
Starting with

$$\begin{aligned}\hat{A}^{(1)}_1&=\mathrm{Tr}_3\hat{V}_{13}\big(\hat{g}^-_{12}\hat{F}_3\hat{\Lambda}^-_{(12),3}+\hat{g}^-_{23}\hat{F}_1\hat{\Lambda}^-_{(23),1}\big)\\ &=\mathrm{Tr}_3\hat{V}_{13}\big(\underbrace{\hat{g}^-_{12}\hat{F}_3}_{I}\underbrace{-\hat{g}^-_{12}\hat{F}_3\hat{P}_{13}}_{II}\underbrace{-\hat{g}^-_{12}\hat{F}_3\hat{P}_{23}}_{III}\\ &\qquad\underbrace{+\hat{g}^-_{23}\hat{F}_1}_{IV}\underbrace{-\hat{g}^-_{23}\hat{F}_1\hat{P}_{12}}_{V}\underbrace{-\hat{g}^-_{23}\hat{F}_1\hat{P}_{13}}_{VI}\big),\end{aligned}$$

where we can identify the Hartree-Fock potential from I and VI by bringing $\hat{P}_{13}$ all the way to the left

$$\hat{U}^{(\mathrm{HF})}_1\hat{g}^-_{12}=\mathrm{Tr}_3\big(\hat{V}_{13}-\hat{V}_{13}\hat{P}_{13}\big)\hat{F}_3\hat{g}^-_{12}.$$

Also, terms II and IV together form

$$\mathrm{Tr}_3\big(\hat{V}_{13}-\hat{V}_{13}\hat{P}_{12}\big)\hat{g}^-_{23}\hat{F}_1=\mathrm{Tr}_3\hat{V}^-_{13}\hat{g}^-_{23}\hat{F}_1.$$

Finally, to combine III and V, we first need to bring III into the right form

$$\begin{aligned}\hat{g}^-_{12}\hat{F}_3\hat{P}_{23}&=\hat{F}_3\hat{g}^-_{12}\hat{\Lambda}^-_{12}\hat{P}_{23}\\ &=-\hat{F}_3\hat{g}^-_{12}\hat{P}_{13}\hat{\Lambda}^-_{23}\hat{P}_{12}\\ &=-\hat{P}_{13}\hat{F}_1\hat{g}^-_{23}\hat{P}_{12},\end{aligned}$$

where in the second line, we used the identity

$$\begin{aligned}\hat{\Lambda}^-_{12}\hat{P}_{23}&=\hat{1}\cdot\hat{P}_{23}-\hat{P}_{12}\hat{P}_{23}=\hat{P}^2_{13}\hat{P}_{23}-\hat{P}_{13}\hat{P}_{12}\\ &=\big(\hat{P}_{13}\hat{P}_{23}-\hat{P}_{13}\big)\hat{P}_{12}=-\hat{P}_{13}\big(-\hat{P}_{23}+\hat{1}\big)\hat{P}_{12}=-\hat{P}_{13}\hat{\Lambda}^-_{23}\hat{P}_{12}.\end{aligned}$$

Now we can combine III and V to

$$\mathrm{Tr}_3\hat{V}_{13}\big(\hat{P}_{13}\hat{F}_1\hat{g}^-_{23}\hat{P}_{12}-\hat{g}^-_{23}\hat{F}_1\big)=-\mathrm{Tr}_3\big(\hat{V}_{13}-\hat{V}_{13}\hat{P}_{13}\big)\hat{g}^-_{23}\hat{F}_1=-\mathrm{Tr}_3\hat{V}^-_{13}\hat{g}^-_{23}\hat{F}_1.$$

All results combined yield

$$\hat{A}_1^{(1)} = \hat{U}_1^{(\mathrm{HF})}\hat{g}_{12}^{-} + \mathrm{Tr}_3\hat{V}_{13}^{-}\hat{g}_{23}^{-}\hat{F}_1\hat{\Lambda}_{12}^{-}.$$

If we apply the same strategy to all other parts of the $\hat{A}$ terms we find

$$\hat{A}_1 + \hat{A}_2 = \big[\hat{U}_1^{(\mathrm{HF})} + \hat{U}_2^{(\mathrm{HF})}, \hat{g}_{12}^{-}\big] + \underbrace{\mathrm{Tr}_3\Bigg(\big[\hat{V}_{13}^{-}, \hat{g}_{23}^{-}\hat{F}_1\big]\hat{\Lambda}_{12}^{-} + \big[\hat{V}_{23}^{-}, \hat{g}_{13}^{-}\hat{F}_2\big]\hat{\Lambda}_{12}^{-}\Bigg)}_{\hat{\Pi}_{12}^{-}}.$$

Inserting this final result into Eq. (A.18) we get

$$\begin{aligned}
i\hbar\frac{\partial}{\partial t}\hat{g}_{12}^{-} - \big[\hat{H}_{12}^{(\mathrm{HF})}, \hat{g}_{12}^{-}\big] &= \hat{\Psi}_{12}^{-} + \hat{L}_{12}^{-} + \hat{\Pi}_{12}^{-} + \hat{C}_{12}^{-},\\
\hat{\Psi}_{12}^{-} &= \tilde{V}_{12}^{-}\hat{F}_1\hat{F}_2 - \hat{F}_1\hat{F}_2\tilde{V}_{12}^{-,\dagger},\\
\hat{L}_{12}^{-} &= \tilde{V}_{12}\hat{g}_{12}^{-} - \hat{g}_{12}^{-}\tilde{V}_{12}^{\dagger},\\
\hat{\Pi}_{12}^{-} &= \mathrm{Tr}_3\Bigg(\big[\hat{V}_{13}^{-}, \hat{g}_{23}^{-}\hat{F}_1\big] + \big[\hat{V}_{23}^{-}, \hat{g}_{13}^{-}\hat{F}_2\big]\Bigg)\hat{\Lambda}_{12}^{-},\\
\hat{C}_{12}^{-} &= \mathrm{Tr}_3\big[\hat{V}_{13} + \hat{V}_{23}, \hat{g}_{123}^{-}\big],\\
\hat{H}_{12}^{(\mathrm{HF})} &= \hat{H}_{12}^{(0)} + \hat{U}_1^{(\mathrm{HF})} + \hat{U}_2^{(\mathrm{HF})},\\
\tilde{V}_{12}^{-} &= \big(\hat{1} - \hat{F}_1 - \hat{F}_2\big)\hat{V}_{12}^{-}, \quad \hat{V}_{12}^{-} = \hat{V}_{12}\hat{\Lambda}_{12}^{-},
\end{aligned}$$

which is the DSL approximation[4] with exchange effects.

---

[4] For $\hat{g}_{123}^{-} = 0$

Appendix B Simulation parameters

N_s	Σ	ϵ/J_0	J/J_0	U/J_0	λ	a/a_0	γ
24	HF	1.22	0.74	1.19	0.153	1	2.12

Table B.1: Simulation parameters for Fig. 3.4. Cluster size N_s, equivalent self-energy approximation Σ, on-site energy ϵ, hopping amplitude J, Hubbard interaction U, hopping modification λ, lattice spacing a and charge transfer amplitude γ. Units are $J_0 = 3.78\,\mathrm{eV}$ and $a_0 = 1.42\,\text{Å}$.

Material	N_s	Σ	ϵ/J_0	J/J_0	U/J_0	λ	a/a_0	γ
SLG	24	HF	1.22	0.74	1.19	0.153	1	2.12
MoS_2	24	HF	1.19	0.19	1.19	0.153	1.29	2.12

Table B.2: Simulation parameters for Fig. 3.5. Cluster size N_s, equivalent self-energy approximation Σ, on-site energy ϵ, hopping amplitude J, Hubbard interaction U, hopping modification λ, lattice spacing a and charge transfer amplitude γ for both materials SLG and MoS_2. Units are $J_0 = 3.78\,\mathrm{eV}$ and $a_0 = 1.42\,\text{Å}$.

Material	N_s	Σ	ϵ/J_0	J/J_0	U/J_0	λ	a/a_0	γ	$v_z^{(\mathrm{ion})}/v_0$
MoS_2	150	HF	1.19	0.19	1.19	0	1.29	2.12	0.4996

Table B.3: Simulation parameters for Fig. 3.7. Cluster size N_s, equivalent self-energy approximation Σ, on-site energy ϵ, hopping amplitude J, Hubbard interaction U, hopping modification λ, lattice spacing a, charge transfer amplitude γ and ion velocity $v_z^{(\mathrm{ion})}$ for both materials SLG and MoS_2. Units are $J_0 = 3.78\,\mathrm{eV}$, $a_0 = 1.42\,\text{Å}$ and $v_0 = 0.82\,\mathrm{nm/fs}$.

Material	N_s	Σ	ϵ/J_0	J/J_0	U/J_0	λ	a/a_0	γ	$v_z^{(\mathrm{ion})}/v_0$
MoS_2	150	HF	1.19	0.19	1.19	0	1.29	2.12	0.4996
MoS_2	150	SOA	1.19	0.19	1.19	0	1.29	2.12	0.4996

Table B.4: Simulation parameters for Fig. 3.8. Cluster size N_s, equivalent self-energy approximation Σ, on-site energy ϵ, hopping amplitude J, Hubbard interaction U, hopping modification λ, lattice spacing a, charge transfer amplitude γ and ion velocity $v_z^{(\mathrm{ion})}$ for MoS_2. Units are $J_0 = 3.78\,\mathrm{eV}$, $a_0 = 1.42\,\text{Å}$ and $v_0 = 0.82\,\mathrm{nm/fs}$.

Material	N_s	Σ	ϵ/J_0	J/J_0	U/J_0	λ	a/a_0	γ	$v_z^{(\mathrm{ion})}/v_0$
MoS_2	150	SOA	1.19	0.19	1.19	0	1.29	2.12	0.4996
SLG	150	SOA	1.22	0.74	1.19	0	1	2.12	0.4996

Table B.5: Simulation parameters for Fig. 3.10. Cluster size N_s, equivalent self-energy approximation Σ, on-site energy ϵ, hopping amplitude J, Hubbard interaction U, hopping modification λ, lattice spacing a, charge transfer amplitude γ and ion velocity $v_z^{(\mathrm{ion})}$ for MoS_2. Units are $J_0 = 3.78\,\mathrm{eV}$, $a_0 = 1.42\,\text{Å}$ and $v_0 = 0.82\,\mathrm{nm/fs}$.

Material	N_s	Σ	ϵ/J_0	J/J_0	U/J_0	λ	a/a_0	γ	$v_z^{(\mathrm{ion})}/v_0$
MoS_2	24	SOA	1.19	0.19	1.19	0	1.29	2.12	0.4996
MoS_2	54	SOA	1.19	0.19	1.19	0	1.29	2.12	0.4996
MoS_2	96	SOA	1.19	0.19	1.19	0	1.29	2.12	0.4996
MoS_2	150	SOA	1.19	0.19	1.19	0	1.29	2.12	0.4996

Table B.6: Simulation parameters for Fig. 3.11. Cluster size N_s, equivalent self-energy approximation Σ, on-site energy ϵ, hopping amplitude J, Hubbard interaction U, hopping modification λ, lattice spacing a, charge transfer amplitude γ and ion velocity $v_z^{(\mathrm{ion})}$ for $\mathrm{MoS_2}$. Units are $J_0 = 3.78\,\mathrm{eV}$, $a_0 = 1.42\,\text{Å}$ and $v_0 = 0.82\,\mathrm{nm/fs}$.

Acknowledgments

First, I would like to thank Professor Dr. Michael Bonitz for giving me the opportunity to work in his group and take part in the exciting research conducted there. The academic freedom he fosters provided both challenges and opportunities, and his expertise in quantum-kinetic theory was a great support throughout this work.
I am also grateful to Professor Dr. Fabio Caruso for his valuable insights into the physics of MoS_2 and his helpful suggestions for exploring new perspectives.
A special thanks goes to Dr. Karsten Balzer for providing reference data and his expertise on the ion-stopping model, as well as for always taking the time to answer my questions.
I would also like to thank my colleagues in the AG Bonitz: Dr. Jan-Philip Joost for his help with implementation and advice on NEGFs, Christopher Makait for stimulating discussions and proofreading, Erik Schroedter for his critical questions and support, and my office mates Paul Hamann and Tim Kalsberger, who were always available to discuss ideas and provide a positive working atmosphere.
Finally, I would like to thank Karolina Hofman, Zoe Beckers, and Maja Zimmer for their thorough proofreading of this thesis. A special thanks to Maja, whose patience and support throughout this process have been invaluable.

Bibliography

[1] D. R. Hartree, "The Wave Mechanics of an Atom with a Non-Coulomb Central Field. Part I. Theory and Methods," *Mathematical Proceedings of the Cambridge Philosophical Society*, vol. 24, no. 1, pp. 89–110, 1928. `https://doi.org/10.1017/S0305004100011919`.

[2] V. Fock, "Näherungsmethode zur Lösung des quantenmechanischen Mehrkörperproblems," *Zeitschrift für Physik*, vol. 61, no. 1, pp. 126–148, Jan. 1, 1930. `https://doi.org/10.1007/BF01340294`.

[3] J. C. Slater and G. F. Koster, "Simplified LCAO Method for the Periodic Potential Problem," *Physical Review*, vol. 94, no. 6, pp. 1498–1524, Jun. 15, 1954. `https://doi.org/10.1103/PhysRev.94.1498`.

[4] E. Runge and E. K. U. Gross, "Density-Functional Theory for Time-Dependent Systems," *Physical Review Letters*, vol. 52, no. 12, pp. 997–1000, Mar. 1984. `https://doi.org/10.1103/PhysRevLett.52.997`.

[5] N. Schlünzen, S. Hermanns, M. Scharnke, and M. Bonitz, "Ultrafast dynamics of strongly correlated fermions—nonequilibrium Green functions and selfenergy approximations," *Journal of Physics: Condensed Matter*, vol. 32, no. 10, p. 103 001, Dec. 2019. `https://doi.org/10.1088/1361-648X/ab2d32`.

[6] G. Stefanucci and R. van Leeuwen, *Many-Body Theory of Quantum Systems: A Modern Introduction.* Cambridge: Cambridge University Press, 2013.

[7] M. Bonitz, *Quantum kinetic theory*, 2nd ed. Cham: Springer, 2016.

[8] P. Lipavský, V. Špička, and B. Velický, "Generalized Kadanoff-Baym ansatz for deriving quantum transport equations," *Physical Review B*, vol. 34, p. 6933, 1986.

[9] J.-P. Joost, N. Schlünzen, and M. Bonitz, "G1-G2 scheme: Dramatic acceleration of nonequilibrium Green functions simulations within the Hartree-Fock generalized Kadanoff-Baym ansatz," *Physical Review B*, vol. 101, no. 24, p. 245 101, Jun. 1, 2020. `https://doi.org/10.1103/PhysRevB.101.245101`.

[10] M. Bonitz, J.-P. Joost, C. Makait, E. Schroedter, T. Kalsberger, and K. Balzer, "Accelerating Nonequilibrium Green Functions Simulations: The G1–G2 Scheme and Beyond," *Physica Status Solidi (b)*, vol. 261, no. 9, p. 2 300 578, Sep. 2024. `https://doi.org/10.1002/pssb.202300578`.

[11] J.-P. Joost, N. Schlünzen, H. Ohldag, M. Bonitz, F. Lackner, and I. Březinová, "The dynamically screened ladder approximation: Simultaneous treatment of strong electronic correlations and dynamical screening out of equilibrium," *Physical Review B*, vol. 105, no. 16, p. 165 155, Apr. 29, 2022. `https://doi.org/10.1103/PhysRevB.105.165155`. arXiv: `2202.10061 [cond-mat, physics:physics]`.

[12] N. N. Bogolyubov, *Problems of dynamic theory in statistical physics.* Oak Ridge, Tenn.: Technical Information Service, United States Atomic Energy Commission; available from Office of Technical Services, Dept. of Commerce, Washington, D.C., 1960, 113 p.

[13] J. de Boer and G. E. Uhlenbeck, *Studies in statistical mechanics. Volume I* (Studies in statistical mechanics; v. 1). Amsterdam: North Holland, 1962.

[14] J.-P. Joost, "Green Functions Approach to Graphene Nanostructures," Kiel University, 2022.

[15] K. Balzer, N. Schlünzen, H. Ohldag, J.-P. Joost, and M. Bonitz, "Accelerating nonequilibrium Green function simulations with embedding self-energies," *Physical Review B*, vol. 107, no. 15, p. 155 141, Apr. 25, 2023. `https://doi.org/10.1103/PhysRevB.107.155141`.

[16] A. Niggas, J. Schwestka, K. Balzer, D. Weichselbaum, N. Schlünzen, R. Heller, *et al.*, "Ion-Induced Surface Charge Dynamics in Freestanding Monolayers of Graphene and MoS2 Probed by the Emission of Electrons," *Physical Review Letters*, vol. 129, no. 8, p. 086 802, Aug. 18, 2022. `https://doi.org/10.1103/PhysRevLett.129.086802`.

[17] A. H. Castro Neto, F. Guinea, N. M. R. Peres, K. S. Novoselov, and A. K. Geim, "The electronic properties of graphene," *Reviews of Modern Physics*, vol. 81, no. 1, pp. 109–162, Jan. 14, 2009. `https://doi.org/10.1103/RevModPhys.81.109`.

[18] Q. H. Wang, K. Kalantar-Zadeh, A. Kis, J. N. Coleman, and M. S. Strano, "Electronics and optoelectronics of two-dimensional transition metal dichalcogenides," *Nature Nanotechnology*, vol. 7, no. 11, pp. 699–712, Nov. 2012. `https://doi.org/10.1038/nnano.2012.193`.

[19] A. Splendiani, L. Sun, Y. Zhang, T. Li, J. Kim, C.-Y. Chim, G. Galli, and F. Wang, "Emerging Photoluminescence in Monolayer MoS2," *Nano Letters*, vol. 10, no. 4, pp. 1271–1275, Apr. 14, 2010. `https://doi.org/10.1021/nl903868w`.

[20] J. S. Williams, "Materials modification with ion beams," *Reports on Progress in Physics*, vol. 49, no. 5, p. 491, May 1986. `https://doi.org/10.1088/0034-4885/49/5/001`.

[21] M. Bonitz, A. Filinov, J.-W. Abraham, K. Balzer, H. Kählert, E. Pehlke, *et al.*, "Towards an integrated modeling of the plasma-solid interface," *Frontiers of Chemical Science and Engineering*, vol. 13, no. 2, pp. 201–237, Jun. 1, 2019. `https://doi.org/10.1007/s11705-019-1793-4`.

[22] J. Von Neumann, *Mathematical foundations of quantum mechanics: New edition.* Princeton University Press, 2018, vol. 53.

[23] L. P. Kadanoff and G. Baym, *Quantum statistical mechanics.* Boca Raton: CRC Press, 2018.

[24] D. B. Boercker and J. W. Dufty, "Degenerate quantum gases in the binary collision approximation," *Annals of Physics*, vol. 119, no. 1, pp. 43–70, May 1, 1979. `https://doi.org/10.1016/0003-4916(79)90247-1`.

[25] M. Born and V. Fock, "Beweis des Adiabatensatzes," *Zeitschrift für Physik*, vol. 51, no. 3, pp. 165–180, Mar. 1, 1928. `https://doi.org/10.1007/BF01343193`.

[26] P. C. Martin and J. Schwinger, "Theory of Many-Particle Systems. I," *Physical Review*, vol. 115, no. 6, pp. 1342–1373, Sep. 15, 1959. `https://doi.org/10.1103/PhysRev.115.1342`.

[27] N. Schlünzen, J.-P. Joost, and M. Bonitz, "Achieving the Scaling Limit for Nonequilibrium Green Functions Simulations," *Physical Review Letters*, vol. 124, no. 7, p. 076 601, Feb. 19, 2020. `https://doi.org/10.1103/PhysRevLett.124.076601`.

[28] K. Balzer and M. Bonitz, "Neutralization dynamics of slow highly charged ions passing through graphene nanoflakes: An embedding self-energy approach," *Contributions to Plasma Physics*, vol. 62, no. 2, e202100041, Feb. 2022. `https://doi.org/10.1002/ctpp.202100041`.

[29] E. Gruber, R. A. Wilhelm, R. Pétuya, V. Smejkal, R. Kozubek, A. Hierzenberger, *et al.*, "Ultrafast electronic response of graphene to a strong and localized electric field," *Nature Communications*, vol. 7, no. 1, p. 13 948, Dec. 21, 2016. `https://doi.org/10.1038/ncomms13948`.

[30] J. Schwestka, "On the charge exchange dynamics of highly charged ions in atomically thin solids," Ph.D. dissertation, Technische Universität Wien, 2020.

[31] T. Koopmans, "Über die Zuordnung von Wellenfunktionen und Eigenwerten zu den Einzelnen Elektronen Eines Atoms," *Physica*, vol. 1, no. 1, pp. 104–113, 1934. `https://doi.org/10.1016/S0031-8914(34)90011-2`.

[32] K. S. Novoselov, A. K. Geim, S. V. Morozov, D.-e. Jiang, Y. Zhang, S. V. Dubonos, I. V. Grigorieva, and A. A. Firsov, "Electric field effect in atomically thin carbon films," *Science*, vol. 306, no. 5696, pp. 666–669, 2004.

[33] K. F. Mak, C. Lee, J. Hone, J. Shan, and T. F. Heinz, "Atomically Thin MoS2 : A New Direct-Gap Semiconductor," *Physical Review Letters*, vol. 105, no. 13, p. 136 805, Sep. 24, 2010. `https://doi.org/10.1103/PhysRevLett.105.136805`.

[34] J. Munárriz Arrieta, "Tight-Binding Description of Graphene Nanostructures," in *Modelling of Plasmonic and Graphene Nanodevices*, Cham: Springer International Publishing, 2014, pp. 13–23. `https://doi.org/10.1007/978-3-319-07088-9_2`.

[35] J. Hubbard, "Electron correlations in narrow energy bands," *Proceedings of the Royal Society of London. Series A. Mathematical and Physical Sciences*, vol. 276, no. 1365, pp. 238–257, 1963.

[36] M. P. von Friesen, C. Verdozzi, and C.-O. Almbladh, "Successes and Failures of Kadanoff-Baym Dynamics in Hubbard Nanoclusters," *Physical Review Letters*, vol. 103, no. 17, p. 176 404, Oct. 2009. `https://doi.org/10.1103/PhysRevLett.103.176404`.

[37] D. Jaksch and P. Zoller, "The cold atom Hubbard toolbox," *Annals of Physics*, vol. 315, no. 1, pp. 52–79, 2005. `https://doi.org/10.1016/j.aop.2004.09.010`.

[38] M. Qin, T. Schäfer, S. Andergassen, P. Corboz, and E. Gull, "The Hubbard Model: A Computational Perspective," *Annual Review of Condensed Matter Physics*, vol. 13, pp. 275–302, Volume 13, 2022 2022. `https://doi.org/10.1146/annurev-conmatphys-090921-033948`.

[39] S. Donsa, F. Lackner, J. Burgdörfer, M. Bonitz, B. Kloss, A. Rubio, and I. Březinová, "Nonequilibrium correlation dynamics in the one-dimensional Fermi-Hubbard model: A testbed for the two-particle reduced density matrix theory," *Physical Review Research*, vol. 5, no. 3, p. 033 022, 2023.

[40] E. H. Lieb and F. Y. Wu, "Absence of Mott Transition in an Exact Solution of the Short-Range, One-Band Model in One Dimension," *Physical Review Letters*, vol. 20, no. 25, pp. 1445–1448, Jun. 1968. `https://doi.org/10.1103/PhysRevLett.20.1445`.

[41] J. C. Butcher, "A history of Runge-Kutta methods," *Applied Numerical Mathematics*, vol. 20, no. 3, pp. 247–260, 1996. `https://doi.org/10.1016/0168-9274(95)00108-5`.

[42] T. Jahnke, A. Czasch, M. S. Schöffler, S. Schössler, A. Knapp, M. Käsz, *et al.*, "Experimental Observation of Interatomic Coulombic Decay in Neon Dimers," *Physical Review Letters*, vol. 93, no. 16, p. 163 401, Oct. 13, 2004. `https://doi.org/10.1103/PhysRevLett.93.163401`.

[43] L. S. Cederbaum, J. Zobeley, and F. Tarantelli, "Giant Intermolecular Decay and Fragmentation of Clusters," *Physical Review Letters*, vol. 79, no. 24, pp. 4778–4781, Dec. 15, 1997. `https://doi.org/10.1103/PhysRevLett.79.4778`.

[44] T. Jahnke, U. Hergenhahn, B. Winter, R. Dörner, U. Frühling, P. V. Demekhin, *et al.*, "Interatomic and Intermolecular Coulombic Decay," *Chemical Reviews*, vol. 120, no. 20, pp. 11 295–11 369, Oct. 28, 2020. `https://doi.org/10.1021/acs.chemrev.0c00106`.

[45] G.-B. Liu, W.-Y. Shan, Y. Yao, W. Yao, and D. Xiao, "Three-band tight-binding model for monolayers of group-VIB transition metal dichalcogenides," *Physical Review B*, vol. 88, no. 8, p. 085 433, Aug. 26, 2013. `https://doi.org/10.1103/PhysRevB.88.085433`.

[46] E. Cappelluti, R. Roldán, J. A. Silva-Guillén, P. Ordejón, and F. Guinea, "Tight-binding model and direct-gap/indirect-gap transition in single-layer and multilayer MoS2," *Physical Review B*, vol. 88, no. 7, p. 075 409, Aug. 8, 2013. `https://doi.org/10.1103/PhysRevB.88.075409`.

[47] S. Lebègue and O. Eriksson, "Electronic structure of two-dimensional crystals from *ab initio* theory," *Physical Review B*, vol. 79, no. 11, p. 115 409, Mar. 11, 2009. `https://doi.org/10.1103/PhysRevB.79.115409`.

[48] K. V. Shanavas and S. Satpathy, "Effective tight-binding model for MX2 under electric and magnetic fields," *Physical Review B*, vol. 91, no. 23, p. 235 145, Jun. 26, 2015. `https://doi.org/10.1103/PhysRevB.91.235145`.

[49] D. W. Smith and O. W. Day, "Extension of Koopmans' theorem. I. Derivation," *The Journal of Chemical Physics*, vol. 62, no. 1, pp. 113–114, Jan. 1, 1975. `https://doi.org/10.1063/1.430253`.

[50] C. Reeves and V. Vlcek, "A Real-time Dyson Expansion Scheme: Efficient Inclusion of Dynamical Correlations in Non-equilibrium Spectral Propertie," 2024. arXiv: `2403.07155`.

[51] J.-P. Joost and M. Bonitz, "New algorithms and linear scaling approaches to NEGF simulations," in *Roadmap Towards Modelling of Ultrafast Phenomena in Quantum Materials*, F. Caruso and M. Sentef, Eds., 2024.

[52] G. Chiappe, E. Louis, E. San-Fabián, and J. A. Vergés, "Can model Hamiltonians describe the electron–electron interaction in pi-conjugated systems?: PAH and graphene," *Journal of Physics: Condensed Matter*, vol. 27, no. 46, p. 463 001, 2015.

Erklärung

Hiermit versichere ich, dass ich die Arbeit selbständig verfasst und keine anderen als die angegebenen Quellen und Hilfsmittel benutzt habe.
Ich versichere zudem, dass ich die Arbeit in keinem anderen Prüfungsverfahren eingereicht habe.
Weiterhin versichere ich, dass die eingereichte schriftliche Fassung der Arbeit der auf dem elektronischen Speichermedium gespeicherten Fassung entspricht.

Kiel, den ____________________

____
Unterschrift